Investigation of corium melt interaction with NPP reactor vessel steel (METCOR) Phase 2

PROGRESS REPORT
01/01/05 – 31/10/05

Investigation of molten steel and suboxidized molten corium (C30) interaction with vessel steel in a neutral atmosphere ($T^{\max}_{st.surf.}$ »1400°C). Test MC9.

Project title	Investigation of Corium Melt Interaction with NPP Reactor Vessel Steel (METCOR, Phase 2), No.833.2	
Contracting organization	ISTC	
File code	METCOR2/RMC09	
Project location	Alexandrov Research Institute of Technology of the RF Ministry for Atomic Energy Russia, 188540, Sosnovy Bor, Leningrad Region, NITI	
Project manager	Name	V.B. Khabensky
	Signature	
	Date	

Authors

Dr.(Eng.), Prof.	V. B. Khabensky
Dr.(Eng.)	S. V. Bechta
Ph.D.	V. S. Granovsky
	S. A. Vitol
	E. V. Krushinov
Ph.D.	S. Yu. Kotova
Ph.D.	A. A. Sulatsky
Prof., Associate member of the Russian Academy of Sciences	V. V. Gusarov
	V. I. Almjashev
Dr.(Eng.), Prof.	Yu. B. Petrov
Ph.D.	I. V. Kulagin
Ph.D.	D. B. Lopukh
Ph.D.	A. Yu. Pechenkov
Ph.D.	I. V. Poznyak
Ph.D.	S. A. Smirnov
	V. G. Bliznyuk
	V. R. Bulygin
	E. M. Belyaeva
	E. K. Kalyago
	N. E. Kamensky
	R. A. Kosarevsky
	A. V. Lysenko
	A. P. Martynov
	V. V. Martynov
	E. V. Shevchenko
	A. A. Chertkov

ABSTRACT

The report presents a description and basic results of MC9 test of the ISTC METCOR Phase 2 Project carried out in the NITI, Sosnovy Bor, on the “Rasplav-3” test facility.

The test focused on corrosion of vessel steel at its interaction with molten corium C-30 and molten stainless steel, in argon, the maximum temperature at the interaction interface being 1400°C.

CONTENTS

Introduction

In accordance with the predicted scenarios of a severe accident development, the pool forming at the reactor vessel bottom would contain molten metal along with the oxidic melt. The OECD MASCA Project has shown the metallic part of the mentioned melt to contain U and Zr in concentrations which depend on the degree of Zr oxidation and the mass fraction of steel.

The tests MC6, MC7 and MC8 performed in the framework of METCOR Phase 2 Project yielded data on kinetics and maximum depth of vessel steel corrosion at the interaction with suboxidized molten corium.

MC9 was aimed at determining characteristics of the corrosion process during the interaction between vessel steel and molten metal which had formed in the pool bottom part as a result of a prior interaction between suboxidized molten corium and stainless steel.

1. Experimental conditions and primary results

1.1. Test facility layout and charge composition

The design of furnace and steel specimen, schematics of the gas-aerosol sampling and the above-melt atmosphere in MC9 did not differ from those used in MC6, MC7 and MC8 [1]. The corresponding diagrams and pictures are given in Figs. 1.1.1-1.1.3. The technique of temperature survey also did not differ from that applied in previous tests. The exact locations of thermocouple junctions are presented in Table 1.1.
The total mass of the loaded charge amounted to 2000 g, and the calculated height of the oxidic melt pool was 65 mm.

Charge composition:

- 1800 g 76.2% UO2 + 9.3% ZrO2 + 14.5% Zr (mass %), of which a 5-mm layer of C-32 corium crushed down to particles sized less than 50 μm was put on the specimen top.
- 200 g of stainless steel of 08Kh18N10T grade.

The oxygen-free above-melt atmosphere was produced using the high-purity argon.

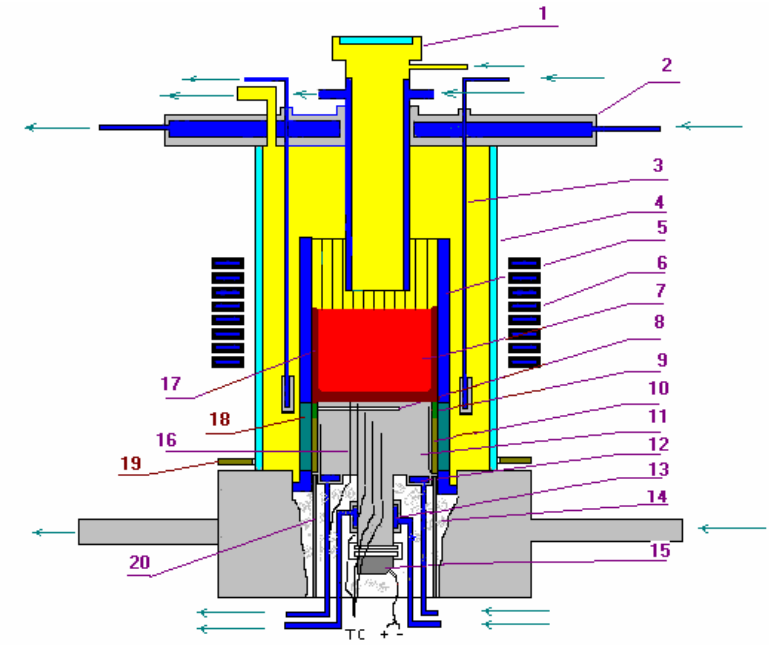

1 – water-cooled pyrometer shaft; 2 – water-cooled cover; 3 – water-cooled electromagnetic screen; 4 – quartz tube; 5 – crucible section; 6 – inductor; 7 – melt; 8 – acoustic defect; 9 –molten ZrO_2; 10 – ZrO_2 powder heat insulation; 11 – vessel steel specimen; 12 – top specimen calorimeter; 13 – bottom specimen calorimeter; 14 – kaolin wool heat insulation; 15 –ultrasonic sensor; 16 – thermocouples; 17 – crust; 18 – electromagnetic screen; 19 – uncooled electromagnetic screen; 20 – cylindrical support of the specimen.

Fig. 1.1.1 – IMCC furnace schematics

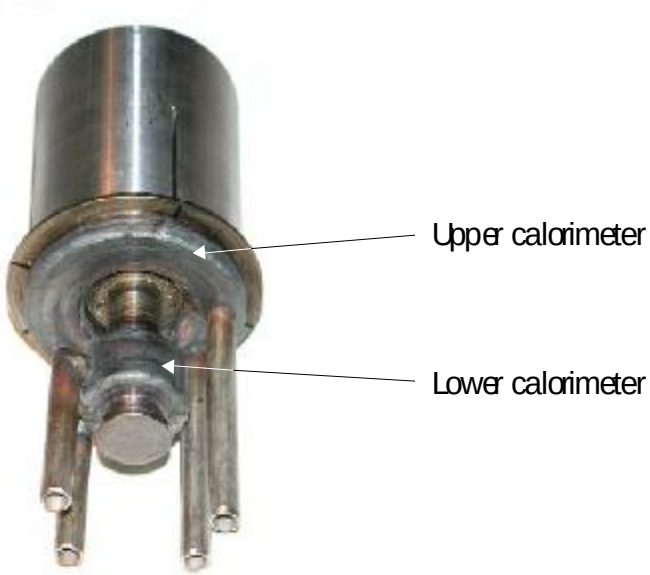

Fig. 1.1.2 – Vessel steel specimen

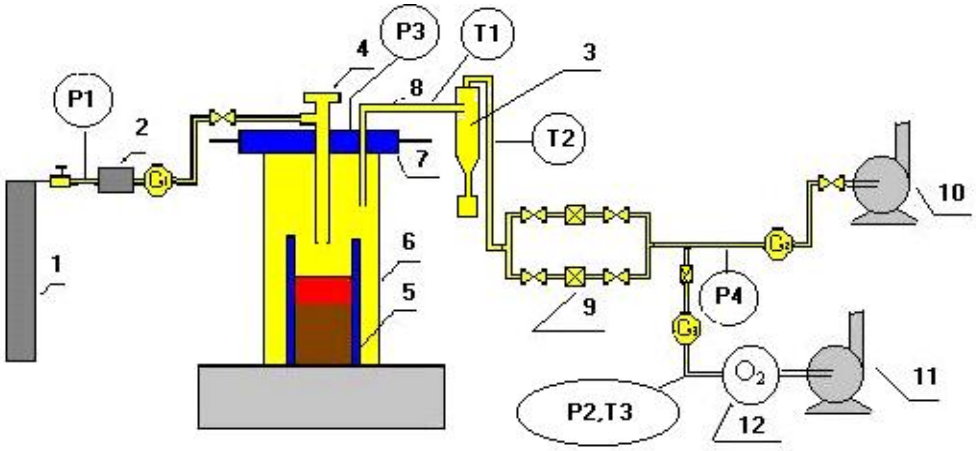

1 – Argon cylinder; 2 – silica gel dehumidifier; 3 – cyclone; 4 – pyrometer shaft; 5 – crucible; 6 – quartz tube; 7 – water-cooled cover; 8 – aerosol pathway; 9 - LAF filters; 10 – fan; 11 – vacuum pump; 12 – oxygen sensor; P1-P4 – pressure gauges; G1, G2– flow meters, G3-rotameter; T1-T3 – thermocouples.

Fig. 1.1.3 – Gas in and out

Table 1.1 – Thermocouple hot junction locations

Thermocouple No.	α° (horizontal angle)	r, mm (distance from the specimen axis)	h, mm (distance from the melt-facing top)
TC01	0	10	0
TC02	90	10	2
TC03	45	10	4
TC04	135	10	7
TC05	270	10	6
TC06	180	10	8
TC07	225	10	20
TC08	315	29	0
TC09	90	29	2
TC10	45	29	4
TC11	225	29	20
TC12	180	29	40
TC13	45	7.5	104

1.2. Experimental procedure

Before the test, the furnace was blasted with argon for 10 minutes at 10 l/min. It was followed by the startup heating and molten C-32 corium pool production with a crust above its surface, at Z_e=10 mm and Z_c=20 mm (Z_e is the distance from the electromagnetic screen upper edge to the specimen upper top, and Z_c is the distance from the inductor lower coil to the specimen upper top). Then the pool of molten C-32 corium has been produced and homogenized.

According to thermocouple readings, at 1760 sec the temperature on the specimen top reached ~ 650 ºC. Melting of the charge had ended by 2250 sec, as it was confirmed by stabilization of power extracted from the cold crucible by cooling water, and the specimen heating-up has been going since then. By 3236 sec the pool depth was approximately 70 mm and the bottom crust

thickness was 3 mm. At 4200 sec readings of the upper thermocouples reached the calculated values. According to the test plan, the temperature on the specimen surface was stabilized by the generator regime at 1400 ºC (upper thermocouple) and at 1290 ºC (next thermocouple TC 02). At 4633 sec the first portion of steel was introduced on the molten pool surface and followed by the 2nd one at 4654 sec. The introduction of metal was accompanied by the drop of temperature of both the melt and specimen. At the same time, the generator regime has virtually not changed. 70 sec after the introduction of the 2nd portion of metal, the molten steel drowned. The temperatures of both the melt and specimen kept decreasing. This effect was conditioned not only by melt cooling with the introduced steel, but also by changes in the electromagnetic characteristics of the system after formation of the metal-oxidic pool. As the result, the melt surface got covered with an oxidic crust. To increase the specimen upper top temperature to the desired value, the generator regime has been stepped up, the screen shifted downwards twice for 5 mm each time (to attain Z_e =0) and the cold crucible with the melt shifted upwards 3 times for 5 mm each time (to attain Z_c=5 mm).

At 5660 sec the temperature profile in the specimen attained the calculated values, and further on, according to the test plan, the temperature regime stabilization was provided for ~ 10 hours and measurements were made during the vessel steel ablation at the interaction with the melt. Aerosols were sampled throughout the test. At 50220 sec heating was disconnected and the ingot with specimen was cooled down in argon.

Figs. 1.2.1 – 1.2.7 show the results of temperature measurements, as well as changes of electrical parameters, heat and electrical power.

An ultrasonic sensor [1] was used for the *in situ* measurements of the specimen ablation depth. The results of measurements are given in Section 2.4.

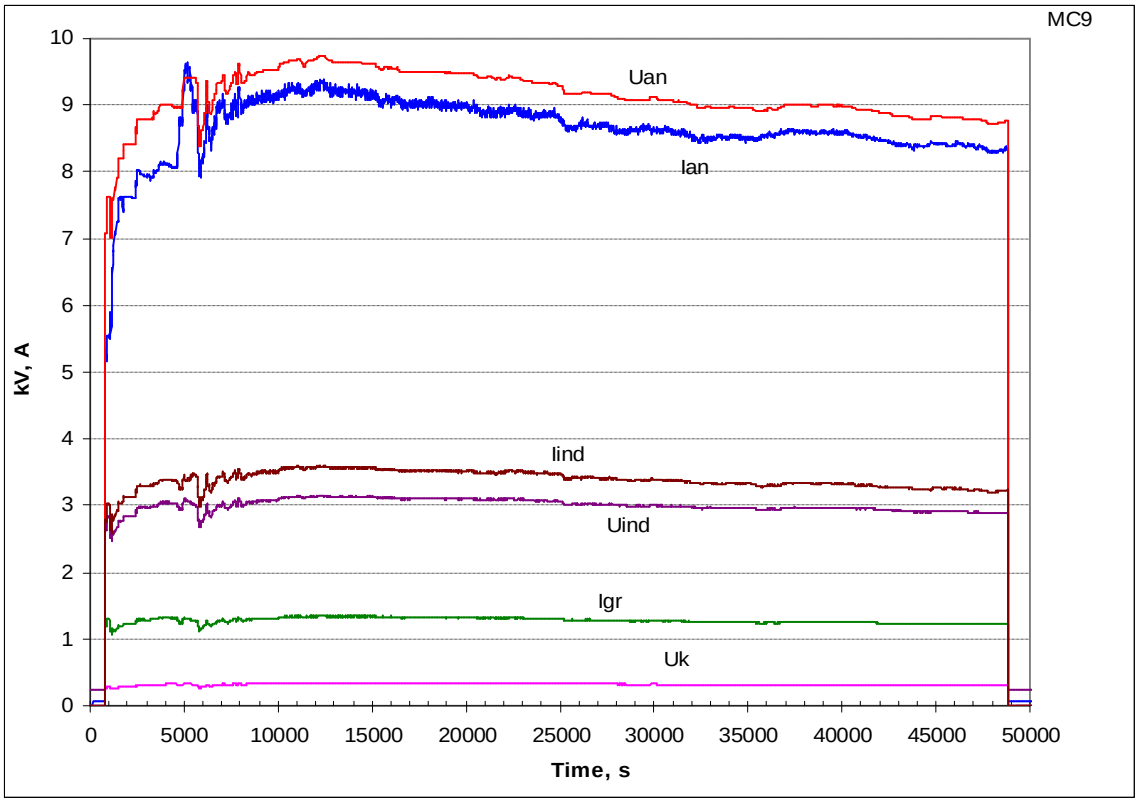

Uan and Ian –anode voltage and current; Uind and Iind – inductor voltage and current; Igr – valve grid current; Uk – signal, proportionate to voltage at the generator secondary circuit.

Fig. 1.2.1 – History of the induction furnace electrical parameters

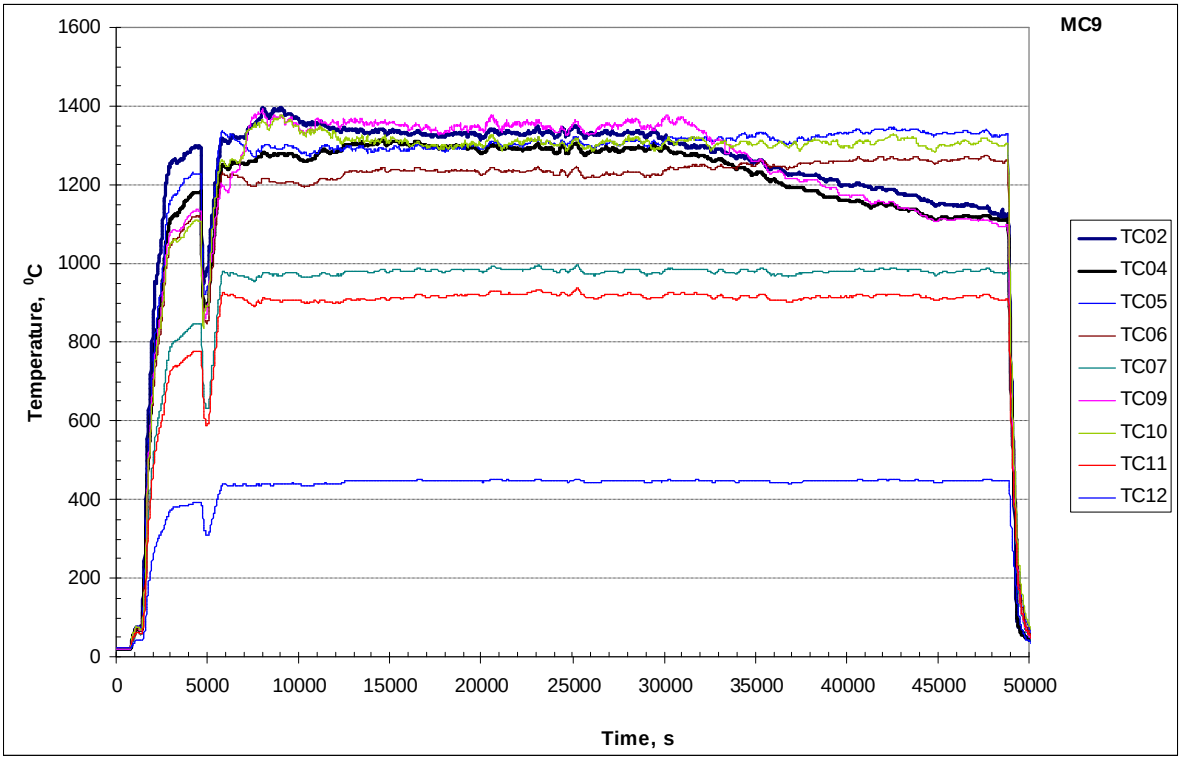

Fig. 1.2.2 – Thermocouple readings

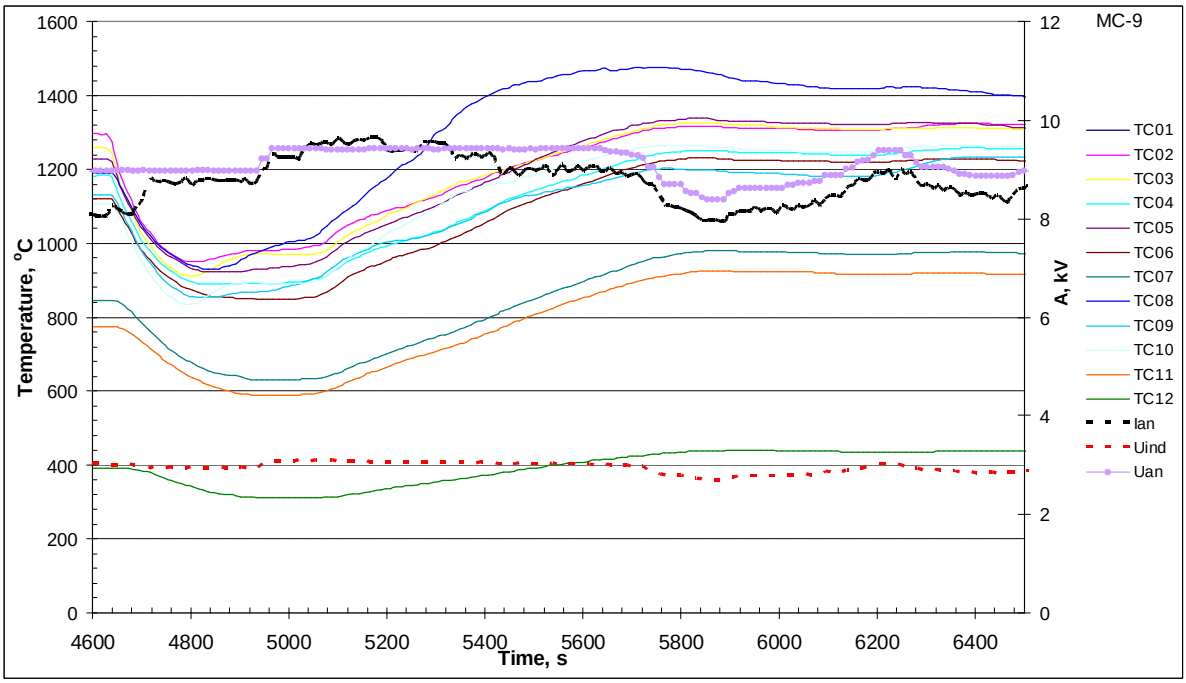

Fig. 1.2.3 – Thermocouple readings and generator regimes after metal introduction into molten corium

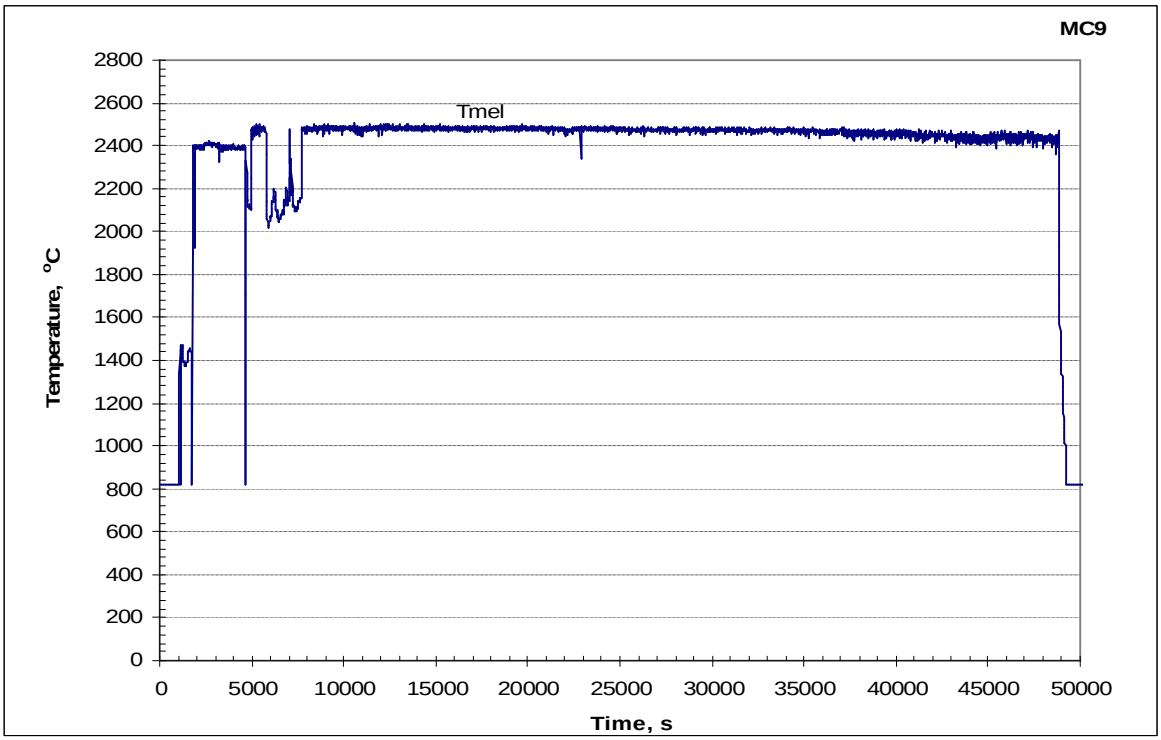

Fig. 1.2.4 – Temperature at the melt surface

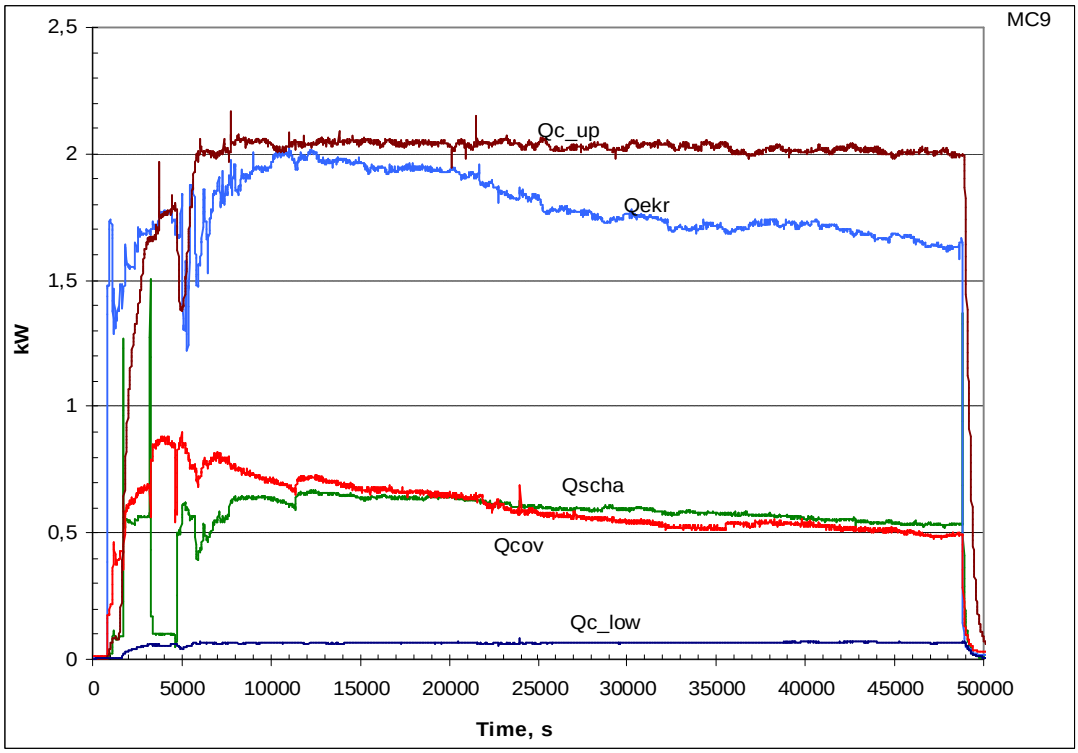

Qc_up – power extracted into upper calorimeter; Qc_low – power extracted into lower calorimeter; Qekr – power extracted into upper screen; Qscha – power extracted into pyrometer shaft; Qcov – power extracted into crucible cover.

Fig. 1.2.5 – History of electromagnetic and thermal power extracted into different furnace components

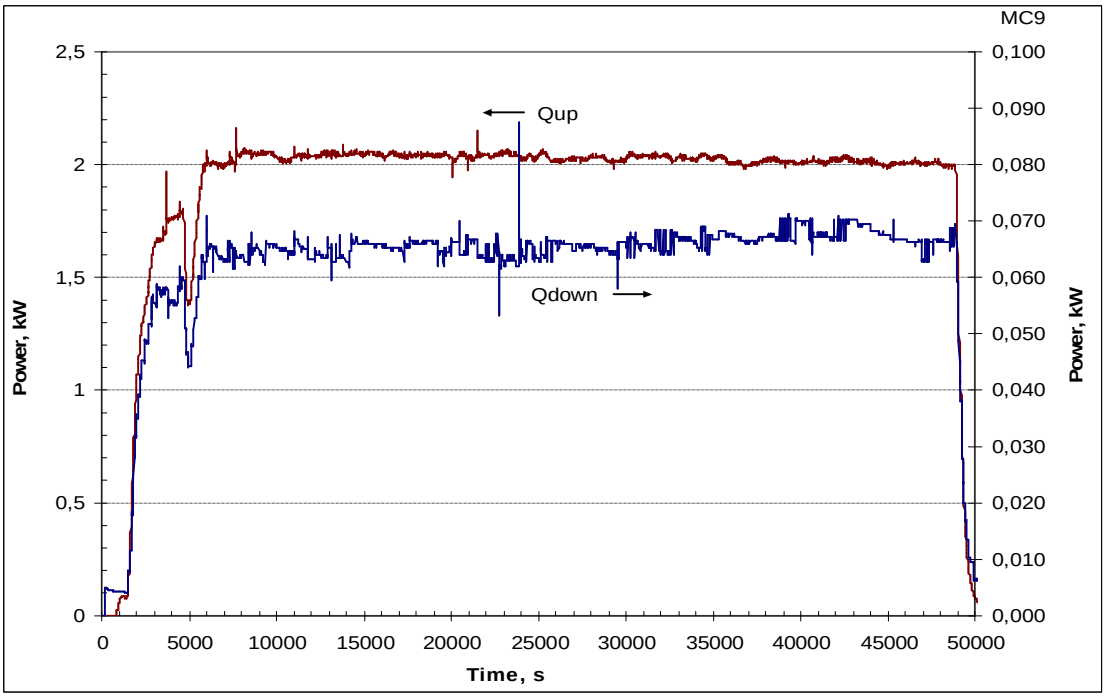

Qup – power extracted into upper calorimeter; Qdown– power extracted into lower calorimeter.

Fig. 1.2.6 – History of power extracted into upper and lower calorimeters

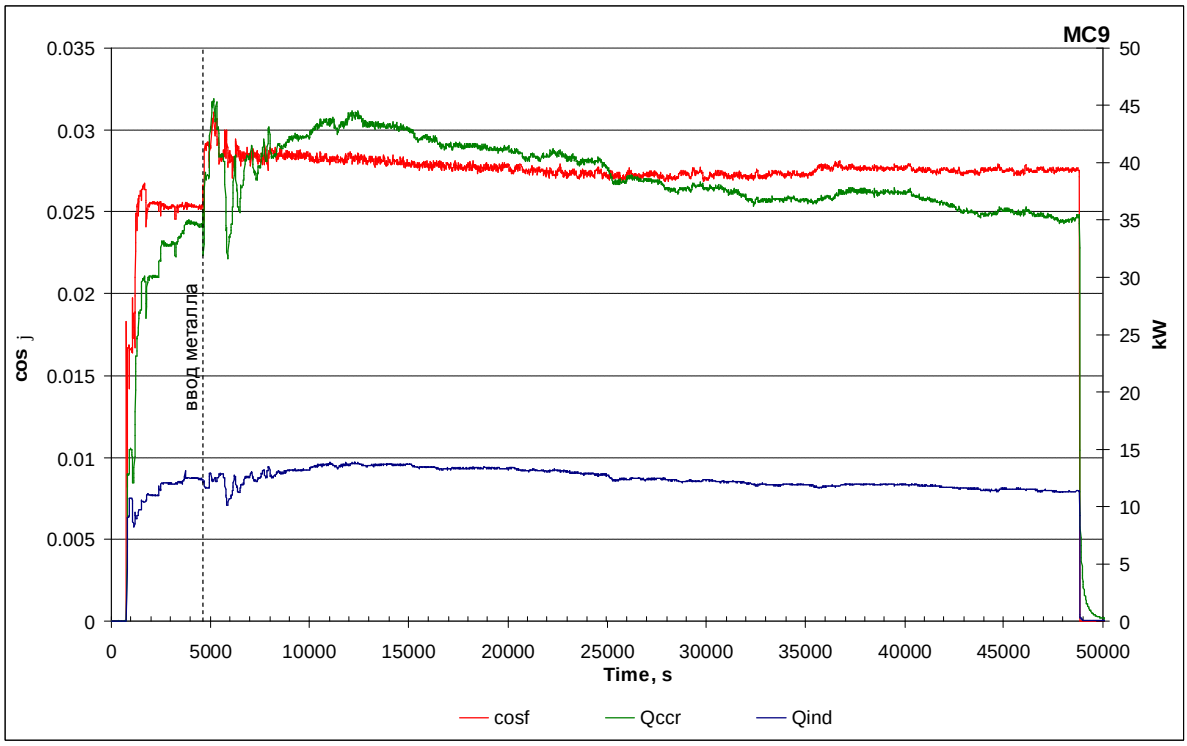

Qccr - power extracted into crucible; Qind – power extracted into inductor; cos φ – inductor power factor.

Fig. 1.2.7 – History of electromagnetic and thermal power extracted into crucible and inductor, and of inductor power factor

2. Posttest analysis

2.1. Ingot macrostructure

The furnace disassembly showed the crucible sections to be covered with a layer of aerosols (see Fig. 2.1.1). The mass of aerosols collected from the crucible sections amounted to 74.4 g. The mass of the crust above the melt was 32.3 g.

At the extraction of the corium ingot and steel specimen from the crucible, the oxidic ingot separated from the metallic specimen and partially broke (Fig. 2.1.2). A fragment of the oxidic ingot and the steel specimen from which templates for further analysis were produced, had been separately embedded in epoxy. Then the steel specimen was cut along its axis. Fig. 2.1.2 shows the oxidic ingot extracted from the crucible, and the steel specimen top after the test. The corium ingot height was approximately 60 mm. Thickness of the skull between the corium ingot and steel specimen was about 1 mm. Fig. 2.1.3 that shows the longitudinal section of the steel specimen, features a big pore (shrinkage cavity) in the specimen upper part. The interaction zone boundary is quite distinct, while the zone itself consists of two parts – lower and upper.

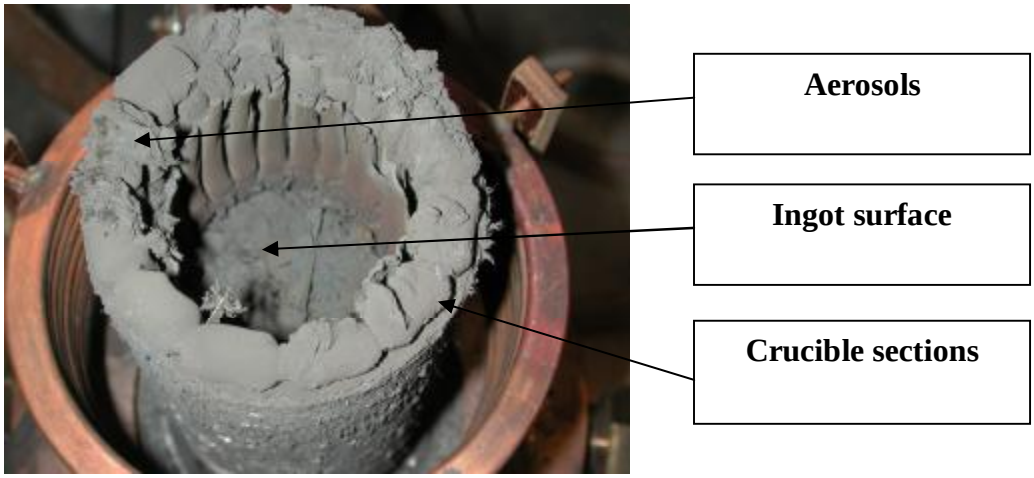

Fig. 2.1.1 – Crucible after the test

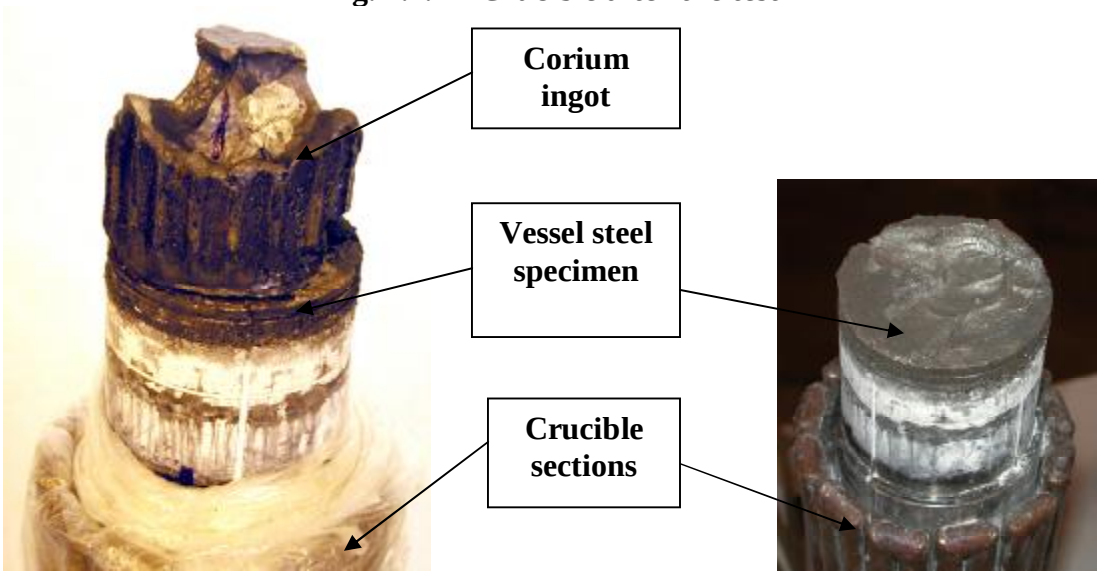

Fig. 2.1.2 – Oxidic ingot and steel specimen extracted from the crucible

Fig. 2.1.3 – Template cut from the oxidic ingot, and the steel specimen longitudinal section

2.2. Physicochemical analysis

2.2.1. Initial components analysis

When preparing the test, the charge components: urania, zirconia, the steel introduced into the melt, metallic zirconium, as well as the vessel steel witness specimen have been checked for the main substance and impurities content. The powdered urania was checked by thermogravimetry and the oxygen/uranium ratio was found to equal 2.0. The composition of charge components and of the steel introduced into the melt in MC9 is given in Tab. 2.2.1.

Table 2.2.1 – Composition of corium charge components in MC9

Components	**Main substance content, mass %**	**Impurities, mass %**	**Notes**
UO_2 powder, <200 μm dispersivity	UO_2>99.0	Fe<0.03; As<0.0003; CuO<0.01; phosphates<0.002; chlorides<0.003.	Certificate data; thermogravimetry
ZrO_2 powder, <100 μm dispersivity	(ZrO_2+HfO_2) >99.3	Al_2O_3<0.03; Fe_2O_3<0.05; CaO<0.03; MgO<0.02; SiO_2<0.2; TiO_2<0.1; P_2O_5<0.15; (Na_2O+K_2O)<0.02.	Certificate data
Zr Нб-1 metallic alloy	Zr >99.0	Nb<1.0	XRF
Steel, 08Kh18N10T grade	Fe>69.14	Si-0.55; S-0.004; P-0.034; Ni-10.4; Mn-1.31; Cr-17.9; Cu-0.18; Ti-0.48.	XRF

2.2.2. Material balance of the test

In order to make the material balance of MC9, the initial charge components and fused products were weighed with accuracy up to 0.1 g. Then the fused products were subjected to

physicochemical analysis, the results of which were used for making material balance of components.

Material balance of components in MC9 is given in Tab. 2.2.2.

Table 2.2.2 –MC9 material balance

Introduced into the melt		Collected after the test, g	
Corium C-27 (<50 μm)	150.0	Rod sample	14.9
UO_2	1371.6	Above melt crust	32.3
ZrO_2	166.5	Ingot	1686.7
Metallic Zr	261.8	Skull from the surface of metal	12.7
Steel 08Kh18N10T	198.7	Aerosols from filters**	88.3
		Aerosols from the bottle? (колбы), crucible sections and pipes	229.2
		Spillages*	56.4
Σ	2148.6	Σ	2120.5
Debalance		28.1	

*- Powders (remaining charge, splashes, aerosols).

**- Two large-area filters were used in turn during the test. The mass of aerosols collected from the 1st filter was 36.9 g and 51.4 g from the 2nd one.

The debalance, amounting to less than 1.3% of the introduced charge, is due to the aerosols lost during the cleaning of the clogged gas-aerosol lines.

2.2.3. XRF of the witness specimen and fused products

The elemental composition of the fused products was determined by XRF using the SPARK-1M and SPECTROSCAN MAX-GV spectrometers [2]. The results of the vessel steel witness specimen composition analysis are given in [2].

The remaining parts of the oxidic ingot, above-melt crust, skull from the steel specimen surface and rod sample were separately crushed into particles sized below 200 μm and then average samples were taken by quartering. The average samples were further ground into particles sized less than 50 μm and analyzed. All the preparatory works were carried out in argon. Tab. 2.2.3.1 contains the XRF results for the fused products.

Table 2.2.3.1 – XRF results for the fused products

Sample	Content, mass %			
	U	Zr	Fe	Impurities and O*
Ingot average sample	63.7	20.3	2.9	12.5 (Cr-0.1, Ni-0.2, Si-0.3)
Above-melt crust	42.1	8.5	21.1	18.7 (Cr-5.0, Ni-2.0, Si-0.8, Mn-1.8)
Skull from the steel specimen surface	64.5	11.8	7.2	14.9 (Cr-0.7, Ni-0.5, Si-0.1, Mn-0.3)
Rod sample**	65.9	21.6	<0.1	12.4

*) O and impurities determined from the residue.

**) The rod sample is partially oxidized; the sample has been analyzed only for the sake of making the elemental material balance.

Notable is the big difference in iron content – from 0.2 to 21.1 % – in the fused products, as well as the presence of components of the stainless and vessel steels (manganese, chromium, nickel and silicon) in the skull and especially in the above-melt crust. This is determined by their evaporation because of strong superheating for almost 1000 °C above the steel melting temperature, the melt temperature being around 2500 °C, and long duration of the test.

For determining the elemental composition of the interaction zones, 2 plates (No.1 and No.2) were cut out from the steel specimen (see Fig. 2.2.1). They represent flat polished pieces of metal 10–15 mm in diameter and 4–5 mm thick. Each of them was subjected to XRF from two sides, i.e. from top and bottom.

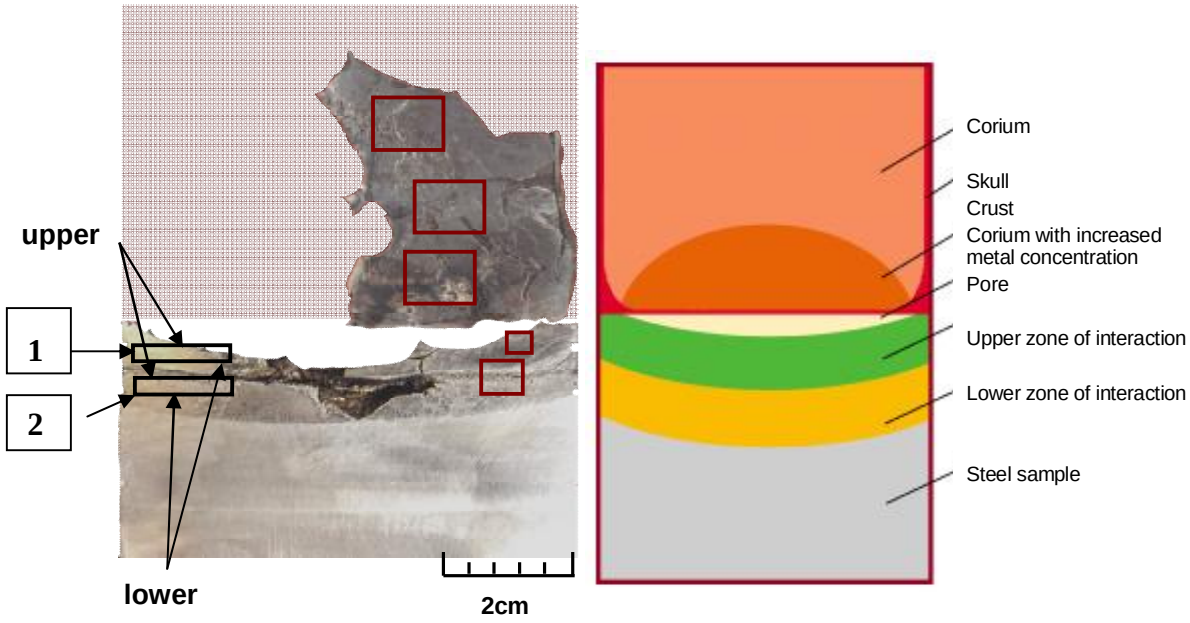

Fig. 2.2.1 – Location of the plates cut for XRF from the interaction zone

Tab. 2.2.3.2 presents the XRF results for the said plates cut from different layers of the interaction zone.

Table 2.2.3.2 – XRF results for the steel plates from the interaction zone

Sample	Content, mass %						
	U	Zr	Fe	Cr	Ni	Mn	Ti
Plate No.1 top	40.99	9.71	46.94	1.12	0.97	0.21	0.03
Plate No.1 bottom	22.64	25.68	49.60	0.90	0.92	0.22	0.03
Plate No.2 top	24.43	22.71	50.72	0.92	0.97	0.22	0.03
Plate No.2 bottom	35.74	5.42	55.96	1.54	1.04	0.26	0.03

It may be seen from the results of analysis that the elemental composition of the interaction zone upper layer bottom and that of the lower layer top are almost the same. However, the compositions of top and bottom of the plates from each layer, and of the lower layer bottom differ significantly: by almost a factor of two for U and 2.5 – 4 times for Zr.

2.2.4. Chemical analysis of the fused products

Both the corium ingot average sample, aerosols collected from filters 1 and 2, and skull from the surface of metal have been checked for the content of ions of U, Fe and Zr^0. The concentration of U was determined by spectrophotometry with arsenazo III [3, 4]. Determination of iron mass concentration was done by photocolorimetry with orthophenanthroline. [5-7].

The final molten corium oxidation degree was calculated on the basis of the content of free zirconium in the melt. The volumetric method [8, 9] was applied to determine free zirconium in corium. The final degree of corium oxidation corresponded to C-45.

The results of Zr^0, Fe and U determination are given in Tab. 2.2.4.1.

Table 2.2.4.1 – Chemical analysis of corium ingot

Method of detection	Photocolorimetry		Volumetric, Zr^0
Sample	U	Fe	
	mass %		
Ingot average sample	62.00	2.9	12.30
Skull from the surface of metal	63.47	15.9	9.08
Aerosols from filter 1	9.29	63.9	-
Aerosols from filter 2	11.18	75.2	-

Tab.2.2.4.2 gives the errors of the analyses.

Table 2.2.4.2 – Analyses errors

Element	Error, % rel.	Detection method
U	5	Photocolorimetry
Zr^0	10	Volumetric
Fe	5	Photocolorimetry
U	5	XRF
Zr		
Fe		

A comparison of the XRF and chemical analyses results of the main components in the fused products has shown them to be in satisfactory accord (Tabs. 2.2.3.1 and 2.2.4.1).

2.2.5. Determination of aerosols release rate and composition

The conducted posttest analyses yielded quantitative and qualitative characteristics of the aerosols generated in MC9.

Conditions of aerosol sampling:

1. During the starting regime and further up to 22930 sec aerosols were sampled to filter 1.
2. From 22930 sec till the end of the test aerosols were sampled to filter 2.
3. The carrier gas flow rate was constant throughout the test.
4. The aerosol sampling does not take into account changes in the adhesive ability of cold surfaces due to the aerosols build-up.

The mass of aerosol deposits on the filters was determined by the gravimetric method using the VLR -200G laboratory equal-arm balance of the 2nd class. The accuracy of weighing was ±0.12 mg. A special technique employing exposure in the exiccator with concentrated sulfuric acid was developed for both preparing the filters for the test and measuring the deposits.

In the course of the test, a part of aerosols deposited on the furnace sections and lines[1] (transport losses), while the greater part was collected on the filters. The following procedure of calculating the aerosol generation rate has been worked out for determining the aerosol release rate taking into account transport losses in the furnace lines.

Designations:

M^0_Σ - mass of total aerosols collected in the furnace, g;

m_Σ - mass of total aerosols collected from all filters, g;

m_F – mass of aerosols collected from respective filters, g;

τ_F – time of sampling to filters;

k – correction factor for aerosol losses;

V^Σ_F – average total aerosol release rate, mg/h;

V^{depos}_F – average total aerosol deposition rate in the lines, mg/h;

V_F – rate of aerosol deposition on the filters, mg/cm^2·h;

S - melt surface area, 39.6 cm^2.

The mass of aerosol deposits in the lines and on filters is calculated as:

$$m^{depos}_{F(i)}=k\cdot V^{\Sigma}_{F(i)}\cdot\Delta\tau_{F(i)}. \quad (1)$$

The mass of total aerosol deposits on the filters:

$$m_{F(i)}=(1-k)\cdot V^{\Sigma}_{F(i)}\cdot\Delta\tau_{F(i)}. \quad (2)$$

The mass of total aerosol deposits in the furnace through the test is a sum of aerosols deposited in the lines and on filters throughout the test.

$$M^0_\Sigma=\Sigma\, m^{depos}_{F(i)}. \quad (3)$$

By substituting expression (1) into formula (3), we obtain:

$$M^0_\Sigma=\frac{k}{1-k}\cdot(m_\Sigma). \quad (4)$$

Therefore, the correction factor for the aerosol losses equals:

[1] The determination of aerosol deposits takes into account masses of aerosols that deposited in the gas-aerosol lines, on the crucible surfaces, quartz tube and cover.

$$k = \frac{M_{\Sigma}^{0}}{(m_{\Sigma}) + M_{\Sigma}^{0}}. \quad (5)$$

By substituting expression (5) into formula (1), we obtain:

$$m_{F(i)}^{depos} = \frac{M_{\Sigma}^{0} \cdot V_{F(i)}^{\Sigma}}{m_{\Sigma} + M_{\Sigma}^{o}} \cdot \Delta t_{F(i)}. \quad (6)$$

Consequently,

$$m_{F(i)}^{depos} = \frac{M_{\Sigma}^{0}}{m_{\Sigma}} \cdot m_{F(i)}. \quad (9)$$

The deposition rate at each filter is calculated as follows:

$$V_{F(i)} = \frac{m_{F(i)}^{depos} + m_{F(i)}}{S \cdot \Delta t_{F(i)}}. \quad (10)$$

By substituting expression (9) into (10), we obtain the final formula for calculating the aerosol deposition rate (including that for each element), taking into account the transport losses:

$$V_{F(i)} = \frac{(m_{\Sigma} + M_{\Sigma}^{0})}{m_{\Sigma}} \cdot \frac{m_{F(i)}}{\Delta t_{F(i)} \cdot S}. \quad (11)$$

The elemental composition of aerosols was determined by XRF. Tabs. 2.2.5.1, 2.2.5.2 and Fig. 2.2.2 contain the data on the aerosol composition and on the calculated release rates taking into account the transport losses.

Table 2.2.5.1 – XRF results for aerosols

Sample	Content, mass %						
	U	Zr	Fe	Cr	Ni	Mn	Ti
Aerosols from sections	18.53	1.02	58.66	13.46	4.02	1.75	0.06
Aerosols from filter 1	9.31	0.22	64.04	19.88	4.10	1.16	0.03
Aerosols from filter 2	10.83	<0.01	78.98	3.10	5.45	0.17	<0.01

Table 2.2.5.2 – Melt components release rates calculated from filter deposits with an account for losses in the gas lines

Sample	Exposure time, s	Rates of elements release from the melt (filters operating; losses in gas lines taken into consideration), mg/cm^2·h.						
		U	Zr	Fe	Cr	Ni	Mn	Ti
Aerosols from filter 1	21759	51.64	1.22	355.24	110.28	22.74	6.43	0.17
Aerosols from filter 2	26724	68.12	0.06	496.78	19.50	34.28	1.07	0.06

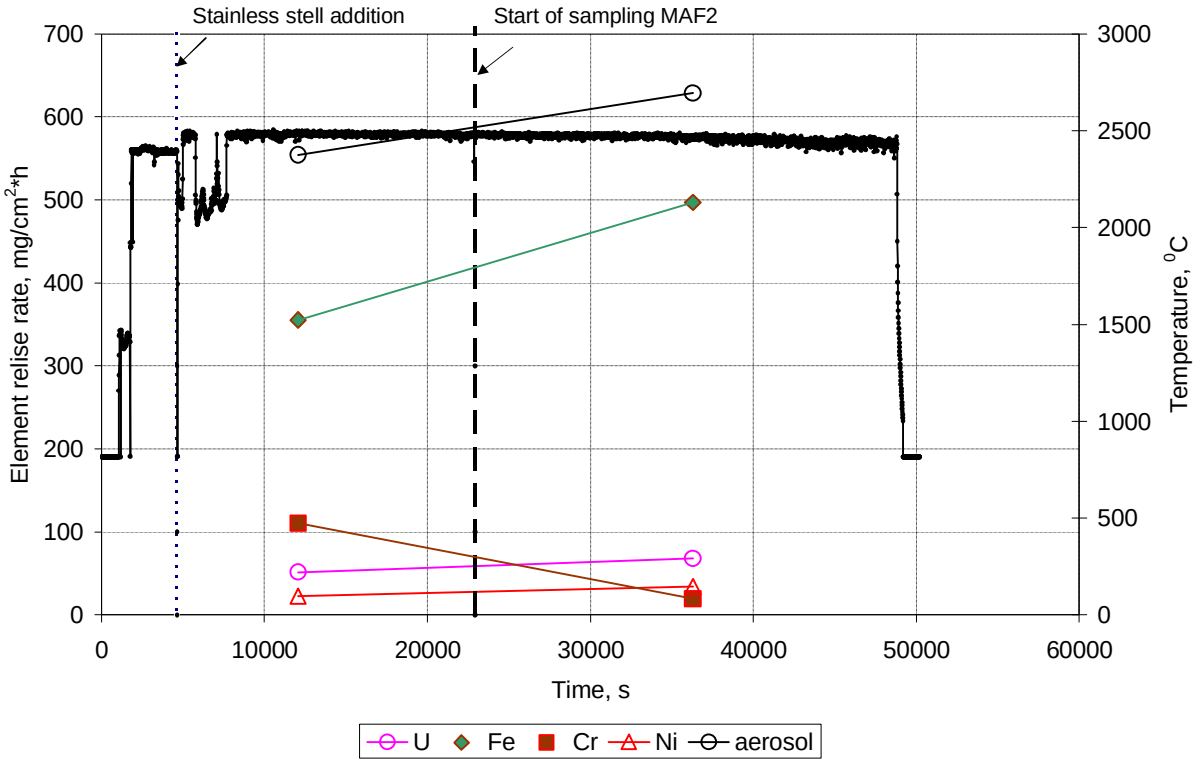

Fig. 2.2.2 – Aerosols and separate elements release rates in MC9

It is evident from the obtained results that both components of the stainless steel added to the melt, and then the vessel steel components were intensively evaporating during the test. This is confirmed by a smaller content of chromium and manganese on the 2nd filter than on the 1st one.

2.2.6. Elemental balance of the test

To understand the processes that occurried in the test better, the elemental balance has been made. Tab. 2.2.6.1 shows changes in the composition of corium at its interaction with vessel steel. For this purpose, the data from Tabs. 2.2.6.2 - 2.2.6.8 were used.

Table 2.2.6.1 –Components repartitioning between corium and vessel steel in MC9

Element	Initial charge, G	Products that did not participate in melting (spillages, crusts, rod). XRF data (Tab. 2.2.6.2), g	Melt composition at steel adding (1-2), g	Added steel, XRF data (Tab. 2.2.6.4), g	Melt composition after steel adding (3+4), g	Aerosols collected before 22930 sec, calculated taking transport losses into account [2], g	Aerosols collected during the test, calculated taking transport losses into account [2] g	Quantity of vessel steel that transited into the melt by the end of the test (Tab. 2.2.6.8), g	Calculated final melt composition (5-7+8), g	Final melt composition (ingot + skull), XRF data (Tab. 2.2.6.2), g	Imbalance Δ (9-10) Only for U,Zr, Fe g
	1	2	3	4	5	6	7	8	9	10	11
U	1310.0	67.75	1242.25		1242.25	12.4	32.4	-116.95	1092.9	1082.62	10.28
Zr	417.5	10.49	407.01		407.01	0.3	0.3	-29.36	377.35	343.90	33.45
Fe		6.82[1]	-6.82	137.4	130.58[1]	85.0	231	137.84	37.42	34.65	2.77
Cr				35.6	35.6	26.4	32.1	3.69	7.19		
Ni				20.7	20.7	5.4	15.5	-0.03	5.17		
Mn				2.6	2.6	1.5	1.8	0.88	1.68		
Ti				1.0	1	0.0	0	-0.11	0.89		
Impur.	222.4	18.55	203.85	1.4	205.25	1.7	4.4	-7.21	193.64	238.23	
Total	**1949.9**	**103.60**	**1853.11**	**198.7**	**2044.99**	**132.7**	**317.5**		1727.49	**1699.40**	

[1] Re. Fe – the iron that did not participate in melting (6.82 g) was subtracted from the amount of introduced iron (137.4 g).

[2] Two large-area filters operated during the test; the 1st one – from the beginning of the test through 22930 sec, and the 2nd one – from 22930 sec till the end of the test. The XRF data were used for calculating masses of the elements composing the aerosols.

Table 2.2.6.2 – Fused products composition by XRF

	Sample	U	Zr	Fe	Impurities and O	Mass, g
		mass %				
Participated in melting	**Ingot**	63.7	20.3	2.0	14.0	
	Skull	64.5	11.8	7.2	16.5	
Did not participate in melting	**Crust**	42.1	8.5	21.1	28.3	
	Rod	65.9	21.6	0	12.5	
		г				
Participated in melting	***Ingot***	1074.43	342.40	33.73	236.14	**1686.7**
	Skull	8.19	1.50	0.91	2.10	**12.7**
	Total	**1082.62**	**343.90**	**34.65**	**238.23**	**1699.40**
Did not participate in melting	***Rod***	9.82	3.22	0	1.86	**14.9**
	Crust	13.60	2.75	6.82	9.14	**32.3**
	Spillages	44.33	4.52	-	7.55	**56.40**
	Total	**67.75**	**10.49**	**6.82**	**18.55**	**103.60**

Table 2.2.6.3 – Spillages composition*

	Loaded into the furnace		Spillages		In terms of element
	g	%	g		g
UO_2	1371.6	89.17	50.29	**U**	44.33
ZrO_2	166.5	10.83	6.11	**Zr**	4.52
				O	7.55
Total	**1538.1**	**100.00**	**56.4**		**56.4**

* Spillages were not analyzed; their composition was calculated assuming them to be composed of UO_2 and ZrO_2 only in the proportion of crucible charge.

Table 2.2.6.4 – Introduced steel composition

Introduced steel	S	Si	Mn	Cr	Ni	Ti	P	Cu	Fe	Total
mass %	0.004	0.55	1.31	17.9	10.4	0.48	0.034	0.18	69.142	100
g	0.01	1.09	2.60	35.57	20.66	0.95	0.07	0.36	137.39	198.7

Table 2.2.6.5 – Interaction zone volume and mass

Layer in the interaction zone	Volume, mm^3	Density*, g/cm^3	Mass by the end of the test, G
Pore	8890	-	-
Upper layer	16043	10.76	172.61
Lower layer	18510	9.76	180.64
Total	**43443**		**353.25**

*) density calculated on the basis of additivity using the elemental analysis results

Table 2.2.6.6 – Vessel steel initial composition in the interaction zone volume *

XRF data	Si	Mn	Cr	Ni	Mo	V	P	Cu	Co	As	Fe	Total
mass %	0.25	0.49	2.24	1	0.7	0.1	0.02	0.07	0.03	0.003	95.097	
g	0.86	1.68	7.66	3.42	2.39	0.34	0.07	0.24	0.10	0.01	325.30	342.07

*- density – 7.874 g/cm^3

Table 2.2.6.7 – XRF and SEM/EDX data on the interaction zone composition

Interaction zone layer	U[1)]	Zr[1)]	Fe[1)]	Cr	Ni	Mn	Ti	Impurities
	mass %							
Upper	39.50	5.50	50.00	1.01	0.945	0.215	0.03	2.800
Lower	27.00	11.00	56.00	1.23	1.005	0.24	0.03	3.495
	G							
Upper	68.18	9.49	86.31	1.74	1.63	0.37	0.05	4.83
Lower	48.77	19.87	101.16	2.22	1.82	0.43	0.05	6.31
Total	**116.95**	**29.36**	**187.46**	**3.97**	**3.45**	**0.80**	**0.11**	**11.15**

[1)] SEM/EDX data on U, Zr and Fe; XRF data on Cr, Ni, Mn and Ti

Table 2.2.6.8 – Quantity of vessel steel that has transited into the melt by the end of the test

Element	Initial composition of the interacting vessel steel, g	Final composition of the interaction zone, g	Transited into the melt, g
Fe	325.30	187.46	137.84
Cr	7.66	3.97	3.69
Ni	3.42	3.45	+0.03
Mn	1.68	0.80	0.88
Ti		0.11	+0.11
Impurities	3.94	11.15	+7.21
U		+116.95	
Zr		+29.36	

Fig. 2.2.3 presents a diagram of the material balance for MC9 concerning the main components.

A slight discrepancy between the final melt composition analytical and calculated values is explained by the error in calculation of the vessel steel/molten corium interaction zone volume, as well as by analysis errors.

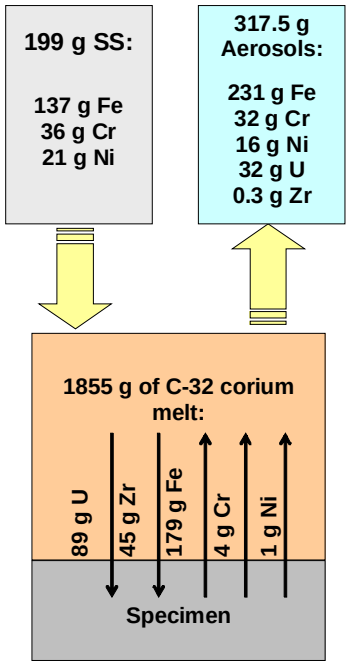

Fig. 2.2.3 – Material balance diagram for MC9 concerning the main components.

2.2.7. Fused corium density

The bottle density of fused corium was determined from the average sample prepared by quartering [10]. Ethyl alcohol was used as a picnometric liquid. The results of density determination under normal conditions are presented in Tab. 2.2.7.

Table 2.2.7 – Fused corium bottle density determination

Sample	Fused corium particle size, mm	Bottle density, g/cm^3
Corium average sample	100-200	8.51

The density evaluation error was ± 0.02 g/cm^3.

In comparison to MC6 (8.52-8.78 g/cm^3), MC7 (8.66-8.81 g/cm^3) and MC8 (8.56 g/cm^3), the bottle density of fused corium was lower in MC9 due to a lower content of uranium as the result of its transition into the specimen (interaction zone).

2.2.8. Metallographic investigations

The performed investigations included:

- Pre-test inspection of steel;
- Steel analysis after the interaction with molten corium.

Pre-test inspection of steel

Like for the tests MC5 – MC8, the specimen for MC9 was made from 15Kh2NMFA-A vessel steel.

Metallographic pre-test inspecion of the witness specimen included analysis of its macro- and microstructure, and microhardness measuring.

Metallographic investigations and microhardness measurements were performed in the same way as in the pervious tests and showed the initial microstructure of steel to consist of the finely-dispersed pearlite, and the integral microhardness of the witness specimen H_μ = 250 – 260.

Initial specimen dimensions measurement

The dimensions were measured with the calipers with a scaling factor of 0.02 mm (20 μm) and the MBC-9 stereoscopic microscope with a 14 μm scaling factor and x50 magnification. The distance A from the upper top to the first groove, distance B to the reference hole axis and diameter D of the reference hole are given in Tab. 2.2.8.1. The points of measurements are shown in Fig. 2.2.8.1.

Table 2.2.8.1 – Steel specimen measurements (mm)

A_1	A_2	A_3	A_4	B_1	B_2	D_1	D_2
3.38	3.42	3.39	3.40	4.95	4.97	2.12	2.24

Specimen length L = 103.9 mm

Steel specimen profilograms

Templates have been prepared from the oxidic corium and steel specimen after the test. The template of the steel specimen axial section was used for measirng the specimen ablation, determining boundaries of the interaction zone and of changes in the macro- and microstructure of steel. Figs. 2.2.8.2 and 2.2.8.3 show corium cutting patterns and the steel specimen axial section.

Fig.2.2.8.4 shows profilograms of the zones that had formed in the steel specimen. Profile of the steel specimen upper top has been plotted using the PMT-3 microhardness tester at x180 magnification, and the MBC-9 stereoscopic microscope at x50 and x100 magnifications. The scale factor of micrometer screws and object plate of microhardness tester is 0.01 mm (10 μm). The measurement error is ±10 μm; it was determined with stage micrometer. The position of the initial top plane was determined from the groove made in the specimen lateral surface at the distance of 3.4 mm from the upper top. The images produced by processing macrosection photographs on the computer were used for plotting all the characteristic boundaries (profiles). Dimensions: specimen width (diameter) – along the X-line; height from the reference plane of the initial top – along the Y-line (top-down).

According to the results of measurements, the interaction zone upper boundary (gas pore boundary) has deepened for 7.35 mm relative to the initial position of the specimen top, while the depth of the corium/steel interaction zone reached 15.55 mm.

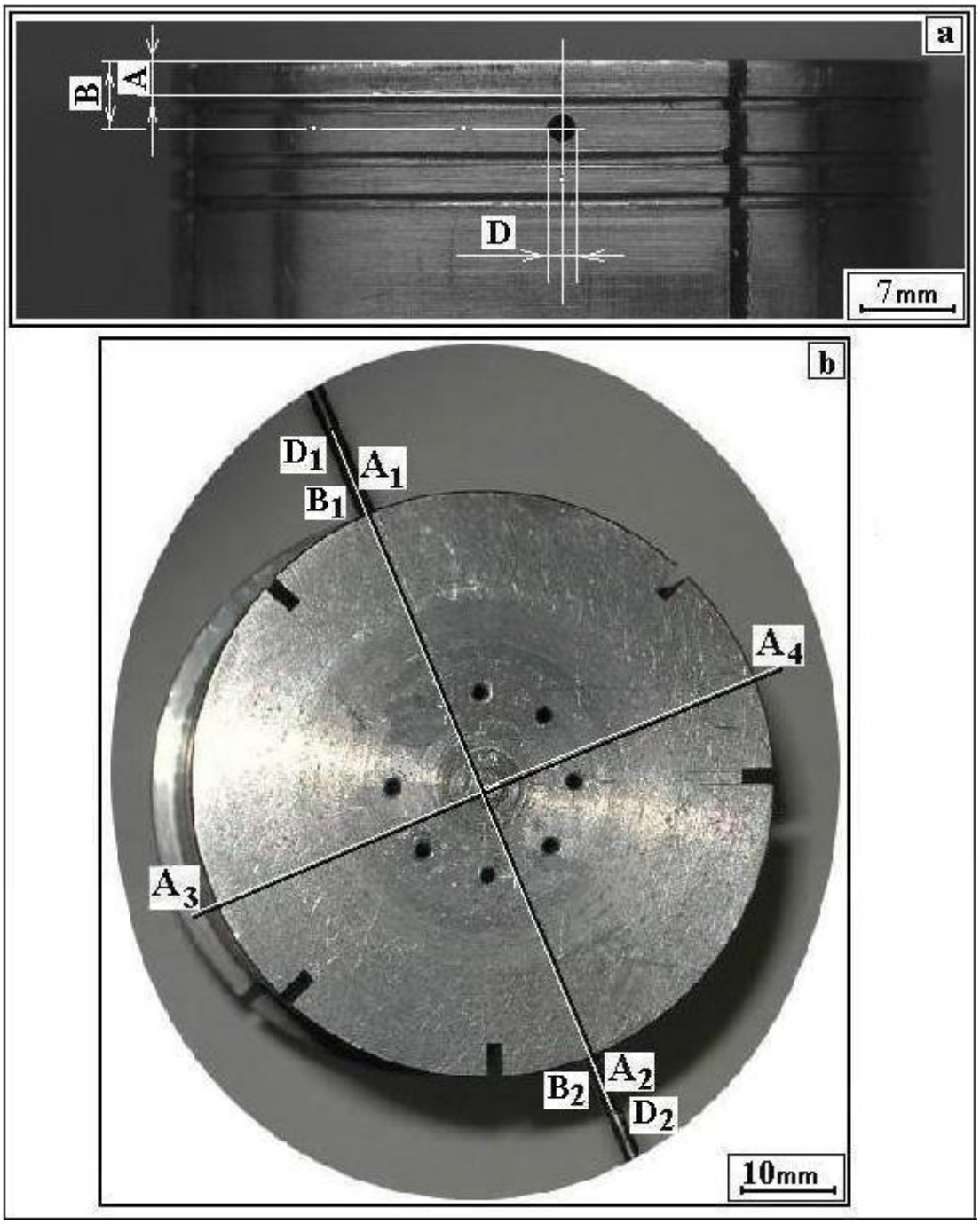

A (A_1, A_2, A_3, A_4), B (B_1, B_2), D (D_1, D_2)- points of measurements

Fig. 2.2.8.1 – Fragments of steel specimen lateral surface (a) and upper top (b) before MC9

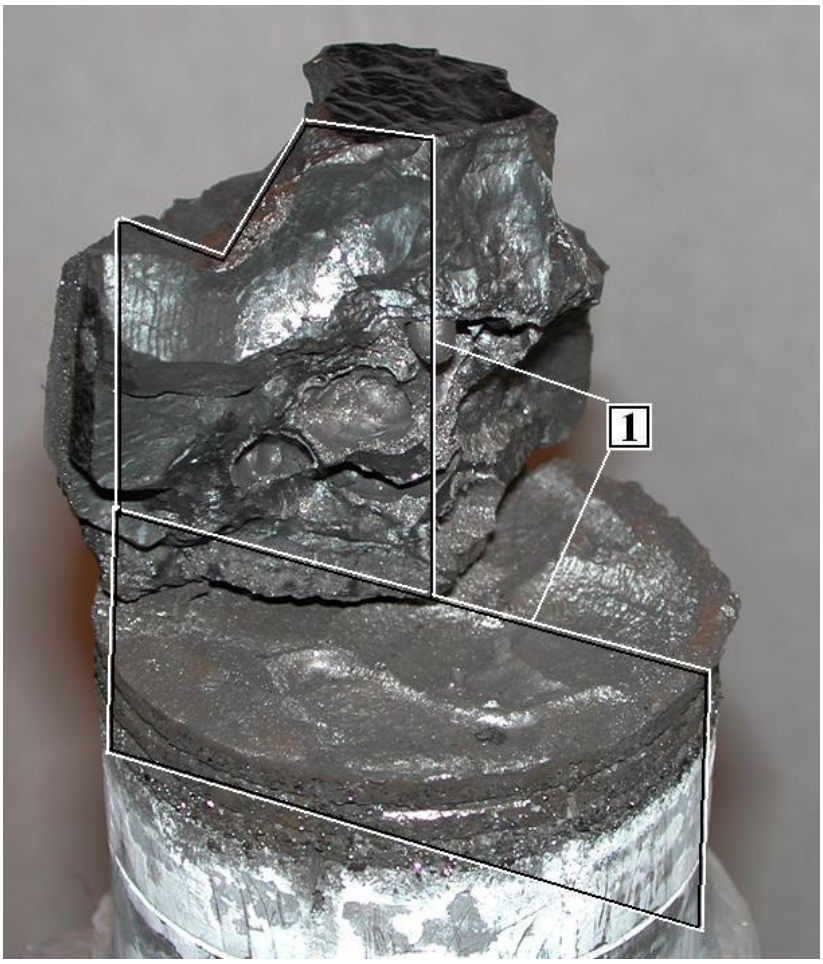

1 – longitudinal cutting plane

Fig. 2.2.8.2 – Corium and steel specimen cutting pattern

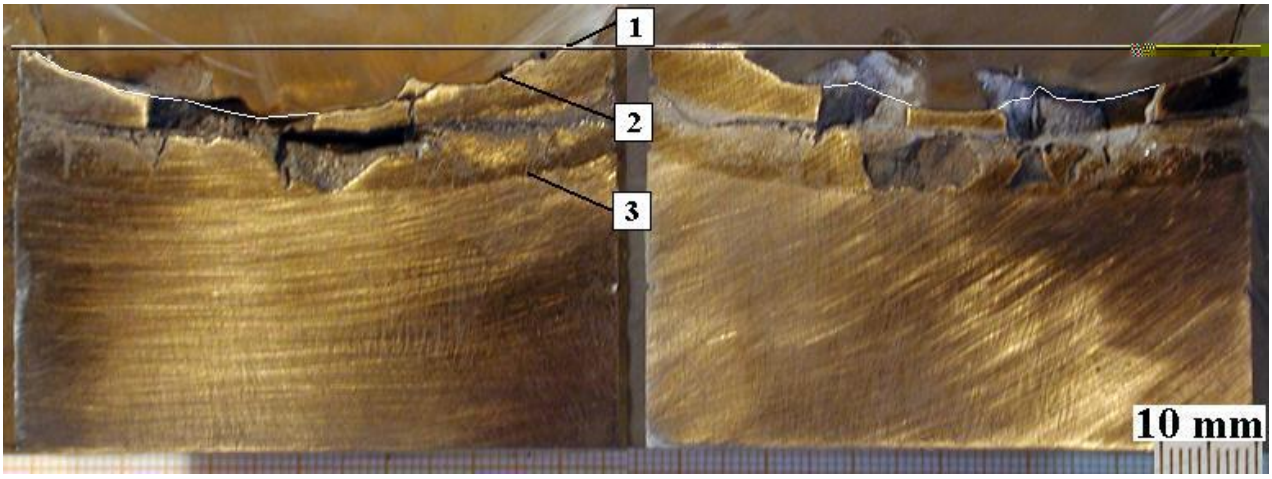

1 – reference plane of the initial upper top;
2 – profile of specimen top after the test;
3 – corium/specimen interaction zone boundary

Fig. 2.2.8.3 – Templates of the axial (longitudinal) cut of the steel specimen upper part

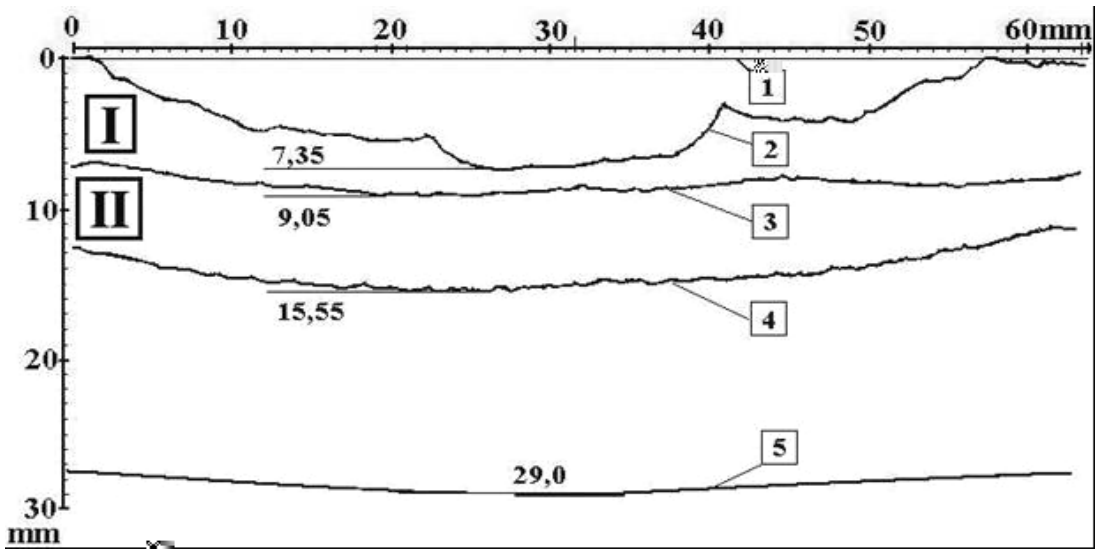

1 – position of the initial top plane;
2 – boundary of the pore that had formed under the skull (profile of the steel specimen upper top after the test);
3 – boundary between the upper and lower parts of the interaction zone;
4 – interaction zone/specimen boundary;
5 – boundary of changes in macro-and microstructure of the steel specimen.

Fig. 2.2.8.4 – Profiles of the zones that had formed along the steel specimen axial section

Steel macro- and microstructure after the test

Grinding and polishing of the templates was done according to the standard technique.

In order to reveal the microstructure, the prepared microsection was etched and quality was controlled by the metallographic microscopes. The etchants for both pearlitic and austenitic steels [11] were used; their combination made it possible to reveal the macro- and microstructure in the zone of molten corium high-temperature influence, macro- and microstructure of the corium/steel interaction zone, as well as identify the microstructure of steel.

The surfaces of microsections were photographed by a NIKON digital camera coupled with the METALLUX metallographic microscope at x200, x400 and x900 magnifications.

Fig. 2.2.8.5 shows the macrostructure of the vessel steel specimen longitudinal section, with marked boundaries of the interaction zone and of thermal influence (numbering corresponds to Fig. 2.2.8.4), as well as of the areas where steel microstructure was studied.

Figs. 2.2.8.6 – 2.2.8.10 (below) show steel microstructure in different zones of the ingot marked in Fig. 2.2.8.5.

The area, within which structural transformations occured in the specimen, spreads to a depth of 28 – 29 mm from its upper top.

The type of the resulting steel microstructure depends on the temperature gradient along the steel specimen height, development of diffusion and recrystallization processes during the test, and on the content of carbon in the mentioned zones. The specimen macro- and microstructure above line ***(5)*** (Fig. 2.2.8.9) underwent transformations as the result of carbon and chromium repartitioning. This zone may be regarded as local formations of steels with different content of

carbon and alloying elements. The microstructure of steel areas near line ***(4)*** consists mainly of ferrite with the carbon content of 0.02 %. Formation of a "new" ferrite-pearlite structure has occurred between lines ***(4)*** and ***(5)***. Formation of such a microstructure may occur at cooling of the steel heated above the critical point Ac_3 from the austenitic state, repartitioning of carbon, and a relatively high cooling rate. In such a case, different modifications of pearlite may be obtained, that is, sorbite, troostite or martensite, even with the given small quantity of carbon. The forming acicular pearlite may lead to an increased strength and hardness of steel and, simultaneously, a reduced impact strength and tensile strain..

The structure changes to the finely-dispersed pearlitic in the zone of line ***(5)***. The marked out area - line ***(5)***, 1.5 - 2 mm wide, determines the boundary of thermal influence exerted by the high-temperature molten corium on the steel specimen. The microstructure of this zone is pearlitic (Fig. 2.2.8.8), showing spheroidizing of the initial pearlitic structure. The microstructure above and below line ***(5)*** is shown in Figs. 2.2.8.9 and 2.2.8.10. Further, below the transitional zone, microstructure of the initial steel remains intact.

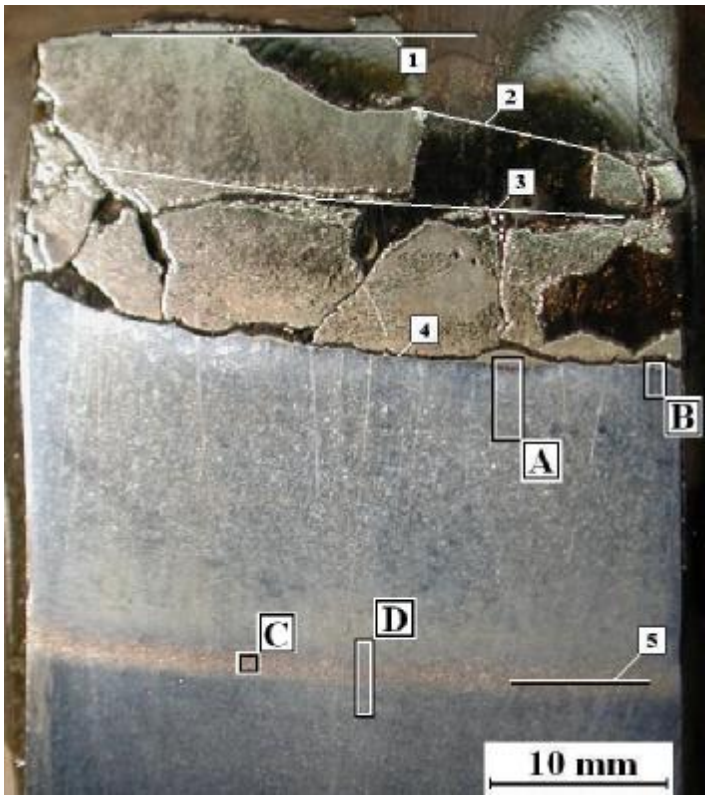

A–D – microsection areas where microstructure was photographed

Fig. 2.2.8.5 – Macrostructure of the steel specimen upper part longitudinal section

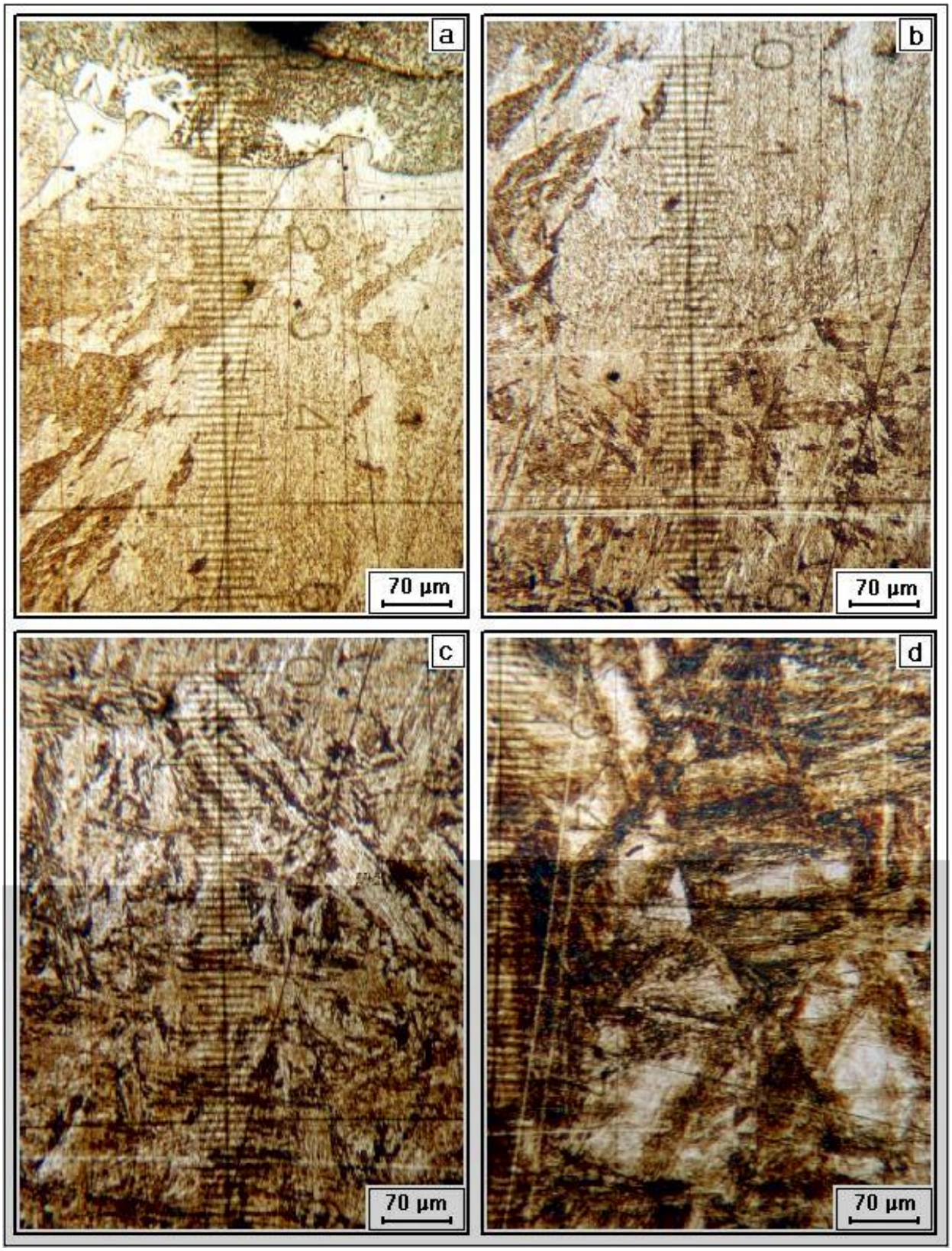

Fig. 2.2.8.6 – Steel microstructure below line (4), area A (etchants for austenitic steels)

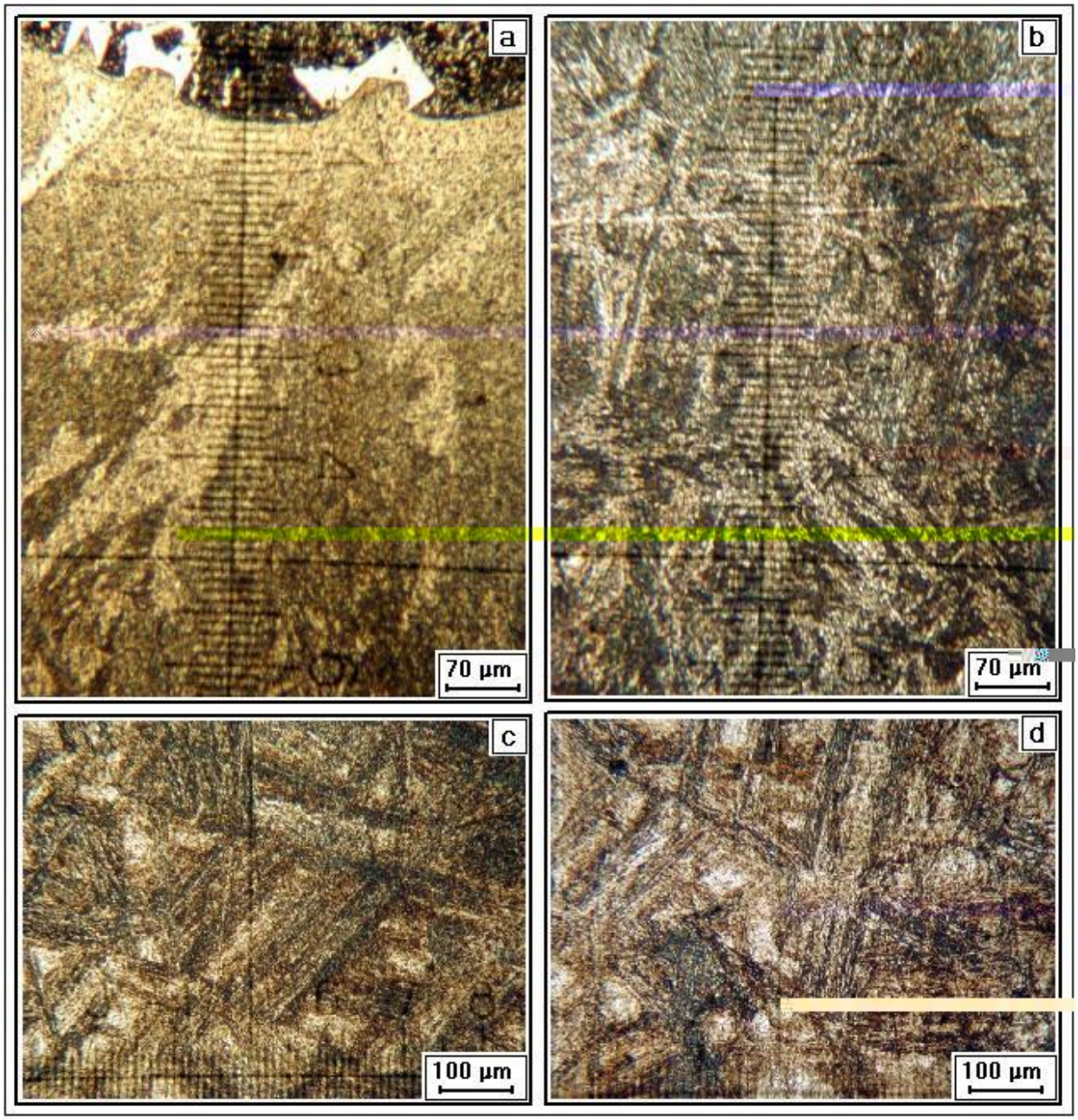

Fig. 2.2.8.7 – Steel microstructure below line (4), area A (etchants for pearlitic steels)

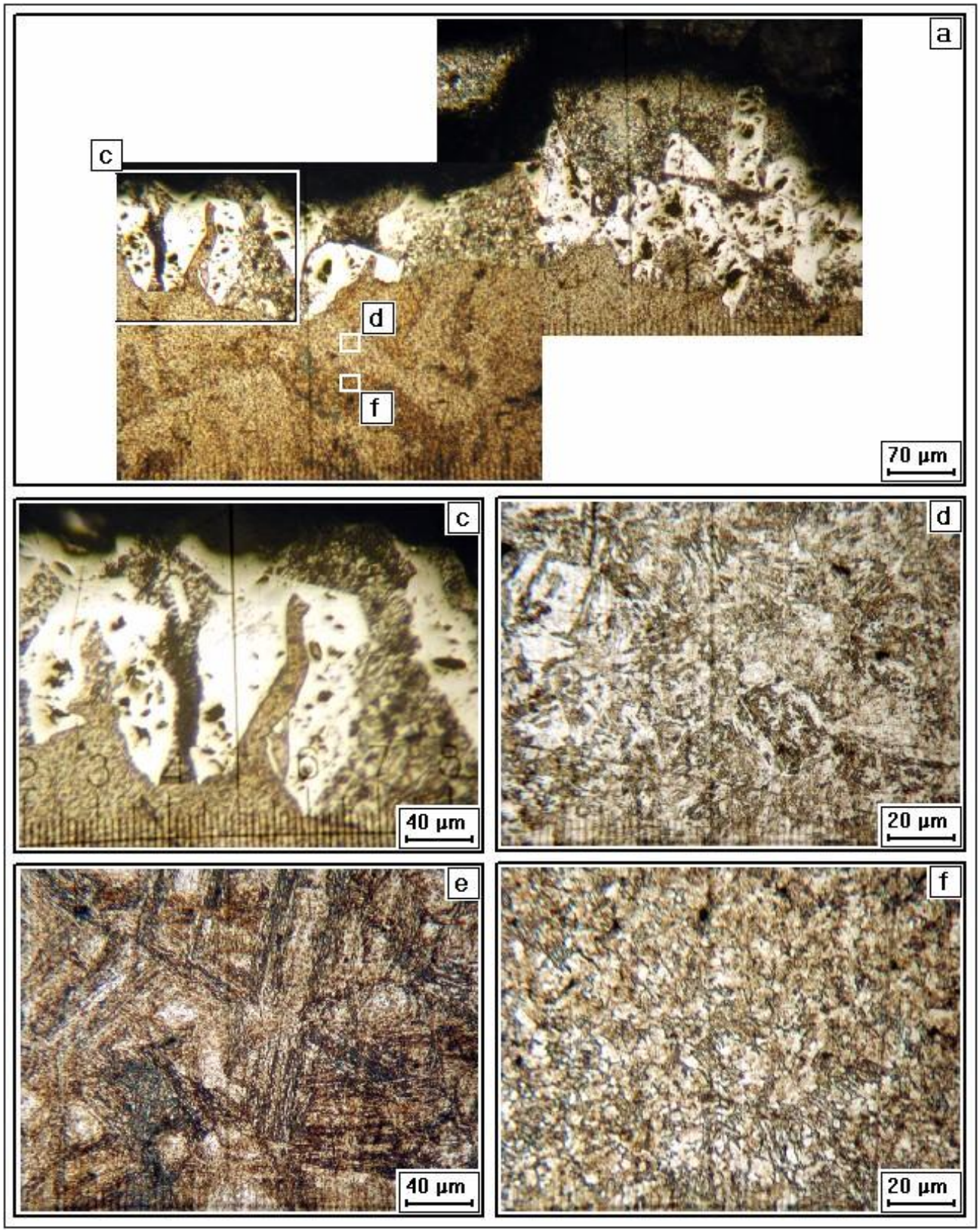

Fig. 2.2.8.8 – Steel microstructure below line (4), area (B) (etchant for pearlitic steels)

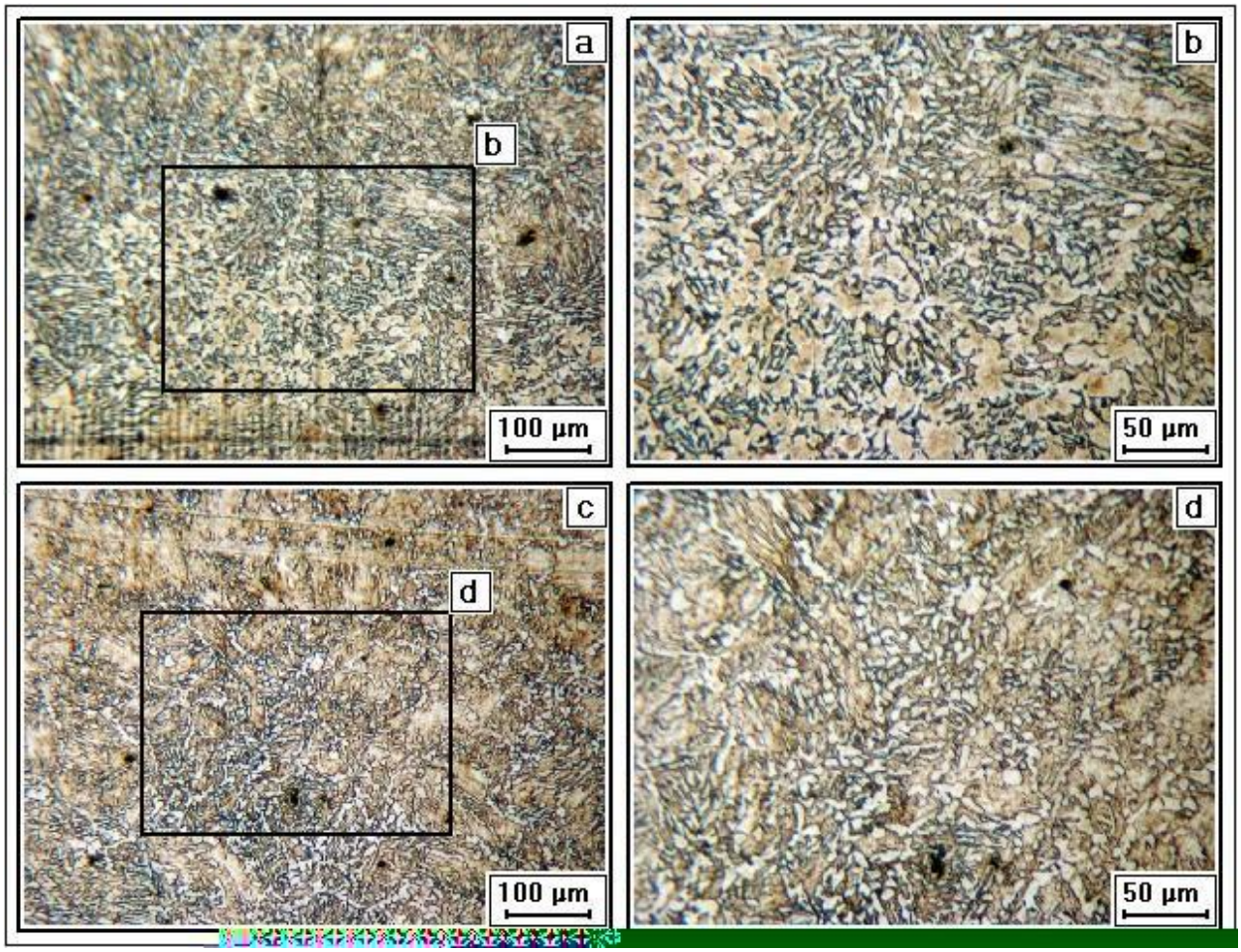

Fig. 2.2.8.9 – Steel microstructure (above line 5) with magnified (b and d) fragments of area (C)

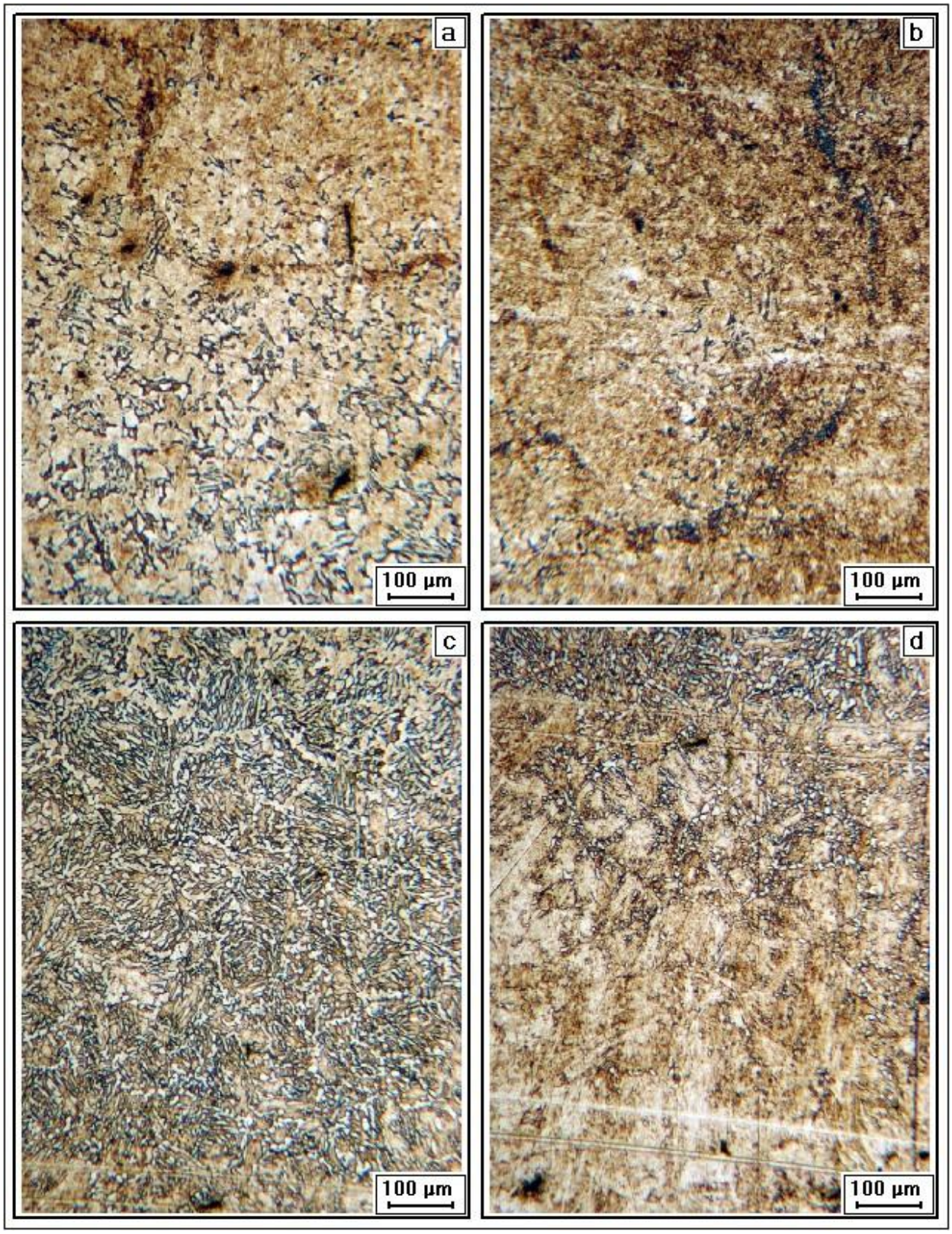

Fig. 2.2.8.10 – Steel microstructure with magnified fragments – area (D) below line 5

2.3. Numeric modeling of the specimen temperature conditions

The calculations were aimed at determining the temperature conditions under which the melt interacted with the specimen and, primarily, of the temperature at the interaction zone/specimen boundary after it has reached the final position. Proceeding from this aim, the specimen temperature condition at the final stage of the test has been modeled. According to the results of posttest analyses, the melt was practically oxidic at the end of the test. The calculations of heat fluxes and electromagnetic forces distribution in the oxidic melt and of its thermal hydrodynamics have yielded the radial distribution of heat flux density at the specimen upper top (see Fig. 2.3.1). Evidently, the maximum heat supply is in the central part of the top. The procedure of the above calculations is described in [12]. The procedure of calculating the specimen temperature conditions did not differ from that previously applied for analyzing the results of MC5…MC8 [1]. The results of calculations for MC9 are given in Figs. 2.3.2 – 2.3.4. The best agreement between the calculated and experimentally obtained temperature values was achieved when the average density value of the heat flux to the specimen upper top (to the interaction zone surface) was 1.1 MW/m^2. The calculated power into the top calorimeter is 2.19 kW, this value being close to the experimentally obtained one (2.03 kW). It should be noted that the comparison of calculations with the test used only the unquestionably reliable thermocouple readings. Besides, the given calculation results were obtained when radially uniform distribution of heat flux density was specified (instead of the given in Fig. 2.3.1), as only in this case the optimal agreement between the calculations and the test was achieved. The possible reasons of the said effect are discussed in Section 3.4. It is evident from Fig. 2.3.4 that the temperature at the interaction zone/specimen boundary (T_{bndry}) is within the 1060…1100 °C range. Like in most tests of the MC series, calculations of T_{bndry} value yielded a range of values which is due to the asymmetrical attitude of the interaction boundary, apparently mainly because of the asymmetrical heat sink down the specimen lateral surface. Therefore, the numeric modeling using the axis-symmetrical formulation inevitably leads to the mentioned range of T_{bndry} values. The same figure shows a boundary between two layers within the interaction zone (see Section 2.5 for their peculiarities) and a boundary of the so-called thermal influence on steel structure which coincides with the 730 °C isotherm. The latter value is close to the boundary temperature of transtition from the pearlitic to pearlite-ferritic structure of carbon steels, and it indirectly confirms the sufficient accuracy of calculations.

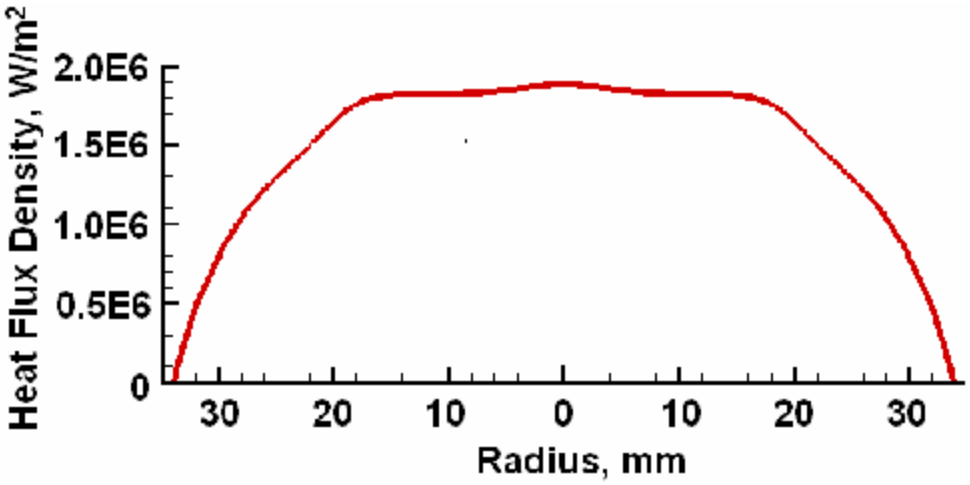

Fig. 2.3.1 – Distribution of heat flux density

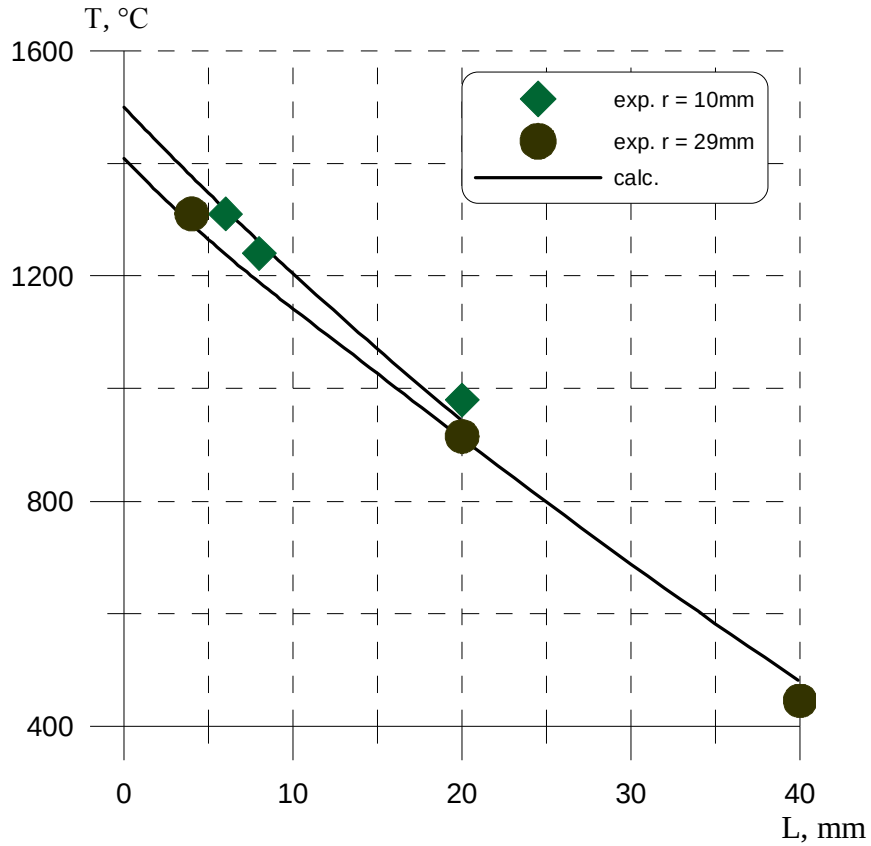

Fig. 2.3.2 – Distribution of temperature along the specimen height

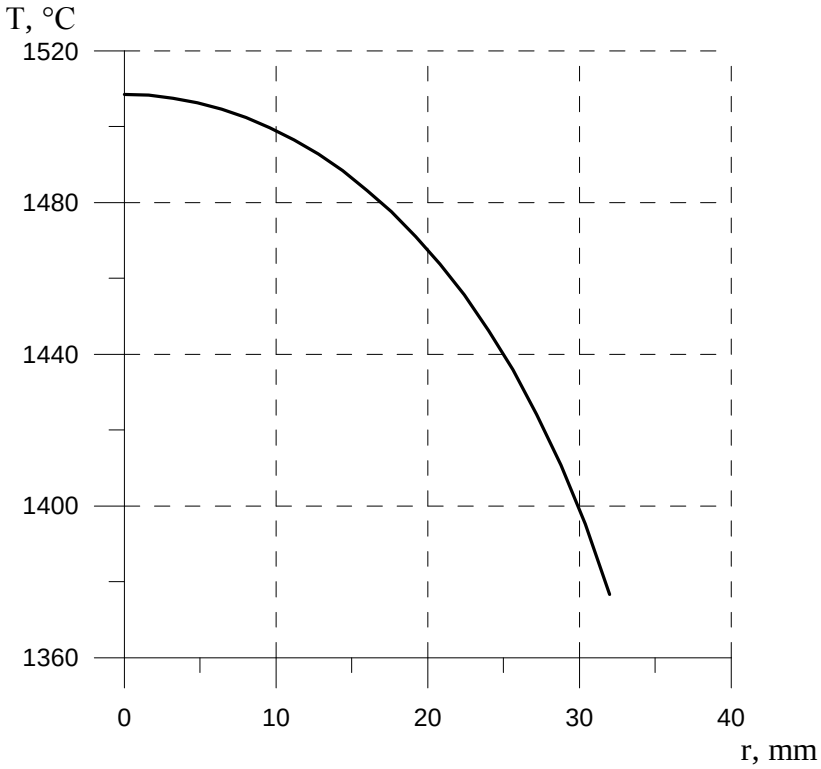

Fig. 2.3.3 – Radial temperature distribution at the specimen upper top

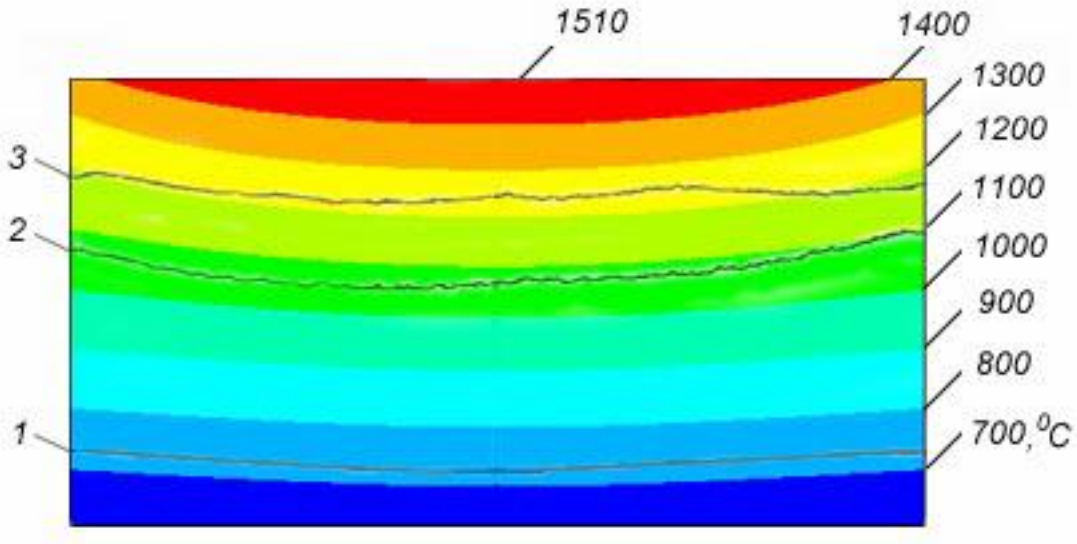

1 – boundary of the area of thermal influence on steel structure (730°C)
2 – interaction zone boundary (1060-1100°C)
3 – boundary of layers within the interaction zone (1170-1250°C)

Fig. 2.3.4 – Temperature field in the specimen (fragment)

2.4. Ultrasonic measurements of the specimen ablation rate

Like in the previous tests, the aim of ultrasonic (US) measurements in MC9 was to determine the kinetics of progress of the corium/vessel steel interaction zone boundary. The measurement and data processing procedures were described in detail in the MC5, MC6, MC7 and MC8 reports [1]. Test MC9 was started with the following values of the main parameters (Tab. 2.2.1).
Test MC9 was started with the following values of the main parameters (Tab.. 2.4.1).

Table 2.4.1 – Initial values of main parameters

Parameter	Notation	Value	Unit	Note
Total specimen length	$L_{tot.}$	103.9	mm	
Distance from the defect to the 1st point of temperature measurement	l_1	0.04	mm	6.00 mm from top
Distance from the defect to the 2nd point of temperature measurement	l_2	4.04	mm	2.00 mm from top
Initial distance from the defect axis to top	D_o	4.95	mm	
Initial speed of sound in the specimen	C	5.89	km/s	

The value determined in the test for $b = \frac{C_0 - C(T)}{TC(T)}$ was $1{,}9 \cdot 10^{-4}$ $(^oC)^{-1}$.

Fig. 2.4.1 shows a plane view of echogram from MC9 processed by the subtraction method [1]. The Y-line shows the echogram scanning time τ (μs). Curve 1 characterizes the temporal position of a signal reflected from the interaction zone lower boundary.

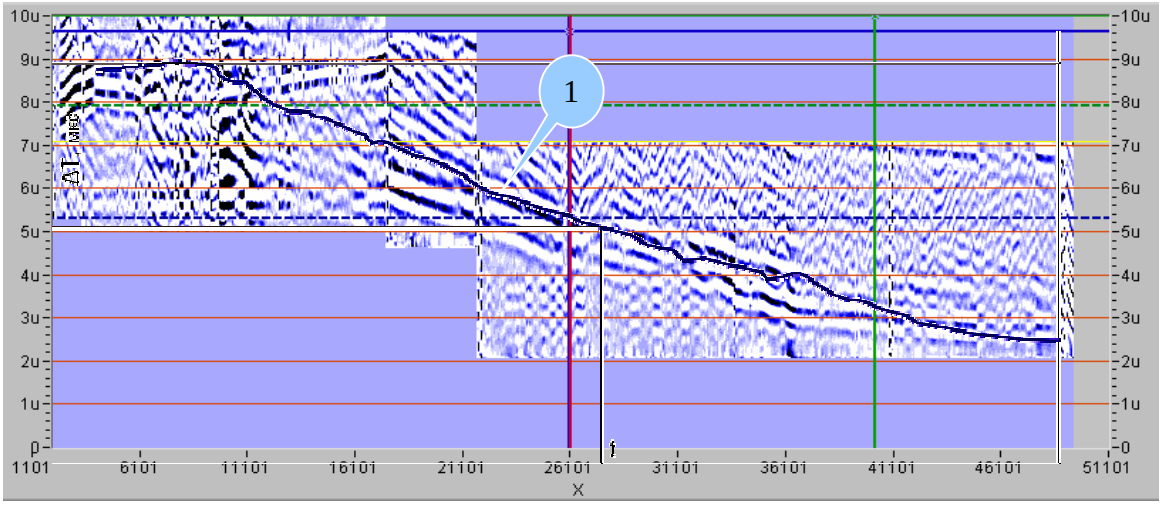

Fig. 2.4.1 – Plane view of echogram processed by the subtraction method

Fig. 2.4.2 shows the true depth of the interaction zone, measured from the initial position of the specimen top, as a function of the test time H(t).

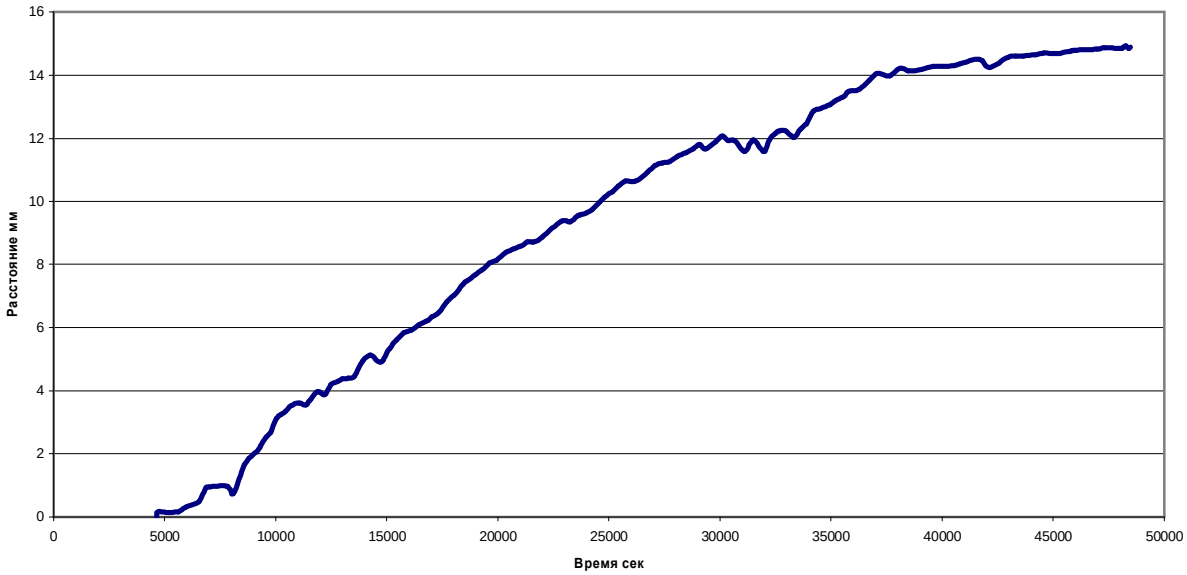

Fig. 2.4.2 – Evolution of the interaction zone depth in MC9

The convertion of Δτ(t) (Fig. 2.4.1) into H(t) (Fig. 2.4.2) used the correlations

$$\frac{1}{2}\,\Delta\tau(t) = \int_0^{H(t)} \frac{dl}{C(l)} \qquad (1)$$

where $C(l)=C_0 / (1+\beta T(l))$, $T(l)=T_s+\frac{dT}{dl} l$;

T_s and $\frac{dT}{dl}$ are the top surface temperature and the temperature gradient in the specimen, respectively;

Ts= 1510 ^oC, $\frac{dT}{dl}$ = – 23.5 ^oC/mm (determined from the thermocouple readings by the least-squares method).

From (1) we finally obtain:

$$H(t)= \frac{C_0 \Delta\tau(t)}{(1+\beta T_s)+\sqrt{(1+\beta T_s)^2+\beta \frac{dT}{dl} C_0 \Delta\tau(t)}}. \quad (2).$$

It should be noted that if H_{max} is determined from (2), then expression (2) may be replaced with a simpler approximate expression

$$H(t)= \frac{\frac{1}{2} C_0 \Delta\tau(t)}{1+\beta\left(T_S+\frac{dT}{dl}\cdot\frac{H_{max}}{2}\right)}. \quad (3).$$

For the conditions of MC9, the maximum absolute difference of (2) from (3) for H(t) is~ 0.1 mm reached in the point $H(t)=\frac{H_{max}}{2}$, while the maximum relative difference of (2) from (3) amounts to ~ 2.5% at $H(t)\to 0$.

Notable is that none of the above evaluations use the data on signals reflected from the defect in the specimen. However, id does not follow that the defect is not needed at all. The defect is useful, at least for determining the value of β, for recording changes in the temperature field in the space between the defect and the US sensor and introducing corresponding corrections to the results of US measurements, especially when positional changes of the reflecting surfaces are small and high precision is required.

It follows from the data given in Fig.2.4.2 that:

1. In MC9, the corium/vessel steel interaction zone lower boundary starts propagating at 1.5 mm/h and gradually slows down to 0.2 mm/h by the time of heating disconnection.

2. According to the results of US measurements in MC9, the maximum depth of the interaction zone (H_{max}) is 14.9 mm, it being in agreement with the posttest measurements: $H_{max\ exp.}$ = 15.6 mm.

2.5. SEM/EDX analysis

Aerosols

The studied template, representing a section of the sintered aerosols flake removed from the crucible wall, is shown in Fig. 2.5.1. The results of SEM/EDX analysis of aerosols are given in Figs. 2.5.2 - 2.5.4 and Tabs. 2.5.1, 2.5.2.

The SEM data allow a conclusion that aerosols represent a highly porous spongy structure, consisting predominantly of the crystallized droplets of steel (Fig. 2.5.2, Tab. 2.5.1, point P1; Fig. 2.5.3, Regs. 2 and 3; Fig. 2.5.4, Reg. 4). There also occur the UO_2-based phase and the ZrO_2 phase (Fig. 2.5.3, Tab. 2.5.2, points P1 and P2, respectively). The SEM/EDX data obtained for aerosols suppose two possible mechanisms of their formation: 1) evaporation – condensation in steam – deposition of the refractory components UO_2 and ZrO_2 in the form of ~ 1 μm droplets and films; 2) evaporation and condensation on the surface of the fusible, most volatile components - Fe, Cr and Ni - in the form of ~ 1 μm droplets. It should be noted that the refractory components occupy ~ 1 vol. % of all aerosols, and their distribution within the volume is sufficiently even.

The layered structure of aerosols observed in Region 4 (Fig. 2.5.4) may be due to such peculiarities of the test, as superheated steel evaporation, changing of the temperature regime, etc. The nature of large crystallized steel formations is connected with intensive evaporation of the superheated steel during its presence in the molten pool and with the subsequent agglomeration of the deposited aerosols.

Ingot oxidic part

A polished section of a half of the longitudinal section of the ingot oxidic part (Fig. 2.5.5) have been prepared for SEM/EDX examination. The crystallized corium away from the interaction zone (Fig. 2.5.5, Regions 4, 5, 6, 8 and 9), corium near the interaction zone (Fig. 2.5.5, Region 7), ingot peripheral part (Fig. 2.5.5, Regions 2 and 3) and drop-shaped inclusions (Fig. 2.5.5, Regions 1, 5 and 8) have been studied.

The analysis of bulk corium far away from the interaction zone shows the presence of ~ 0.5 mass % of iron in the crystallized corium upper part (Fig. 2.5.5, 2.5.9, Region 4, Tab. 2.5.6, Area SQ1). The microstructure in this region, as well as in regions 6 and 9 (Figs. 2.5.5, 2.5.11 and 2.5.14) is analogous to that observed in the previous tests MC6 and MC7. The EDX examination of Regions 2 and 3 (Figs. 2.5.5, 2.5.7 and 2.5.8) demonstrates the absolute absence of iron in the peripheral parts of the crystallized ingot.

Investigation of corium near the interaction zone (Figs. 2.5.5, 2.5.11, 2.5.12, Regions 6 and 7) has identified a sufficiently distinct boundary between the region with a relatively small iron content (~ 1 mass %) (Fig. 2.5.11, Region 6, Tab. 8, SQ1) and the region containing 6 mass % of iron and somewhat poorer in zirconium in comparison with the oxidic melt that had crystallized in Region 6 (Fig. 2.5.12, Tab. 2.5.9, SQ1).

Also studied were the drop-shaped inclusions which had formed both in proximity to the interaction boundary (Figs. 2.5.5, 2.5.6, Region 1) and in the central part of the crystallized ingot (Figs. 2.5.5, 2.5.13 and 2.5.10, Regions 8 and 5). The analysis of drop-shaped inclusions showed that before crystallization they represented a melt containing such components as U-Zr-Fe-Ni-Cr-O and were close in terms of bulk composition. However, microstructurally the drop-shaped inclusions differ quite much. At least 6 phases may be distinguished in the microstructure of the crystallized drop-shaped inclusions:

- The $U_6Fe(O)$-based phase with a small amount of nickel (Fig. 2.5.6, Region 1-1-2, Tab. 2.5.3, Point P1; Fig. 2.5.10, Region 5-1-1, Tab. 2.5.7, Point P1) has been recorded for all the studied inclusions.
- The uranium monoxide-based phase with small amounts of zirconium and iron (Fig. 2.5.6, Region 1-1-2, Tab. 2.5.3, Point P2) is present in the drop-shaped inclusion close to the boundary with steel.

- The $(Zr,U)_2Fe(Ni)(O)$-based phase (Fig. 2.5.10, Region 5-1-1, Tab. 2.5.7, Point P2).
- (Zr,U)Fe(O)-based phase (Fig. 2.5.10, Region 5-1-1, Tab. 2.5.7, Point P3) has been identified in the drop-shaped inclusion from the ingot central part.
- The $Zr(U)Fe(Cr,Ni)_2(O)$-based phase (Fig. 2.5.6, Region 1-1-2, Tab. 2.5.3, Point P3), is the basic one in the drop-shaped inclusion located in proximity to the interaction boundary in the iron-enriched layer.
- The $ZrO_{0.33}$-based phase with small amounts of iron, nickel and uranium (Fig. 2.5.10, Region 5-1-1, Tab. 2.5.7, Point P4) has been recorded for the drop-shaped inclusion from the ingot central part.

It should also be noted that the drop-shaped inclusion adjacent to the interaction boundary features oxidic globules which serve as the centres of crystallization in the region (Fig. 2.5.6, Region 1-1-1) and testify to the high oxygen potential of the final liquid.

The considered drop-shaped inclusions might have formed due to the displacement of fusible components into the ingot central part in the course of the oxidic melt cooling and its subsequent stratification into the metallic and oxidic components (Fig. 2.5.13, Fig. 2.5.10). Notable is that smaller quantities of similar inclusions were also observed in MC6.

Another distinctive feature is the extremely high porosity of the central part of the crystallized oxidic melt. It was not observed in the previous tests of the MC series. This feature may be due to a strong shrinkage of the final liquid connected with the release of excessive oxygen during crystallization of the metallized inclusions.

Interaction zone

Macrostructurally, the interaction zone in MC9 represents a two-layer structure with shrinkage cracks distinctly separating the zone from steel and one layer from another. Under the crystallized corium ingot a spacious pore has formed because of shrinkage and due to the considerable evaporation of iron from the steel specimen. It should be stressed that such a macrostructure of the interaction zone is a new effect in the MC experimental series.

Three polished sections have been prepared for SEM/EDX investigations of the interaction zone. Two polished sections represented the interaction zone upper layer with the skull adjacent to the upper boundary (Figs. 2.5.15, 2.5.32) and another section represented a half of the longitudinal section of the steel specimen with the interaction zone (Fig. 2.5.19).

Like in previous tests of the MC series, the EDX analysis of the bulk composition of steel near the interaction zone and in the depth of the specimen did not register noticeable differences (Fig. 2.5.19, Regions 3, 2, 13 and 1; Fig. 2.5.21, Tab. 2.5.14, Point P1; Fig. 2.5.20, Tab. 2.5.13; Fig. 2.5.31, Tab. 2.5.21).

The SEM analysis of the interaction zone distinguishes at least three layers which are sufficiently well separated from one another and possess characteristic microstructure (Fig. 2.5.36).

Let us consider the interaction zone structure along the “steel – crystallized corium” line, i.e., from the side of more fusible compositions.

At the steel/interaction zone boundary, in a layer about 1-2 mm thick (Fig. 2.5.36, layer 1), the microstructure of the zone reminds that of the interaction zone in MC7, that is, cut crystalline formations composed of $Zr(U)Fe_5(O)$ spread throughout the layer and at the very boundary (Fig. 2.5.21, Tab. 2.5.14, Points P2 and P6; Fig. 2.5.22, Tab. 2.5.15, Point P1, Area SQ1; Fig. 2.5.23, Tab. 2.5.15, Points P1 and P3; Fig. 2.5.24). Так The boundary with steel has a tendency to

smoothening following the temperature front (like in MC7), but still it is less smooth than in MC6 and MC8. At the same time, there exist differences with MC7. Microstructurally, the layer shows the dendritic type of crystallization between crystals (Figs. 2.5.21 - 2.5.24). Like in MC6 and 8, it is the iron-based phase that has the dendritic type of crystallization near the boundary with steel (Fig. 2.5.21, Tab. 2.5.14, Point P3), while in the bulk of the considered layer the phase that crystallizes dendritically has a gradiently changing composition of an uninterrupted succession of solid solutions of the U(Zr)Fe_3(O)-type (Fig. 2.5.22, Tab. 2.5.15, Points P2 и P3). In MC7 the said phase crystallizes in the form of 1) separate inclusions surrounded by the eutectically crystallized melt, and 2) as a layer at the interaction zone periphery. Formation of rare crystallites of the U(Zr)Fe_3(O)-type along the boundary with steel should be mentioned (Fig. 2.5.23, Tab. 2.5.16, Point P2). As in all other tests of the series, between the dendrites there is a melt with the eutectic character of crystallization (Fig. 2.5.21, Tab. 2.5.14; Fig. 2.5.22, Tab. 2.5.15, Area SQ3). Unlike in MC7, the porosity observed above the layer in question is slight (Fig. 2.5.25). Though the boundary with the overlying layer is smooth, it could not be correlated with some characteristic isotherm (see Fig. 2.3.4). Besides, no shrinking crack was observed between the overlying layer and the one in question. Apparently, this is associated with similarity of the coefficient of thermal expansion for these layers, or with the possibility of the overlying layer to assimilate or quickly transport the oxygen released by the crystallizing layer below.

The overlying layer thickness (Fig. 2.5.36, layer 2) differs from 0.1 (in Region 7) up to 2 mm. Its microstructure is given in Fig. 2.5.23, 5-3, Fig. 2.5.25, 7-2, Figs. 2.5.26, 2.5.28 and 2.5.29. The basic, apparently, the most refractory phase in this layer is the Zr(U)Fe_3(O) system, which forms the frame structure surrounded by a melt with the eutectic character of crystallization. In the lower part of the layer, a phase composed of Zr(U)Fe_5(O) exists in addition to the frame phase (Fig. 2.5.23, 5-3). The light edging of the frame phase attracts attention. Presumably, it is a solid solution of the U(Zr)Fe_3(O)-type (Fig. 2.5.25). It should be mentioned that the eutectic crystallized around the frame phase is poorer in zirconium, if compared with the eutectic of the below layer.

The next layer (Fig. 2.5.36, layer 3) is separated from the middle layer 2 by a wide shrinking crack. A smooth transition of microstructure between these layers is worth mentioning. The deposition of the ZrO_2–based phase at the boundary between the layers has been recorded. It proves that this layer is better saturated with oxygen than the previous one (e.g., see Fig. 2.5.29). The frame structure in layer 3 is finer and has the dendritic character (Figs. 2.5.16, 2.5.30, 2.5.33), while the dendritically crystallized phase itself is a gradiently changing composition of an uninterrupted succession of solid solutions from Zr(U)Fe_3(O) to U(Zr)Fe_3(O). The crystallized melt between the dendrites also had the eutectic character of crystallization. The eutectic composition is close to the eutectic in the middle layer 2 of the interaction zone (compare, e.g., Fig. 2.5.16, Tab. 2.5.11, SQ3 and SQ4 with Fig. 2.5.26, Tab. 2.5.18, SQ2). Besides the mentioned phases, the (U,Zr)O_2- and (Zr,U)O-based phases rarely occur in the central zone (Fig. 2.5.16, Tab. 2.5.11, Points P1 and P2, respectively). Their presence along with the availability of ZrO_2 confirms the high content of oxygen in the layer.

The bottom skull layer of corium, ~ 500 μm-thick, is separated from the interaction zone by large pores and represents by itself a mixture of the above-described microstructure and rounded grains of the uranium-enriched U(Zr)O_2 solid solution. The latter phase occupies from 20 up to 50 vol. % of all the skull layer and does not form a continuous structure (Figs. 2.5.17, 2.5.18, 2.5.33, 2.5.34).

When considering the distribution of components in the corium-steel ingot along its height, it may be noticed that the concentration of iron is decreasing steadily in the steel-to-corium direction. The crystallized oxidic ingot contains a zone with a considerably high content of iron, which is separated by a smooth boundary from the crystallized corium above, and is adjacent to the interaction zone upper boundary. This zone's peculiar features are the absence of a visible microstructural difference with the above-located crystallized corium, and the absence of a shrinkage crack between these layers. Undoubtedly, the considered structure is not a consequence of crystallization processes and corresponds to some stationary state of the molten pool. Such a structure may be a consequence of the temperature gradient along the melt height, which results in a lower temperature of the pool bottom layers. The melt in the pool bottom layers has a higher viscosity due to the refractory phase crystallization and serves as an obstacle of a kind for levelling of components' concentration in the system.

The abnormal uranium to zirconium ratio in the middle layer of the interaction zone also draws attention. In contrast to the considered layer, such a distribution of components has never been recorded in any crystallized layer of the interaction zone from any test of the MC series. Perhaps, the temperature gradient in the interaction zone was high and the layer in question crystallized from the melt that had formed in the interaction zone along the isotherm of the most refractory component (probably, the $Zr(U)Fe_3(O)$ solid solution) crystallization. This layer kept growing thicker as the interaction front advanced inside the steel specimen. This supposition is corroborated by the microstructure of the zone, which is characteristic of slow crystallization and represents a recrystallized accrete structure with a eutectic in the interphase space.

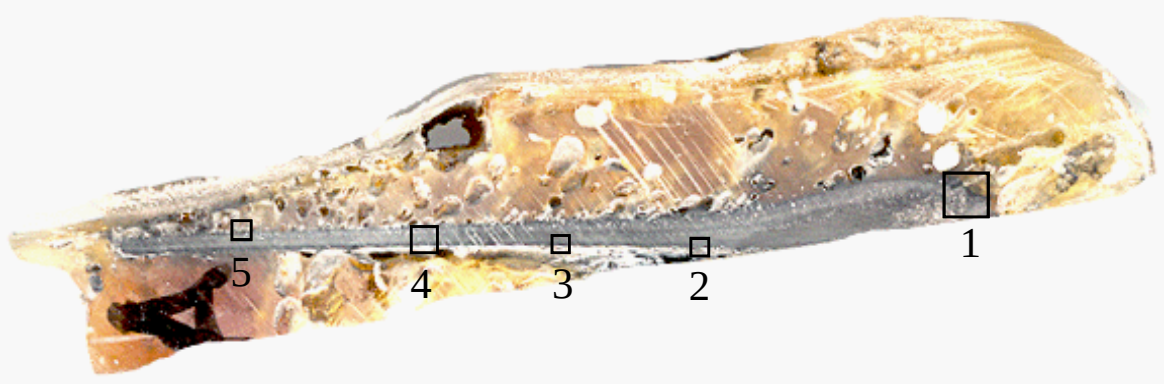

Fig. 2.5.1 – Sintered aerosols template with regions marked for examination

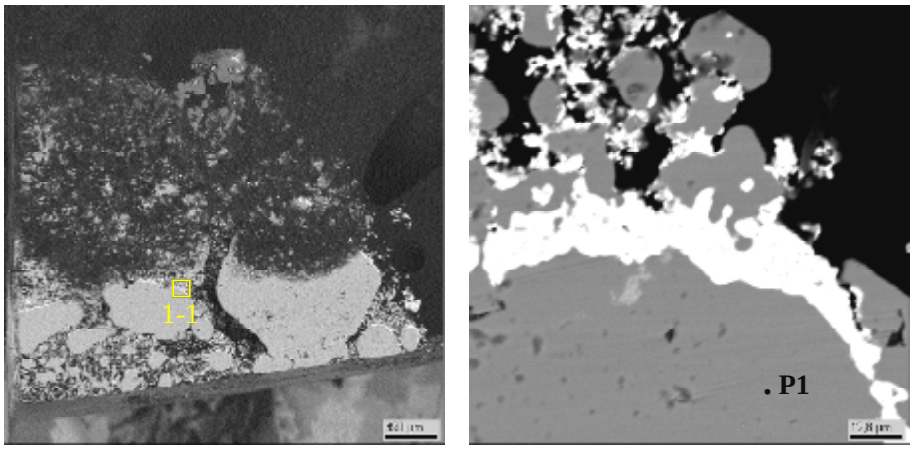

1 1-1

Fig. 2.5.2 – Micrographs of Region 1

Table 2.5.1 – Data on Region 1 EDX analysis

No.		Fe	Cr	Ni	Mn	~O
P1	mass %	67.40	26.95	5.26	0.39	-
	mol.%	66.24	28.45	4.92	0.39	-

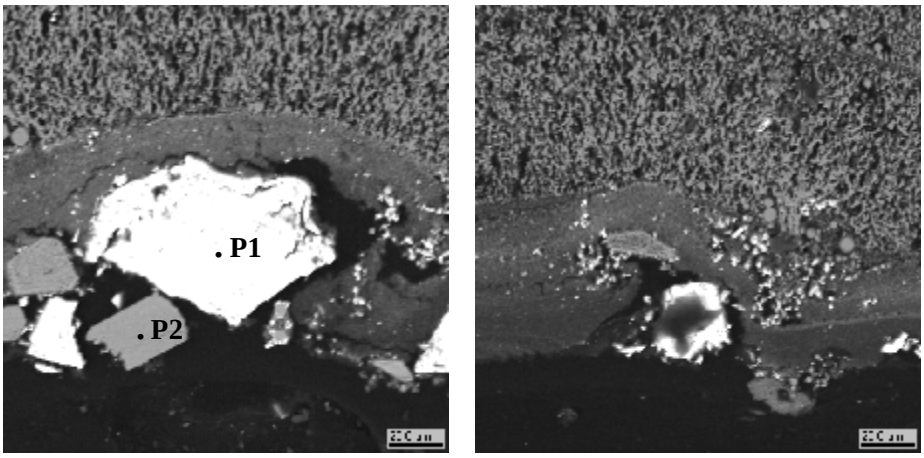

2 3

Fig. 2.5.3 – Micrograph of Region 2 and 3

Table 2.5.2 – Data on Region 2 EDX analysis

No.	%	U	Zr	Fe	~O
P1	mass %	87.66	-	0.35	11.99
	mol.%	32.77	-	0.57	66.67
	mol.%	98.30	-	1.70	
P2	mass %	-	74.00	-	25.98
	mol.%	-	33.32	-	66.68
	mol.%	-	100	-	

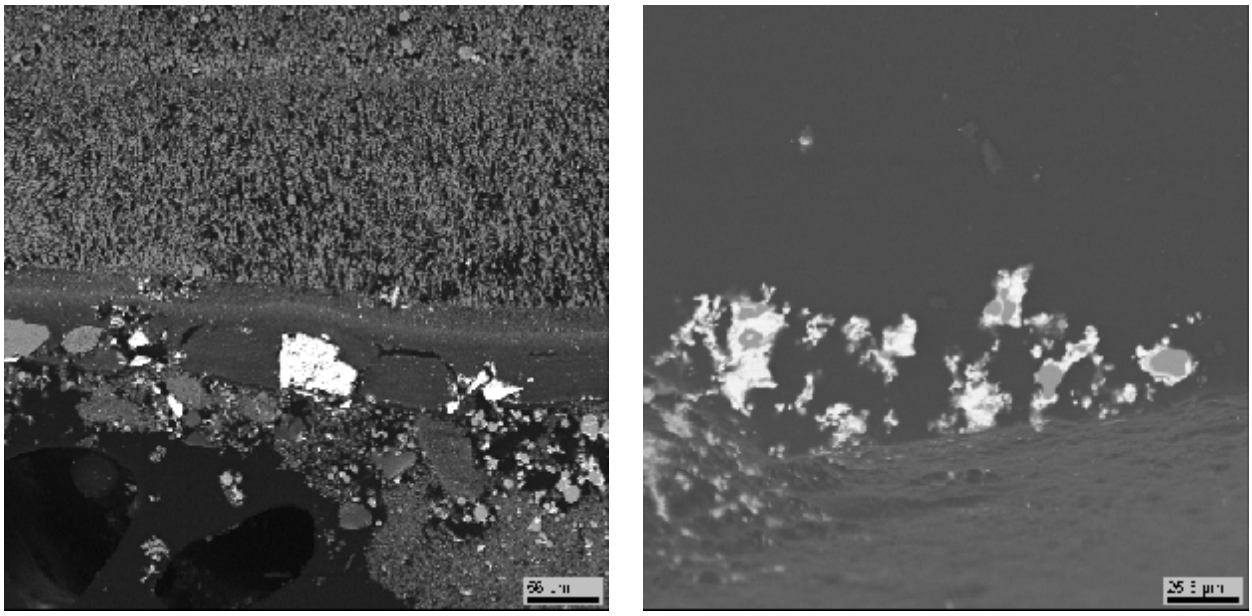

4 5

Fig. 2.5.4 – Micrographs of Regions 4 and 5

Fig. 2.5.5 – Template of the ingot oxidic part with regions marked for examination

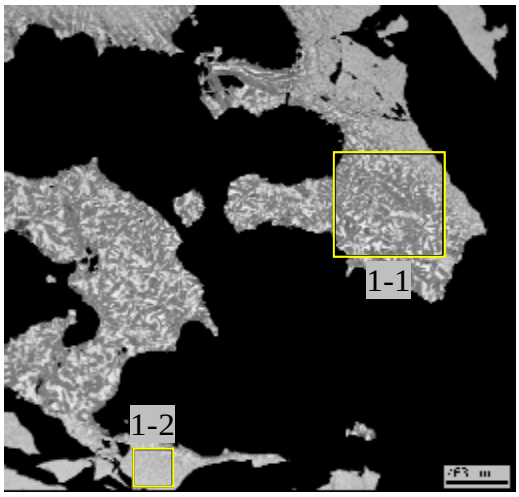

1

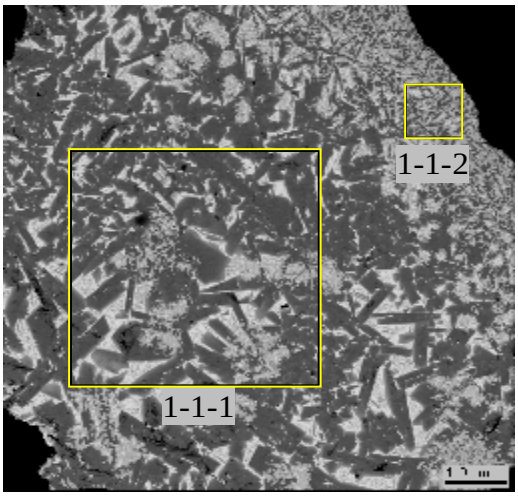

1-1

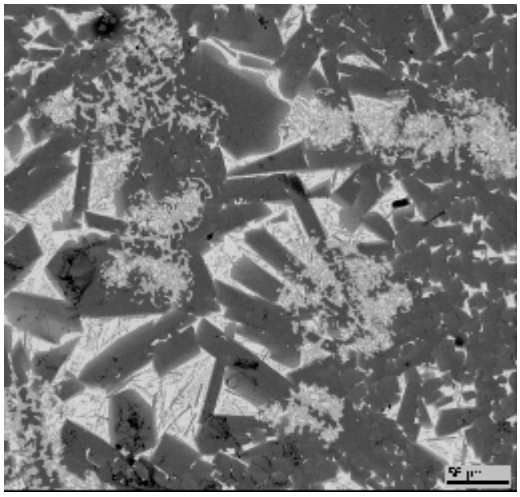

1-1-1 (SQ1)

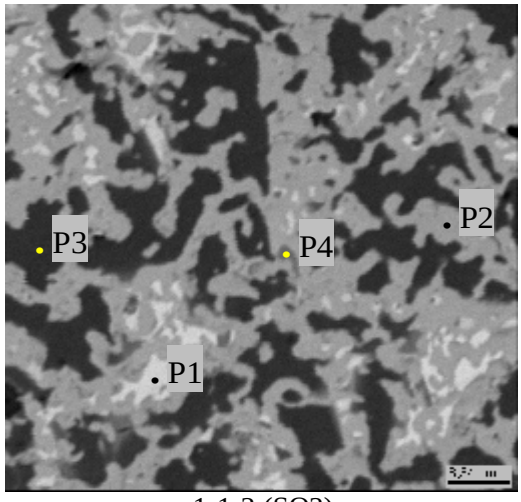

1-1-2 (SQ2)

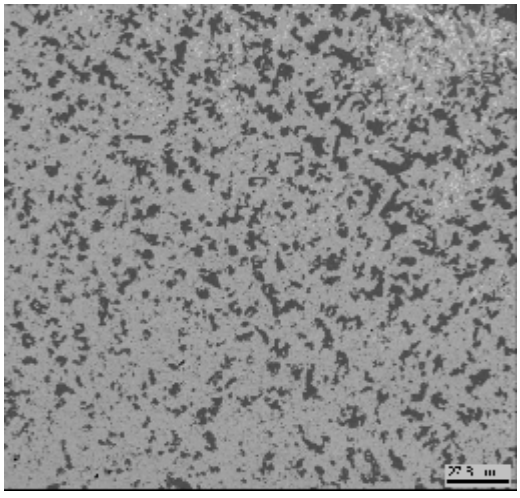

1-2 (SQ3)

Fig. 2.5.6 – Micrographs of Region 1

Table 2.5.3 – Data on Region 1 EDX analysis

No.		U	Zr	Fe	Cr	Ni	~O
SQ1	mass %	40.69	16.66	33.66	0.62	3.32	5.05
	mol.%	12.75	13.62	44.97	0.88	4.22	23.55
	mol.%	16.68	17.82	58.82	1.16	5.52	
SQ2	mass %	60.76	10.83	19.56	0.30	1.81	6.74
	mol.%	21.59	10.04	29.63	0.48	2.61	35.65
	mol.%	33.55	15.60	46.04	0.75	4.06	
SQ3	mass %	69.93	8.41	11.55	0.29	0.88	8.93
	mol.%	25.07	7.87	17.64	0.48	1.28	47.65
	mol.%	47.89	15.03	33.70	0.92	2.45	
P1	mass %	89.05	0.25	5.56	-	0.49	4.65
	mol.%	48.24	0.36	12.83	-	1.08	37.49
	mol.%	77.17	0.57	20.53	-	1.73	
P2	mass %	90.45	2.42	0.95	-	-	6.18
	mol.%	46.94	3.28	2.09	-	-	47.69
	mol.%	89.73	6.27	4	-	-	
P3	mass %	14.48	30.55	48.37	1.17	2.95	2.47
	mol.%	4.09	22.49	58.18	1.51	3.38	10.35
	mol.%	4.56	25.09	64.89	1.68	3.77	
P4	mass %	42.15	21.40	7.44	-	22.46	6.54
	mol.%	13.25	17.55	9.97	-	28.63	30.60
	mol.%	19.09	25.29	14.36	-	41.25	

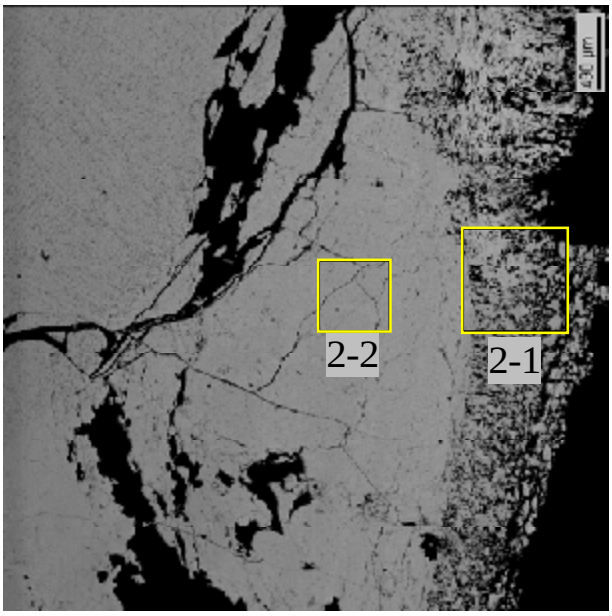

2

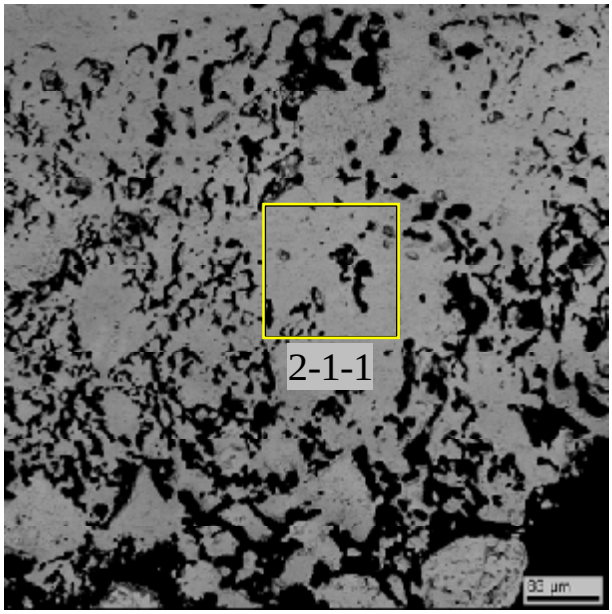

2-1

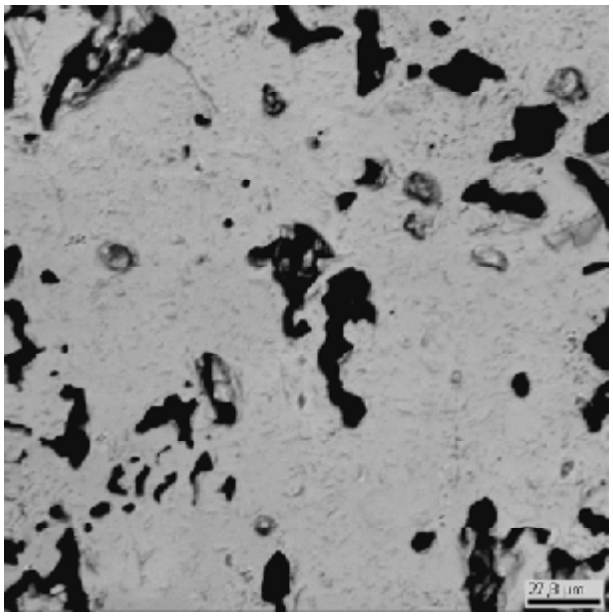

2-1-1

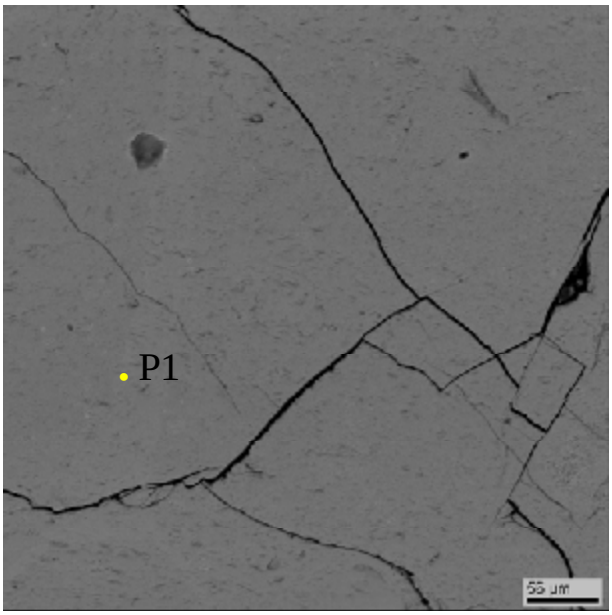

2-2 (SQ1)

Fig. 2.5.7 – Micrographs of Region 2

Table 2.5.4 – Data on Region 2 EDX analysis

No.		U	Zr	Fe	~O
SQ1	mass %	74.94	11.04	-	14.02
	mol.%	23.99	9.22	-	66.79
	mol.%	72.24	27.76	-	
P1	mass %	74.85	11.17	-	13.98
	mol.%	23.99	9.34	-	66.67
	mol.%	71.97	28.03	-	

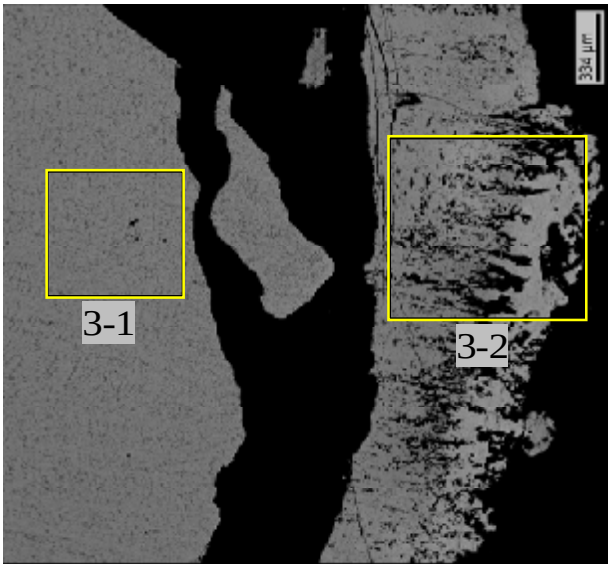

3

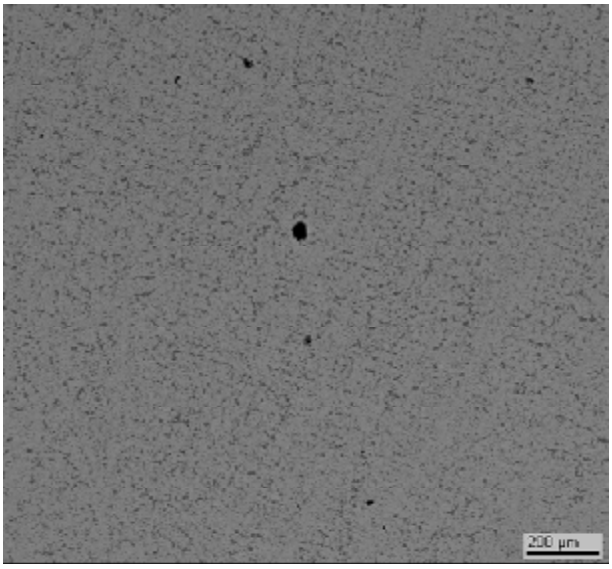

3-1 (SQ1)

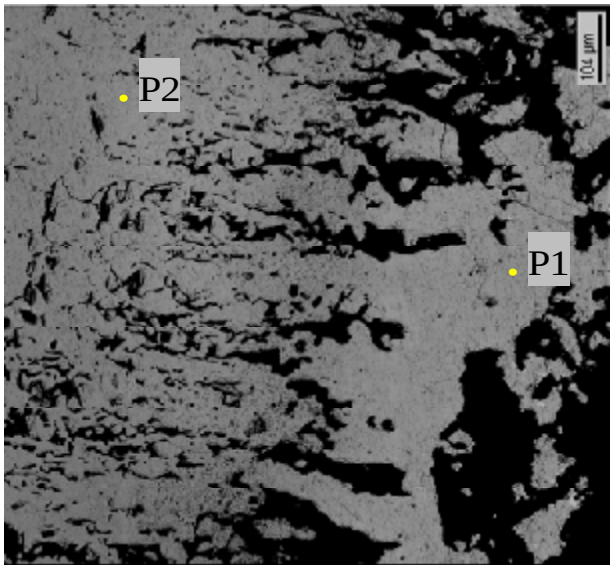

3-2

Fig. 2.5.8 – Micrographs of Region 3

Table 2.5.5 – Data on Region 3 EDX analysis

No.		U	Zr	Fe	~O
SQ1	mass %	68.74	19.09	-	12.17
	mol.%	22.95	16.63	-	60.43
	mol.%	57.98	42.02	-	
P1	mass %	85.11	3.24	-	11.65
	mol.%	31.90	3.17	-	64.93
	mol.%	90.96	9.04	-	
P2	mass %	87.18	2.26	-	10.56
	mol.%	34.85	2.35	-	62.79
	mol.%	93.67	6.33	-	

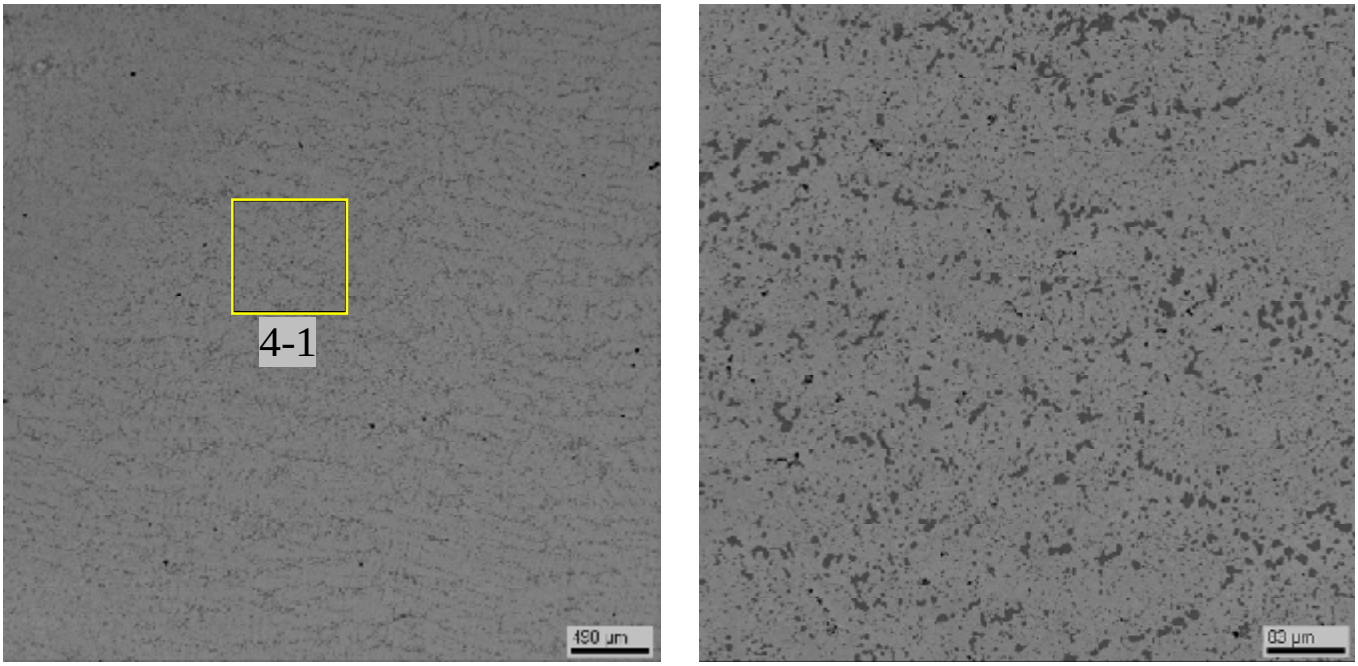

4 (SQ1) 4-1

Fig. 2.5.9 – Micrographs of Region 4

Table 2.5.6 – Data on Region 4 EDX analysis

No.		U	Zr	Fe	~O
SQ1	mass %	69.89	17.54	0.54	12.02
	mol.%	23.55	15.43	0.78	60.24
	mol.%	59.24	38.8	1.97	

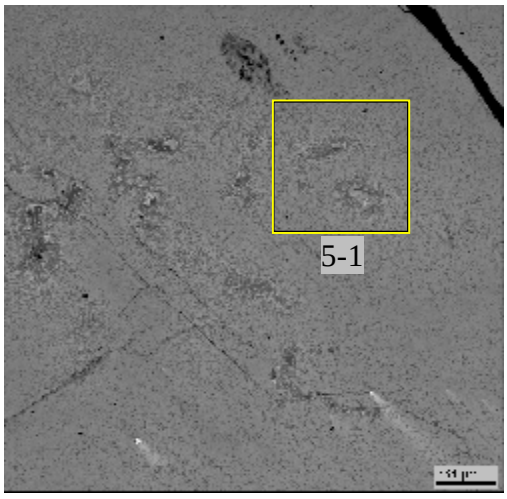

5

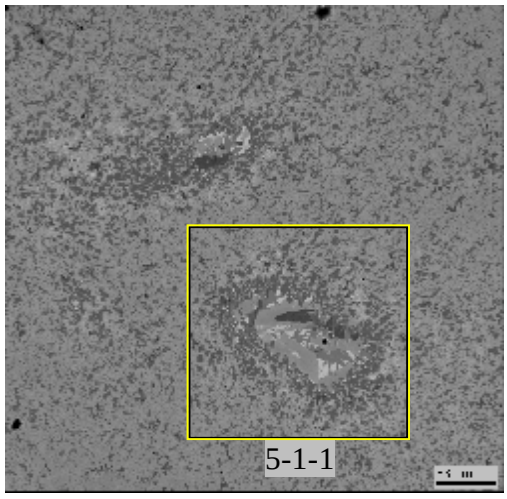

5-1

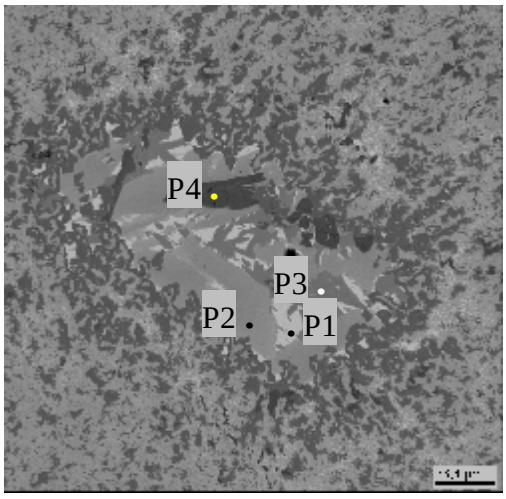

5-1-1

Fig. 2.5.10 – Micrographs of Region 5

Table 2.5.7 – Data on Region 5 EDX analysis

No.		U	Zr	Fe	Cr	Ni	Mn	~O
P1	mass %	93.37	-	4.30	-	0.41	-	1.92
	mol.%	65.79	-	12.91	-	1.16	-	20.14
	mol.%	82.38	-	16.16	-	1.46	-	
P2	mass %	54.88	22.28	15.62	-	2.70	-	4.52
	mol.%	21.29	22.56	25.83	-	4.25	-	26.06
	mol.%	28.80	30.51	34.94	-	5.75	-	
P3	mass %	43.16	21.71	30.47	0.33	0.66	-	3.67
	mol.%	14.96	19.63	45.02	0.53	0.93	-	18.93
	mol.%	18.46	24.22	55.53	0.65	1.14	-	
P4	mass %	5.36	78.51	4.46	-	1.31	-	10.36
	mol.%	1.38	52.71	4.89	-	1.37	-	39.64
	mol.%	2.29	87.34	8.11	-	2.27	-	

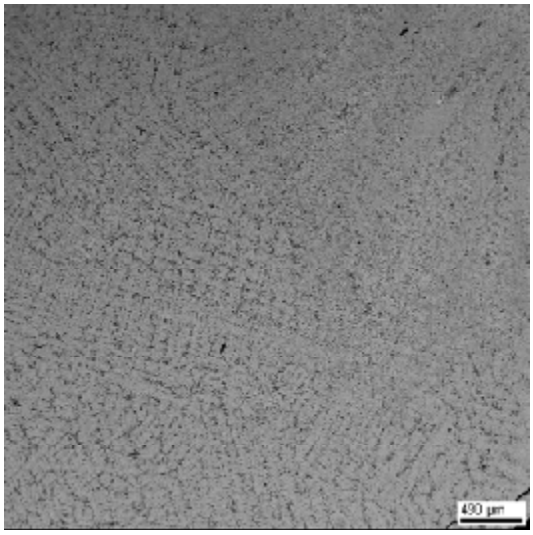

6 (SQ1)

Fig. 2.5.11 – Micrograph of Region 6

Table 2.5.8 – Data on Region 6 EDX analysis

No.		U	Zr	Fe	~O
SQ1	mass %	69.33	17.73	1.27	11.66
	mol.%	23.54	15.71	1.84	58.9
	mol.%	57.29	38.23	4.48	

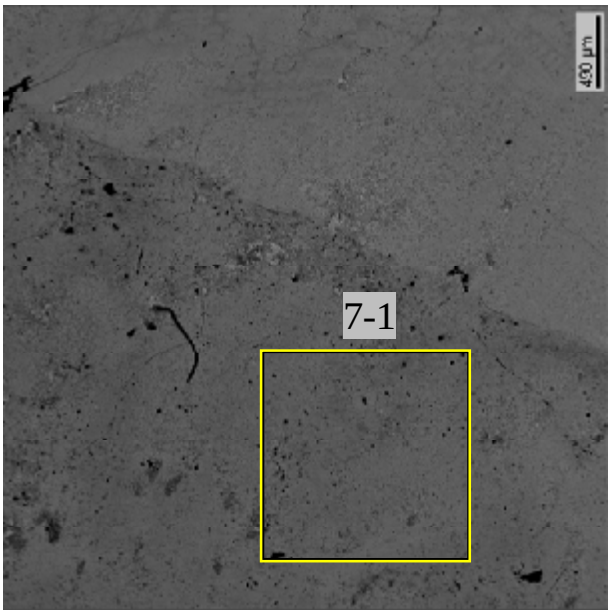

7

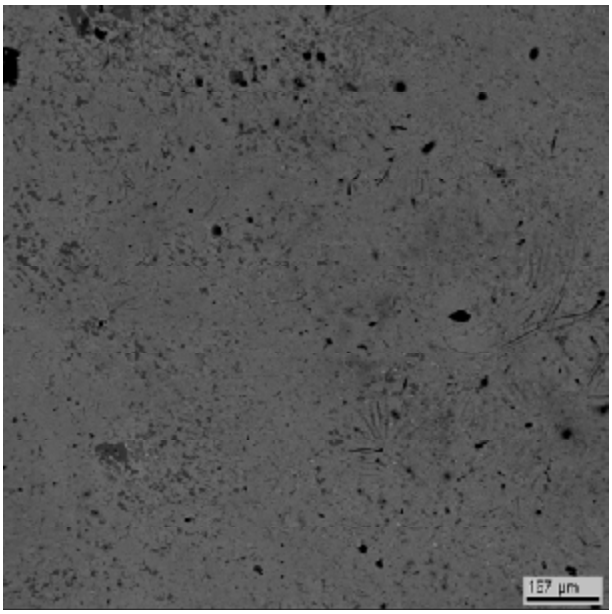

7-1 (SQ1)

Fig. 2.5.12 – Micrographs of Region 7

Table 2.5.9 – Data on Region 7 EDX analysis

No.		U	Zr	Fe	~O
SQ1	mass %	67.99	15.46	6.21	10.33
	mol.%	23.56	13.98	9.17	53.28
	mol.%	50.44	29.93	19.64	

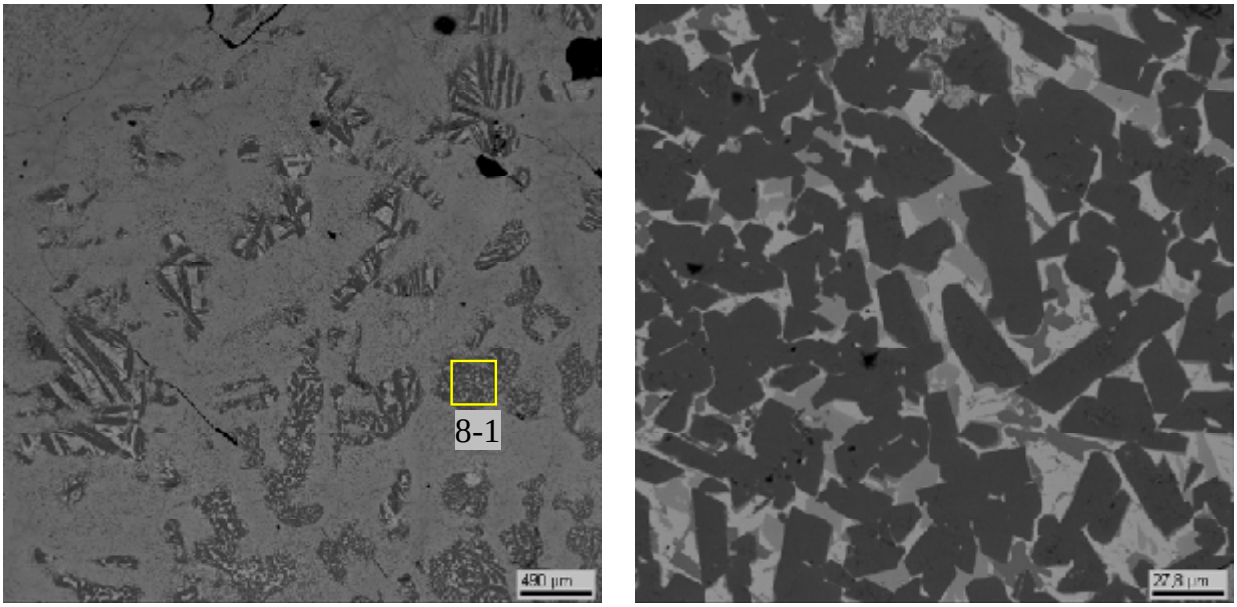

8 8-1 (SQ1)

Fig. 2.5.13 – Micrographs of Region 8

Table 2.5.10 – Data on Region 8 EDX analysis

No.		U	Zr	Fe	Cr	Ni	O
SQ1	mass %	35.21	22.43	36.02	0.71	3.31	2.32
	mol.%	11.80	19.61	51.45	1.09	4.50	11.55
	mol.%	13.34	22.17	58.17	1.23	5.09	

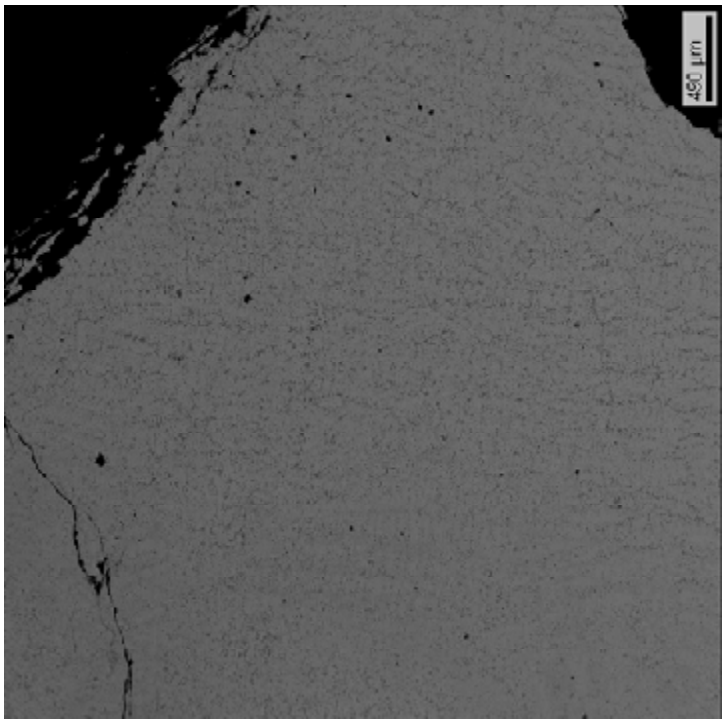

9

Fig. 2.5.14 – Micrograph of Region 9

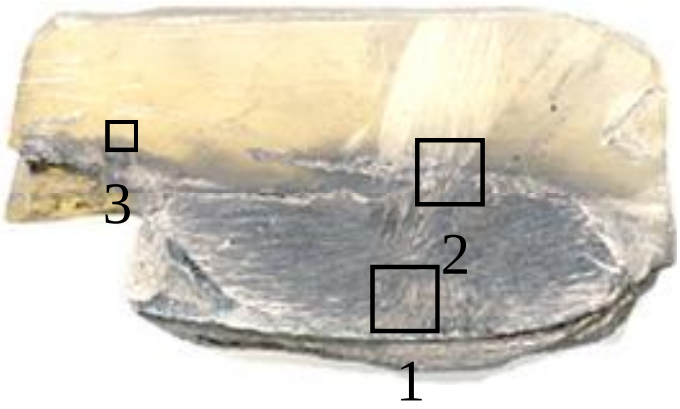

Fig. 2.5.15 – Template of the interaction zone upper layer with regions marked for examination

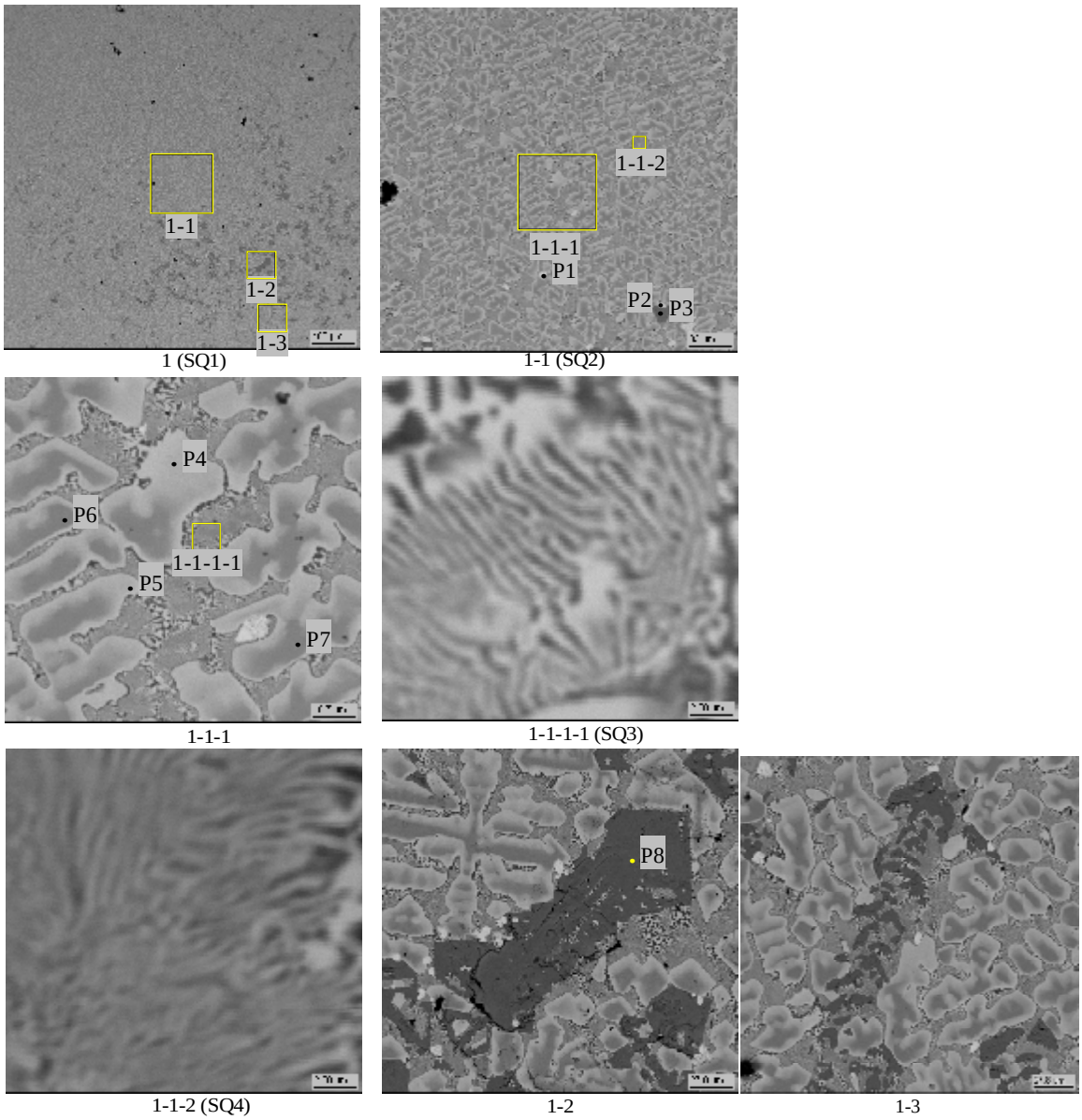

Fig. 2.5.16 – Micrographs of Region 1

Table 2.5.11 – Data on Region 1 EDX analysis

No.		U	Zr	Fe	Cr	Ni	Mn	~O
SQ1	mass %	38.24	9.19	46.79	1.23	1.17	0.18	3.19
	mol.%	11.94	7.49	62.26	1.76	1.48	0.25	14.83
	mol.%	14.01	8.79	73.09	2.07	1.74	0.29	
SQ2	mass %	41.06	7.28	49.16	1.36	0.92	0.23	-
	mol.%	14.64	6.77	74.70	2.22	1.33	0.35	-
SQ3	mass %	40.09	1.54	54.81	2.06	1.11	0.38	-
	mol.%	13.67	1.37	79.65	3.21	1.54	0.56	-
SQ4	mass %	39.10	1.35	55.99	2.24	1.02	0.31	-
	mol.%	13.17	1.18	80.36	3.46	1.39	0.45	-
P1	mass %	78.70	9.54	0.45	-	-	-	11.31
	mol.%	28.74	9.09	0.69	-	-	-	61.47
	mol.%	74.59	23.60	1.80	-	-	-	
P2	mass %	56.40	33.55	0.40	-	-	-	9.64
	mol.%	19.51	30.28	0.60	-	-	-	49.62
	mol.%	38.72	60.10	1.18	-	-	-	
P3	mass %	1.58	72.35	0.46	-	-	-	25.59
	mol.%	0.28	32.94	0.35	-	-	-	66.43
	mol.%	0.81	98.15	1.04	-	-	-	
P4	mass %	56.09	3.30	39.05	0.48	1.08	-	-
	mol.%	23.60	3.62	70.01	0.93	1.84	-	-
P5	mass %	51.22	5.11	41.90	0.50	1.14	0.13	-
	mol.%	20.44	5.32	71.25	0.92	1.84	0.23	-
P6	mass %	23.48	19.87	54.34	0.90	1.08	0.33	-
	mol.%	7.41	16.37	73.09	1.30	1.38	0.45	-
P7	mass %	23.74	19.82	54.11	0.89	1.07	0.37	-
	mol.%	7.51	16.36	72.97	1.29	1.37	0.50	-
P8	mass %	-	73.12	1.23	-	-	-	25.65
	mol.%	-	33.03	0.91	-	-	-	66.06
	mol.%	-	97.34	2.66	-	-	-	

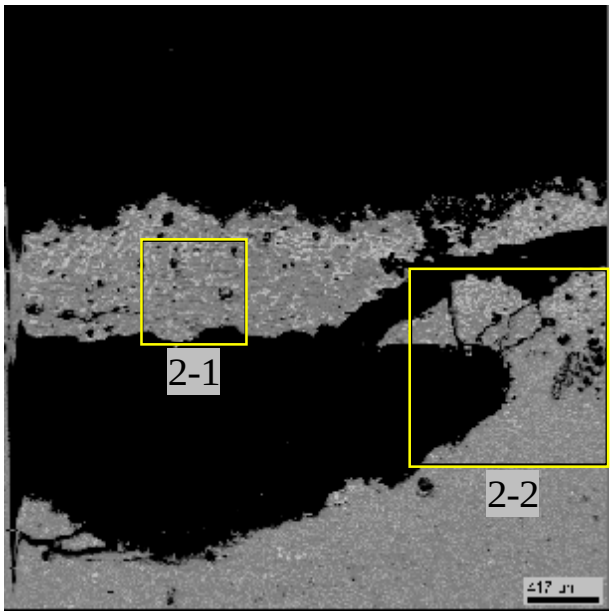

2

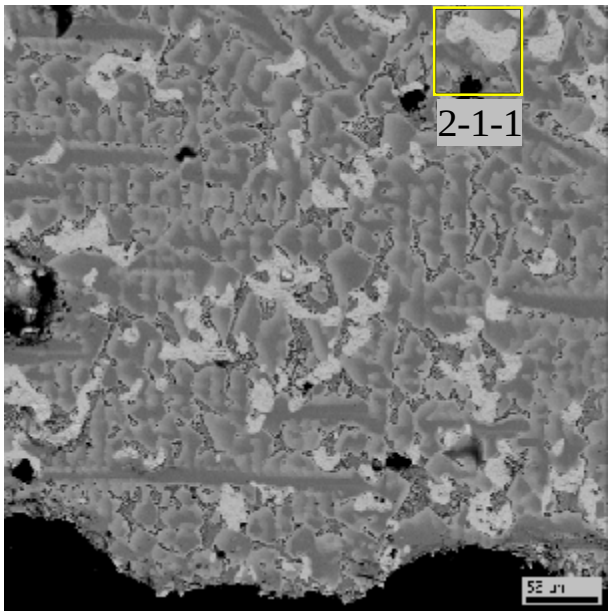

2-1

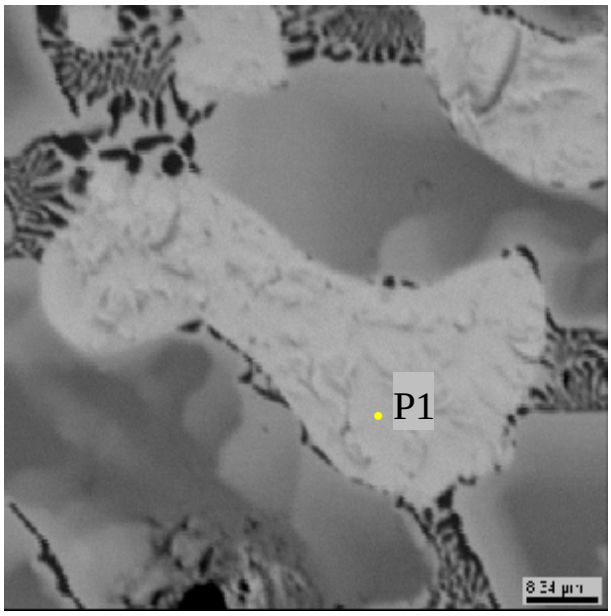

2-1-1

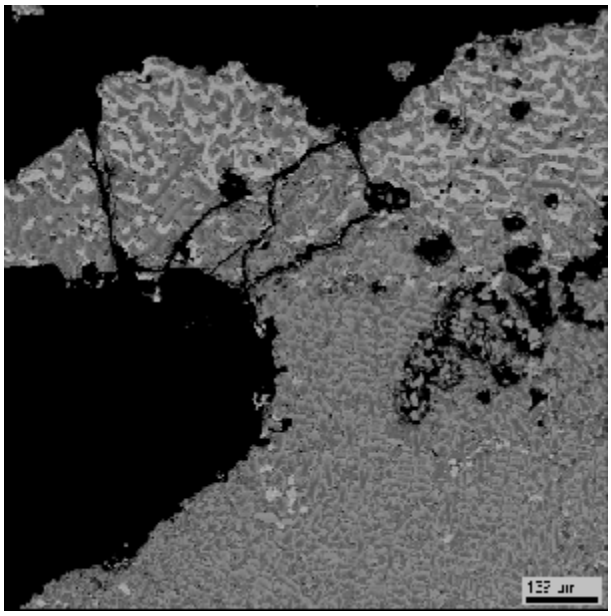

2-2

Fig. 2.5.17 – Micrographs of Region 2

Table 2.5.12 – Data on Region 2 EDX analysis

No.		U	Zr	Fe	~O
P1	mass %	86.66	1.22	0.33	11.79
	mol.%	32.51	1.19	0.52	65.78
	mol.%	94.98	3.49	1.53	

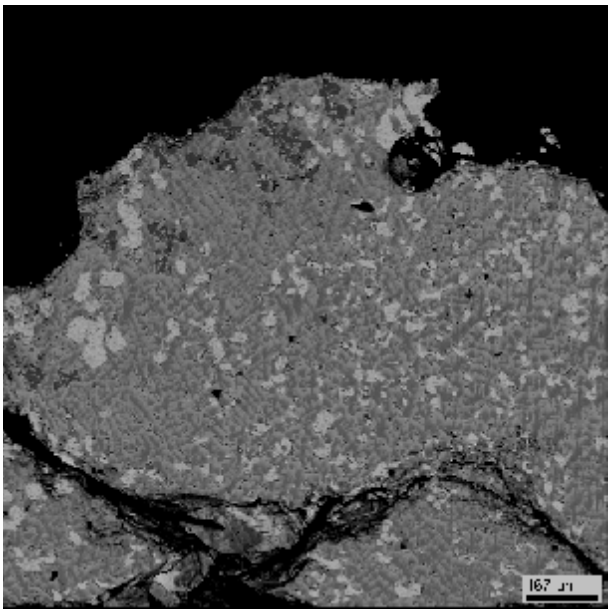

3

Fig. 2.5.18 – Micrograph of Region 3

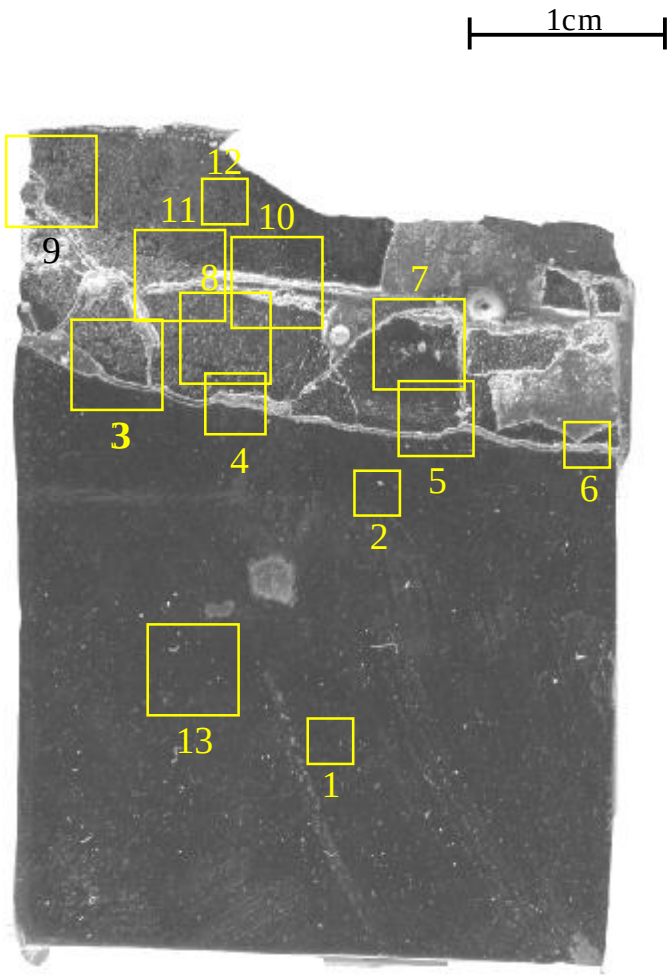

Fig. 2.5.19 – Template of the specimen longitudinal section, interaction zone included, with regions marked for examination

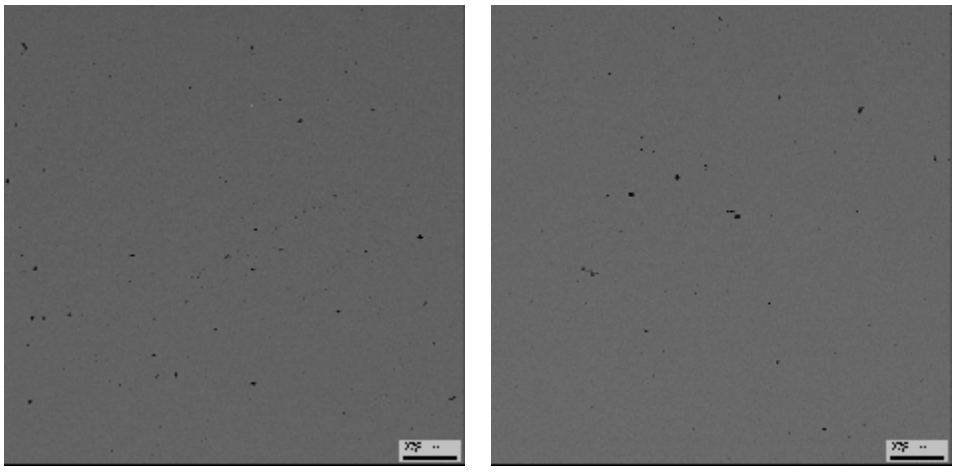

1 (SQ1) 2 (SQ2)

Fig. 2.5.20 – Micrographs of Regions 1 and 2

Table 2.5.13 – Data on Regions 1 and 2 EDX analysis

No.		Fe	Cr	Ni	Mn
SQ1	mass %	96.08	2.26	1.12	0.53
	mol.%	95.96	2.43	1.07	0.54
SQ2	mass %	96.32	2.16	0.98	0.54
	мол.%	96.21	2.31	0.93	0.55

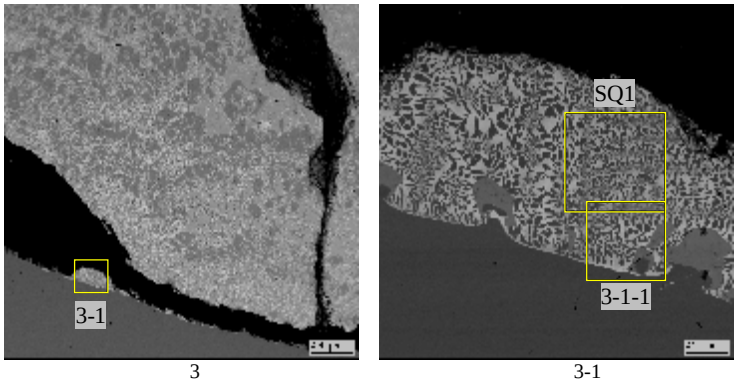

3 3-1

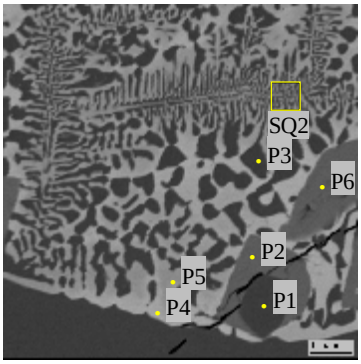

3-1-1

Fig. 2.5.21 – Micrographs of Region 3

Table 2.5.14 – Data on Region 3 EDX analysis

No.		U	Zr	Fe	Cr	Ni	Mn	~O
SQ1	mass %	28.49	2.82	64.85	2.21	1.12	0.40	0.12
	mol.%	8.62	2.22	83.64	3.06	1.38	0.52	0.56
	mol.%	8.67	2.24	84.11	3.08	1.38	0.52	
SQ2	mass %	24.38	4.22	66.65	2.25	0.68	0.48	1.33
	mol.%	6.88	3.11	80.15	2.91	0.78	0.59	5.59
	mol.%	7.29	3.29	84.89	3.08	0.83	0.63	
P1	mass %	-	-	96.37	2.08	1.02	0.53	-
	mol.%	-	-	96.26	2.23	0.97	0.54	-
P2	mass %	8.97	17.62	64.98	1.30	0.88	0.29	5.96
	mol.%	2.08	10.66	64.22	1.38	0.82	0.29	20.54
	mol.%	2.62	13.42	80.82	1.74	1.04	0.36	
P3	mass %	0.58	-	94.36	3.86	0.72	0.43	0.05
	mol.%	0.14	-	94.42	4.14	0.69	0.44	0.17
	mol.%	0.14	-	94.59	4.15	0.69	0.44	
P4	mass %	51.05	4.4	41.95	0.36	1.36	-	0.89
	mol.%	19.5	4.39	68.31	0.62	2.1	-	5.07
	mol.%	20.55	4.62	71.96	0.66	2.22	-	
P5	mass %	44.40	7.08	45.79	0.59	1.12	-	1.02
	mol.%	15.84	6.59	69.61	0.96	1.62	-	5.39
	mol.%	16.74	6.96	73.57	1.01	1.71	-	
P6	mass %	8.28	17.92	64.67	1.40	1.12	-	6.61
	mol.%	1.88	10.63	62.66	1.45	1.03	-	22.35
	mol.%	2.42	13.68	80.69	1.87	1.33	-	

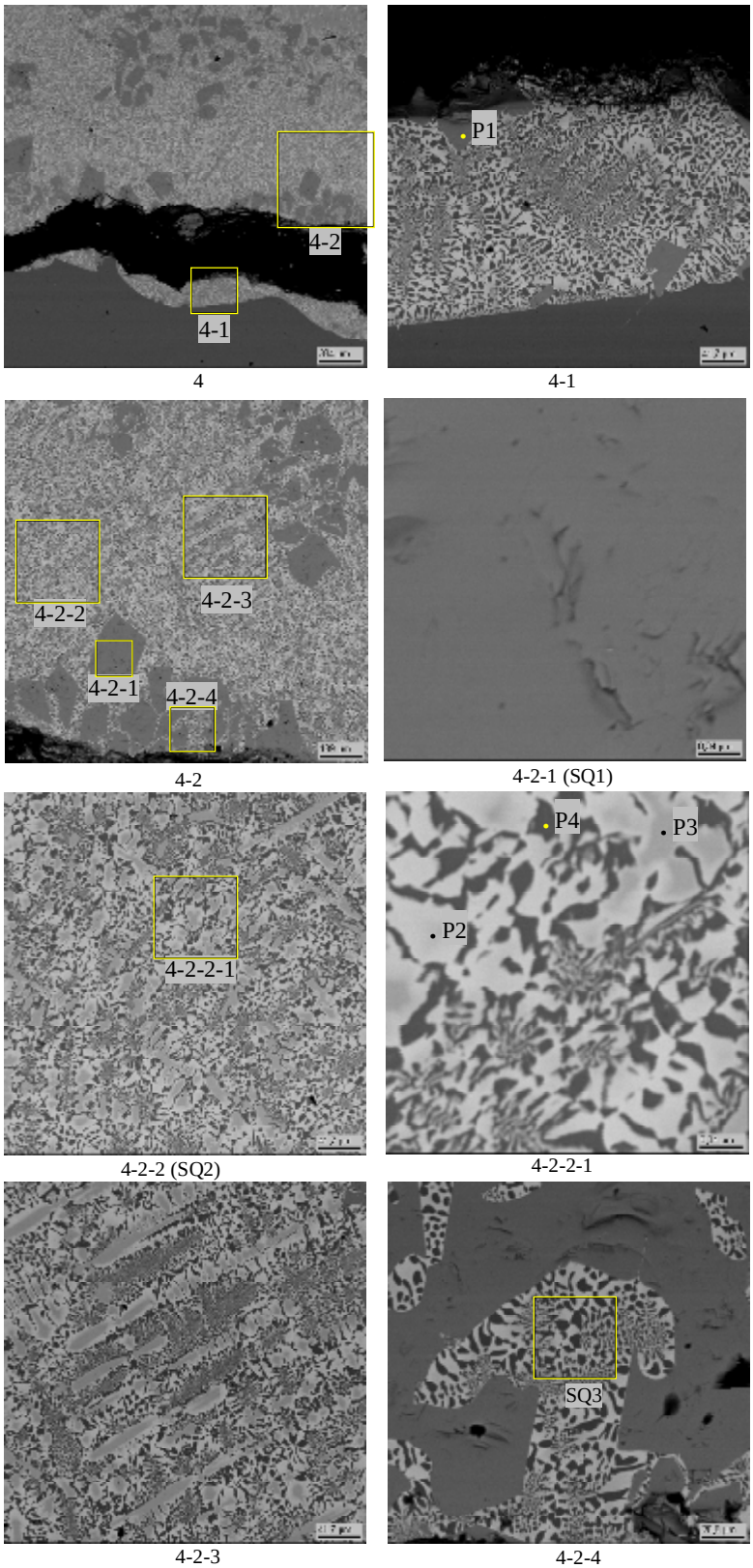

Fig. 2.5.22 – Micrographs of Region 4

Table 2.5.15 – Data on Region 4 EDX analysis

No.		U	Zr	Fe	Cr	Ni	Mn	~O
SQ1	mass %	7.17	17.79	64.97	1.40	0.99	0.32	7.36
	mol.%	1.59	10.27	61.30	1.42	0.89	0.31	24.22
	mol.%	2.09	13.56	80.89	1.87	1.18	0.41	
SQ2	mass %	35.10	2.90	58.99	1.61	1.08	0.33	-
	mol.%	11.42	2.46	81.83	2.40	1.42	0.46	-
SQ3	mass %	29.42	2.84	63.75	2.12	1.01	0.34	0.51
	mol.%	8.88	2.23	81.98	2.93	1.24	0.45	2.30
	mol.%	9.08	2.28	83.91	3.00	1.27	0.46	
P1	mass %	8.64	19.02	65.33	1.43	1.05	0.33	4.20
	mol.%	2.10	12.07	67.68	1.59	1.03	0.35	15.18
	mol.%	2.48	14.23	79.79	1.88	1.22	0.41	
P2	mass %	56.62	2.55	39.34	0.31	1.18	-	-
	mol.%	23.87	2.81	70.70	0.60	2.02	-	-
P3	mass %	36.22	10.48	49.14	0.63	1.34	0.31	1.87
	mol.%	11.66	8.80	67.45	0.93	1.75	0.44	8.97
	mol.%	12.81	9.67	74.09	1.02	1.92	0.48	
P4	mass %	0.75	-	94.5	3.55	0.57	0.54	0.09
	mol.%	0.18	-	94.6	3.82	0.54	0.55	0.32
	mol.%	0.18	-	94.9	3.83	0.54	0.55	

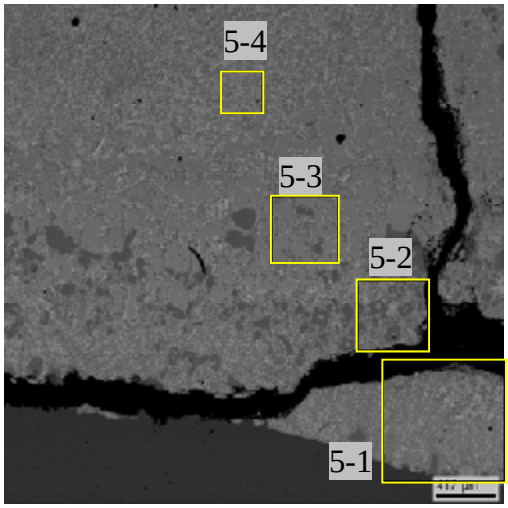

5

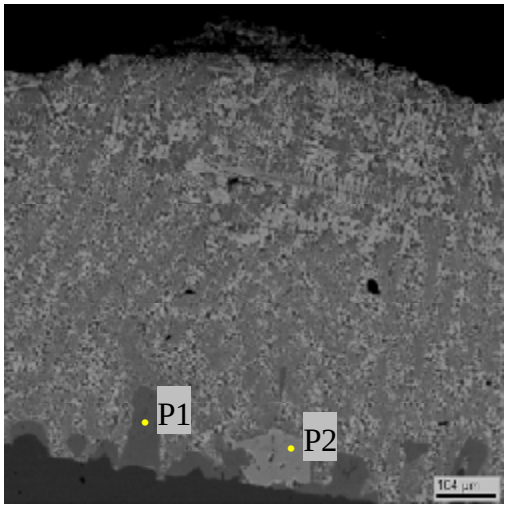

5-1

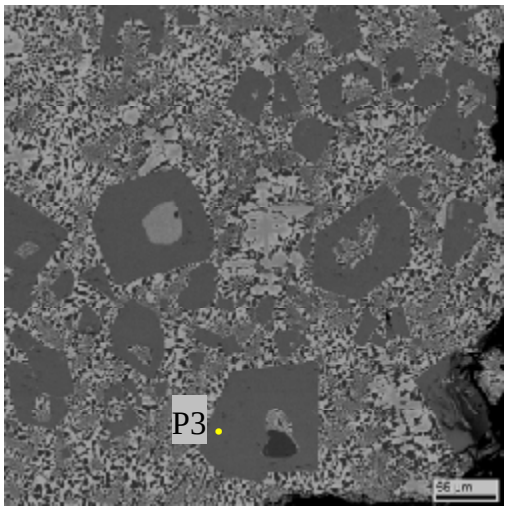

5-2

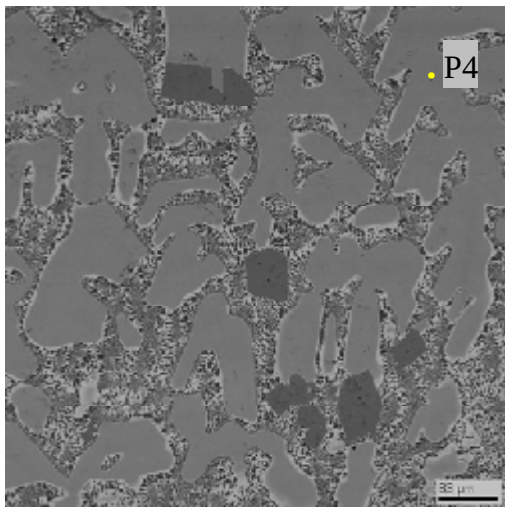

5-3

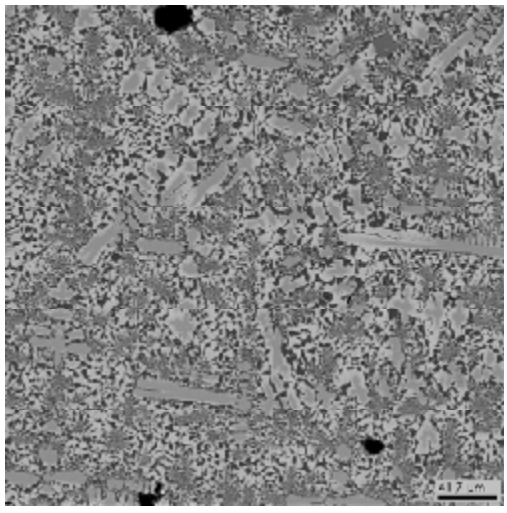

5-4 (SQ1)

Fig. 2.5.23 – Micrographs of Region 5

Table 2.5.16 – Data on Region 5 EDX analysis

No.		U	Zr	Fe	Cr	Ni	Mn	~O
SQ1	mass %	35.50	2.70	58.54	1.77	1.14	0.34	-
	mol.%	11.59	2.30	81.46	2.65	1.52	0.48	-
P1	mass %	8.14	17.56	63.94	1.49	1.11	0.22	7.53
	mol.%	1.80	10.17	60.45	1.51	1.00	0.21	24.85
	mol.%	2.40	13.53	80.45	2.01	1.33	0.28	
P2	mass %	35.34	9.99	47.63	0.58	0.93	-	5.52
	mol.%	10.01	7.38	57.51	0.76	1.07	-	23.26
	mol.%	13.05	9.62	74.95	0.99	1.39	-	
P3	mass %	8.73	16.95	63.71	1.40	0.96	0.28	7.97
	mol.%	1.92	9.72	59.72	1.41	0.86	0.27	26.09
	mol.%	2.60	13.16	80.81	1.91	1.16	0.37	
P4	mass %	27.79	13.42	51.42	0.70	1.09	0.26	5.31
	mol.%	7.51	9.47	59.27	0.87	1.20	0.31	21.37
	mol.%	9.56	12.05	75.37	1.11	1.53	0.39	

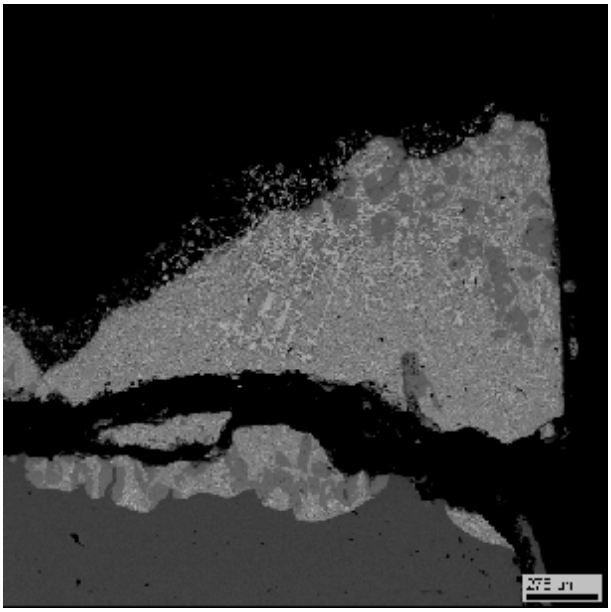

6

Fig. 2.5.24 – Micrograph of Region 6

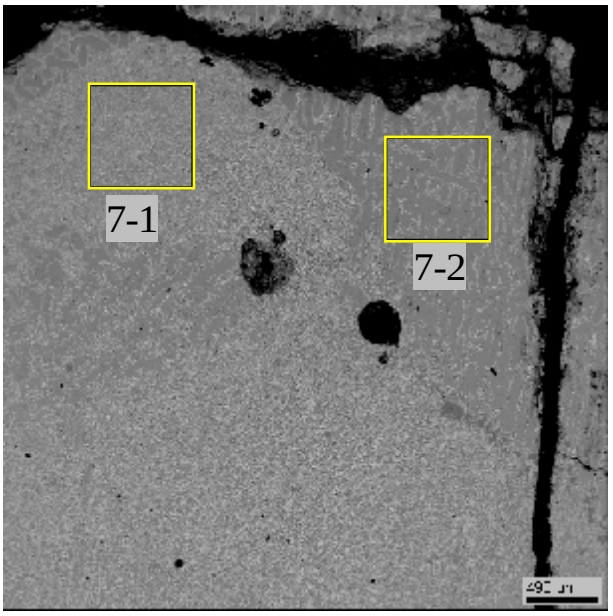

7

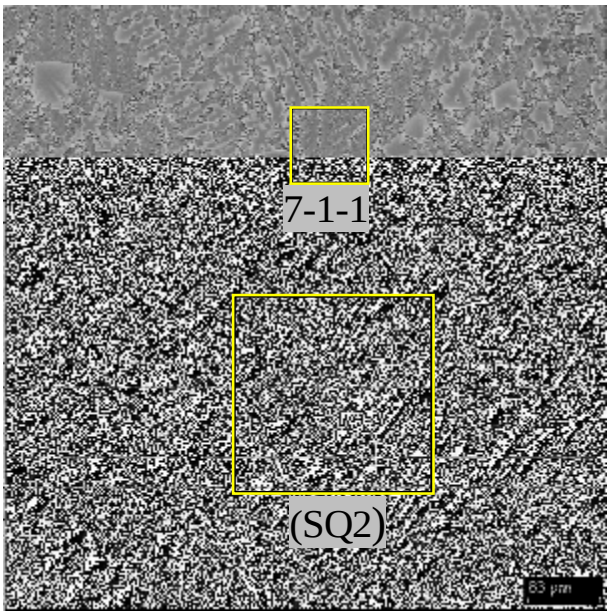

7-1 (SQ1)

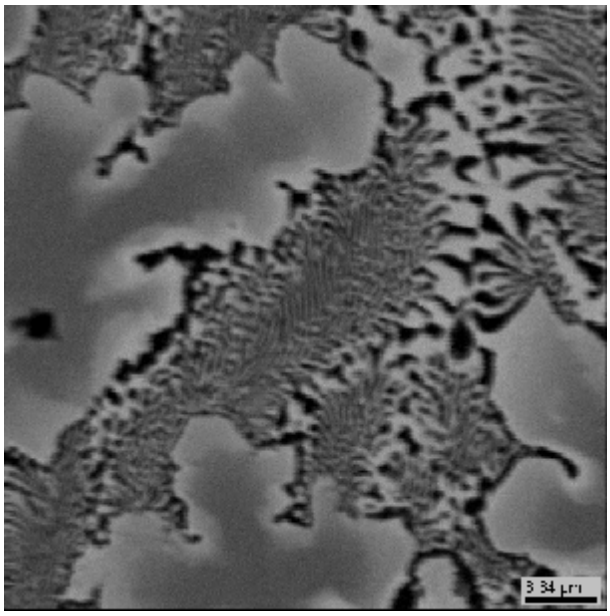

7-1-1 (SQ3)

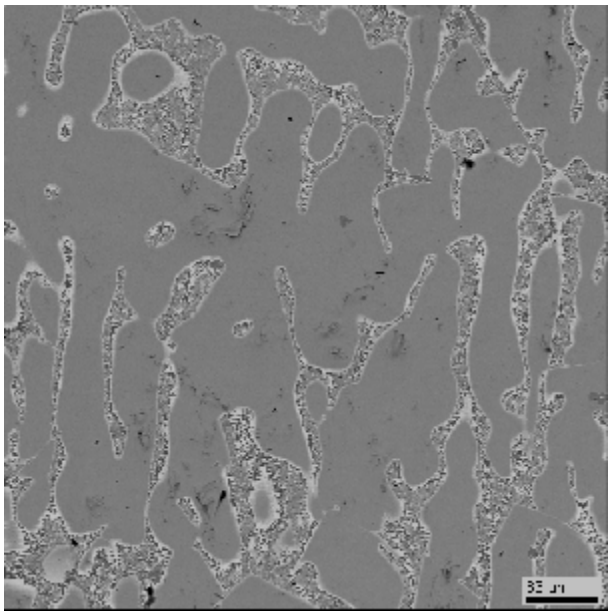

7-2 (SQ4)

Fig. 2.5.25 – Micrographs of Region 7

Table 2.5.17 – Data on Region 7 EDX analysis

No.		U	Zr	Fe	Cr	Ni	Mn	~O
SQ1	mass %	35.58	4.90	56.32	1.67	1.15	0.38	-
	mol.%	11.77	4.23	79.40	2.53	1.54	0.54	-
SQ2	mass %	34.91	6.23	55.03	1.62	1.08	-	1.13
	mol.%	11.11	5.17	74.64	2.36	1.40	-	5.33
	mol.%	11.73	5.46	78.84	2.49	1.48	-	
SQ3	mass %	34.78	5.55	55.15	1.40	1.16	0.23	1.72
	mol.%	10.80	4.50	73.00	1.99	1.46	0.31	7.93
	mol.%	11.73	4.88	79.29	2.16	1.59	0.34	
SQ4	mass %	25.86	13.61	54.32	0.92	0.94	-	4.35
	mol.%	7.07	9.71	63.32	1.15	1.05	-	17.70
	mol.%	8.59	11.80	76.93	1.40	1.27	-	

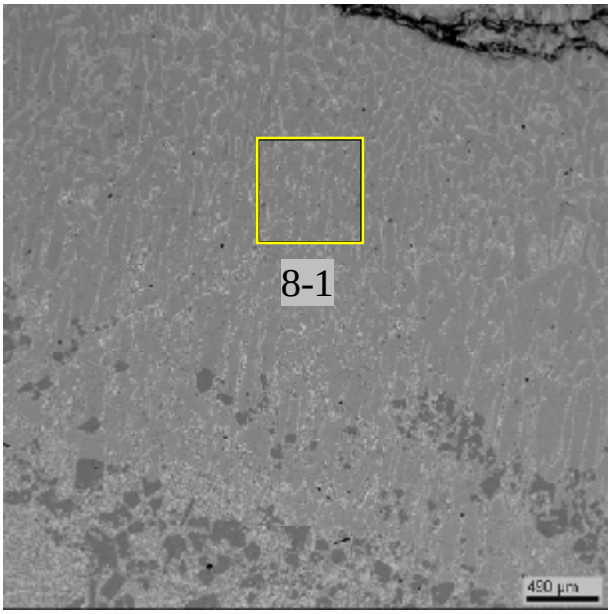

8

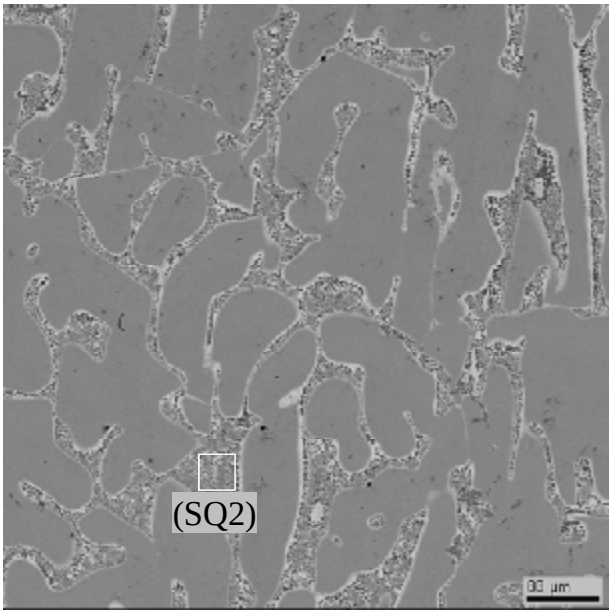

8-1 (SQ1)

Fig. 2.5.26 – Micrographs of Region 8

Table 2.5.18 – Data on Region 8 EDX analysis

No.		U	Zr	Fe	Cr	Ni	Mn	~O
SQ1	mass %	26.87	13.36	55.27	0.97	1.19	-	2.34
	mol.%	7.87	10.22	69.02	1.30	1.41	-	10.18
	mol.%	8.76	11.37	76.84	1.44	1.57	-	
SQ2	mass %	34.18	1.51	60.08	2.23	0.89	0.35	0.76
	mol.%	10.66	1.23	79.83	3.18	1.13	0.47	3.51
	mol.%	11.04	1.28	82.73	3.30	1.17	0.49	

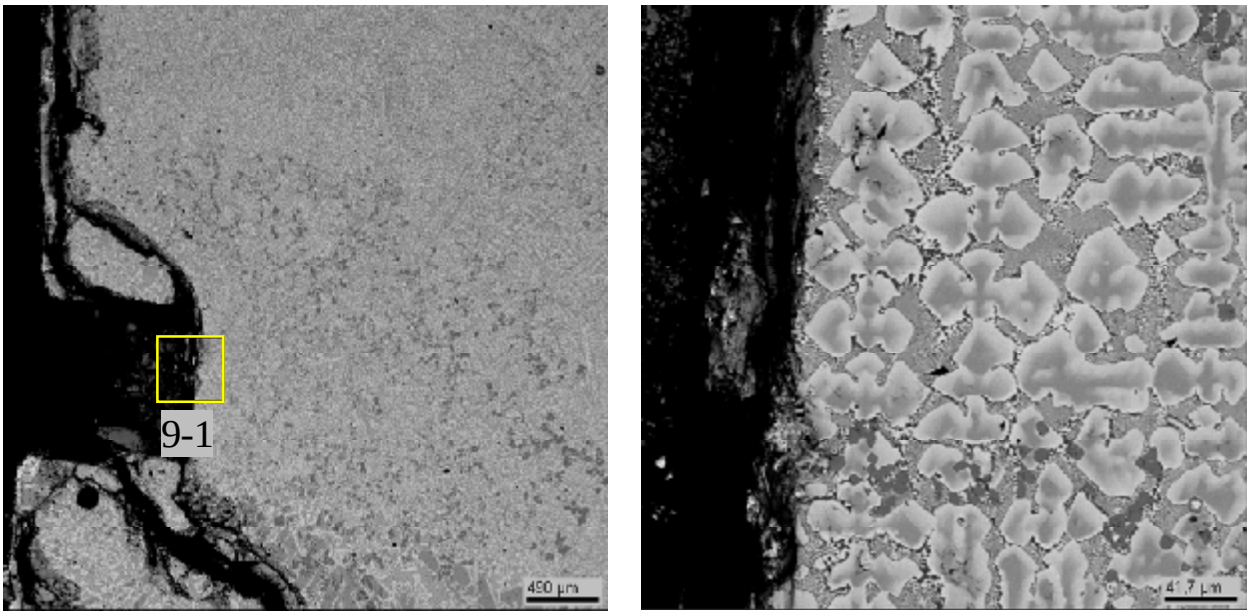

9 9-1

Fig. 2.5.27 – Micrographs of Region 9

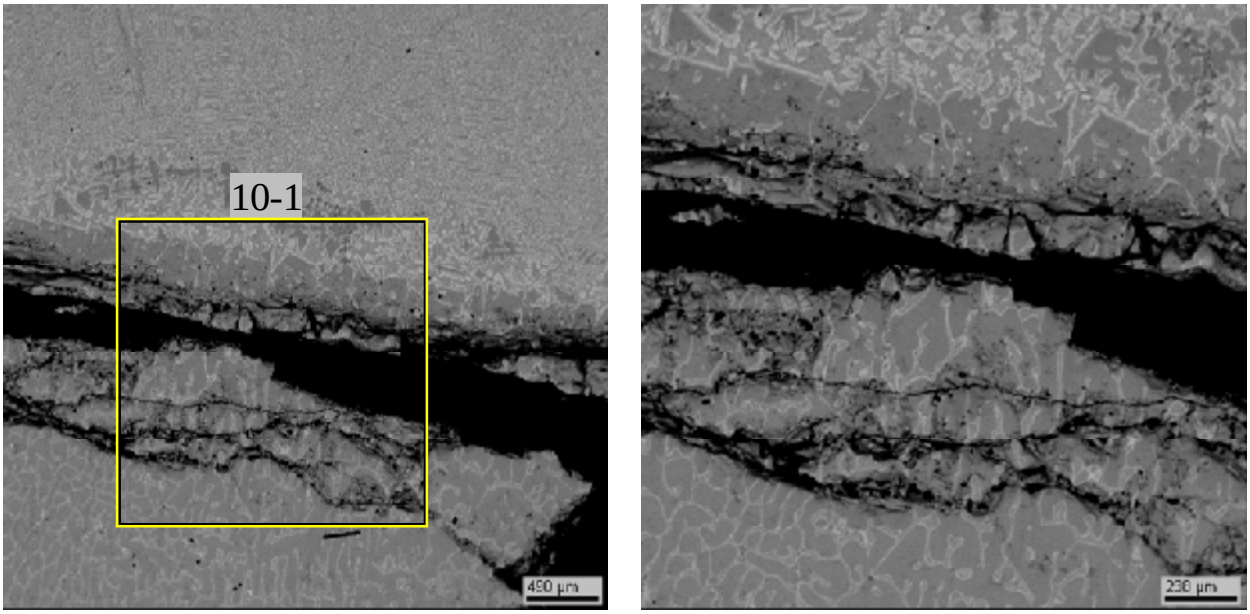

10 10-1

Fig. 2.5.28 – Micrographs of Region 10

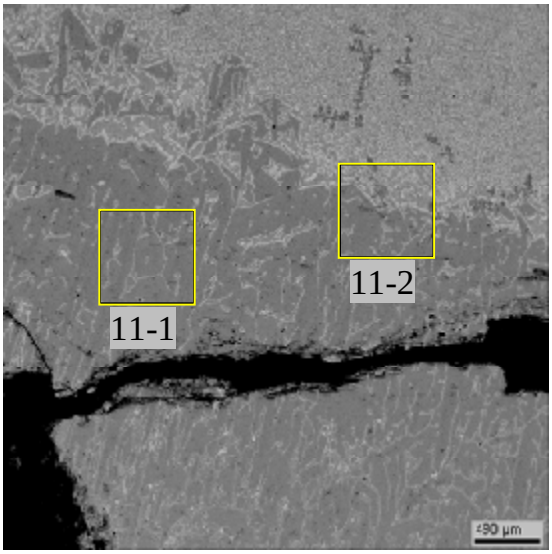

11

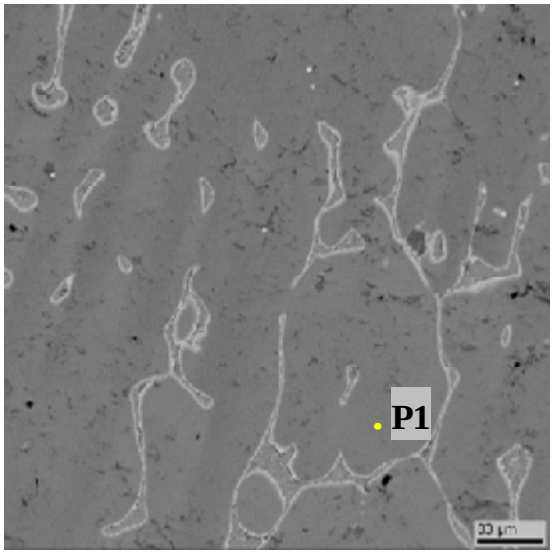

11-1 (SQ1)

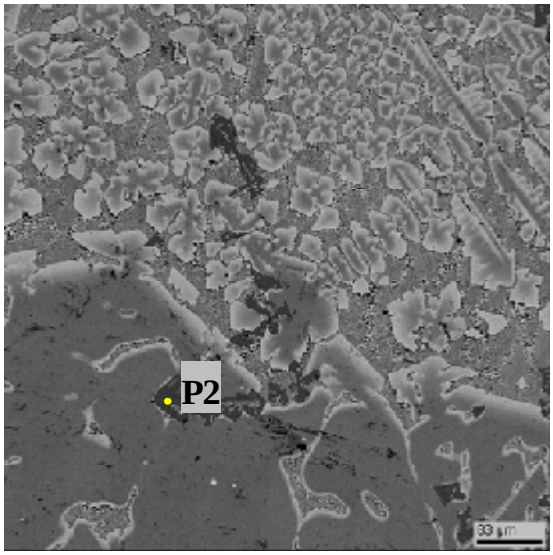

11-2

Fig. 2.5.29 – Micrographs of Region 11

Table. 2.5.19 – Data on Region 11 EDX analysis

No.		U	Zr	Fe	Cr	Ni	Mn	~O
SQ1	mass %	22.03	17.49	53.53	1.07	0.85	0.26	4.76
	mol.%	5.86	12.13	60.65	1.30	0.91	0.30	18.84
	mol.%	7.21	14.95	74.73	1.61	1.13	0.37	
P1	mass %	19.32	19.63	54.02	0.93	1.18	0.28	4.64
	mol.%	5.08	13.48	60.58	1.12	1.26	0.32	18.17
	mol.%	6.21	16.47	74.03	1.36	1.54	0.39	
P2	mass %	3.85	66.89	5.45	-	-	-	23.81
	mol.%	0.69	31.40	4.18	-	-	-	63.73
	mol.%	1.91	86.57	11.52	-	-	-	

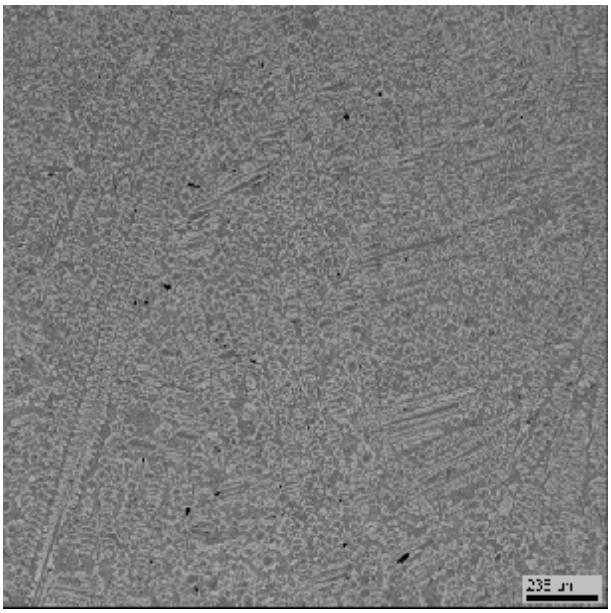

12 (SQ1)

Fig. 2.5.30 – Micrograph of Region 12

Table 2.5.20 – Data on Region 12 EDX analysis

No.		U	Zr	Fe	Cr	Ni	Mn	~O
SQ1	mass %	39.21	5.91	49.72	1.43	1.04	0.26	2.43
	mol.%	12.47	4.90	67.38	2.08	1.33	0.36	11.47
	mol.%	14.08	5.54	76.11	2.35	1.51	0.41	

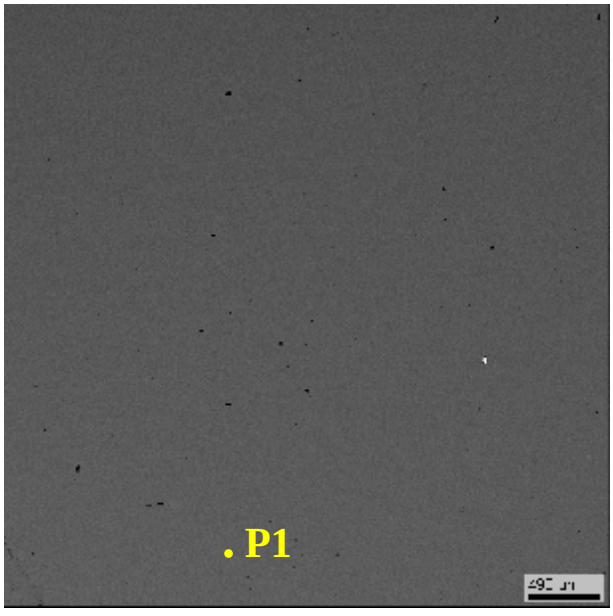

14 (SQ1)

Fig. 2.5.31 – Micrograph of Region 13

Table 2.5.21 – Data on Region 13 EDX analysis

No.		Fe	Cr	Ni	Mn
SQ1	mass %	96.31	1.99	1.13	0.57
	mol.%	96.21	2.14	1.08	0.58
P1	mass %	95.61	2.26	1.46	0.67
	mol.%	95.51	2.43	1.39	0.68

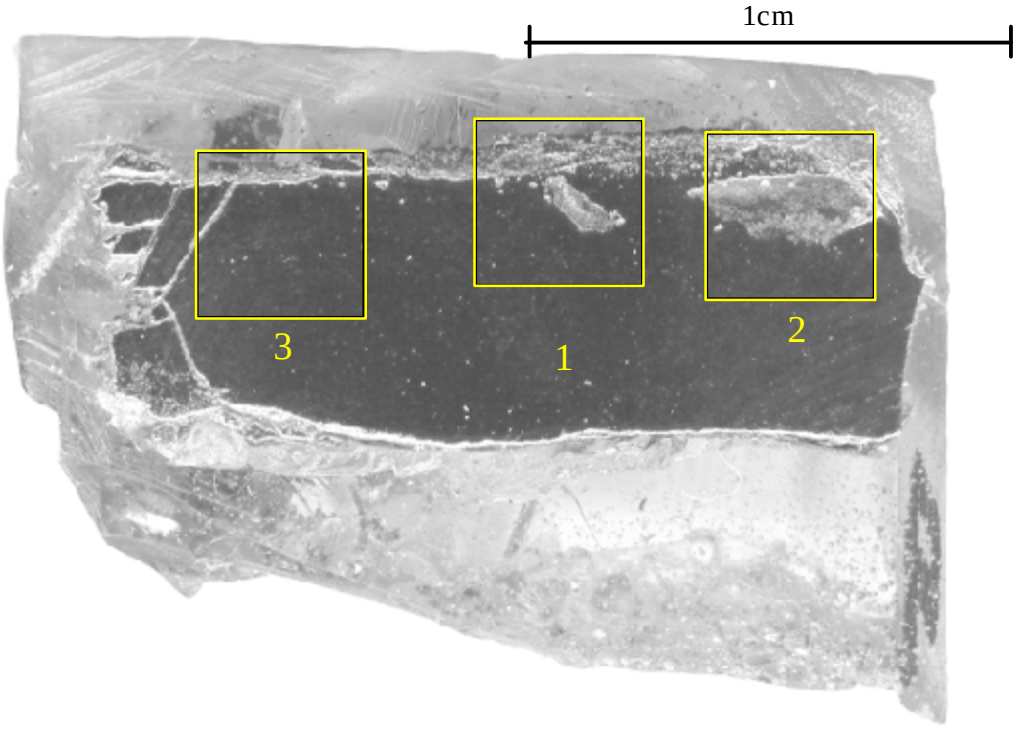

Fig. 2.5.32 – Template of the interaction zone upper part with regions marked for examination

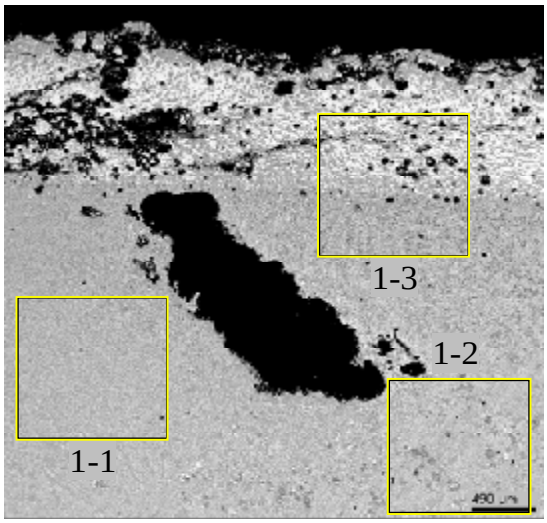

1

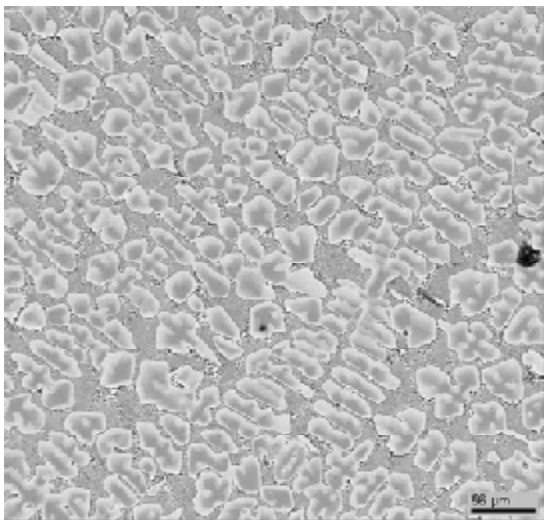

1-1 (SQ1)

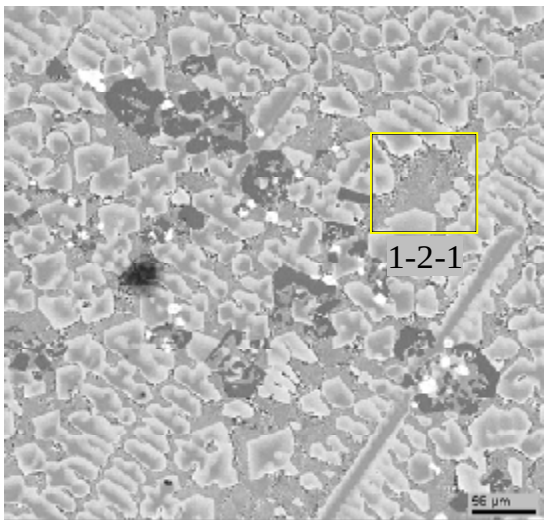

1-2

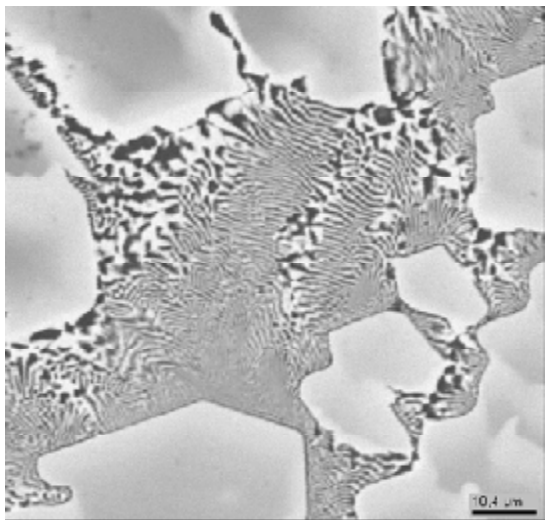

1-2-1

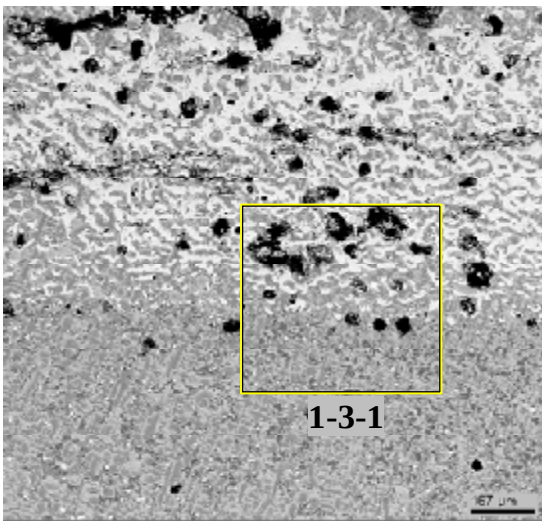

1-3

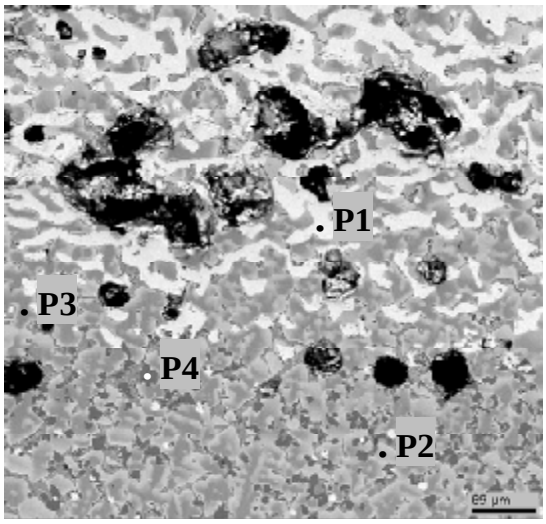

1-3-1

Fig. 2.5.33 – Micrographs of Region 1

Table 2.5.22 – Data on Region 1 EDX analysis

No.		U	Zr	Fe	Cr	Ni	~O
SQ1	mass %	40.39	6.40	50.37	1.43	0.95	0.45
	mol.%	13.98	5.78	74.30	2.27	1.33	2.34
	mol.%	14.31	5.92	76.08	2.33	1.36	
P1	mass %	86.94	1.02	-	-	-	12.04
	mol.%	32.35	0.99	-	-	-	66.67
	mol.%	97.02	2.98	-	-	-	
P2	mass %	44.66	8.37	44.78	0.86	1.34	-
	mol.%	16.74	8.18	71.57	1.47	2.03	-
P3	mass %	21.91	19.19	52.52	0.74	0.93	4.70
	mol.%	5.87	13.43	60.02	0.91	1.01	18.76
	mol.%	7.23	16.53	73.87	1.12	1.25	
P4	mass %	9.04	60.99	8.39	0.38	-	21.2
	mol.%	1.73	30.54	6.87	0.33	-	60.53
	mol.%	4.39	77.37	17.39	0.85	-	

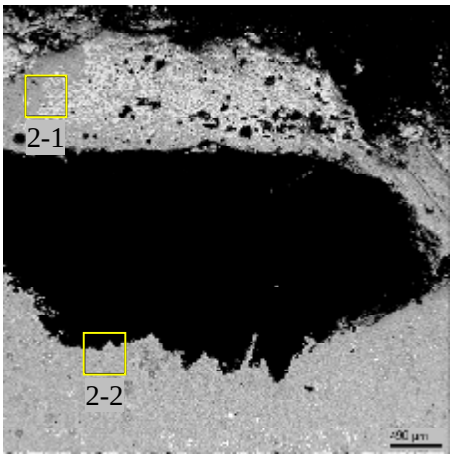

2

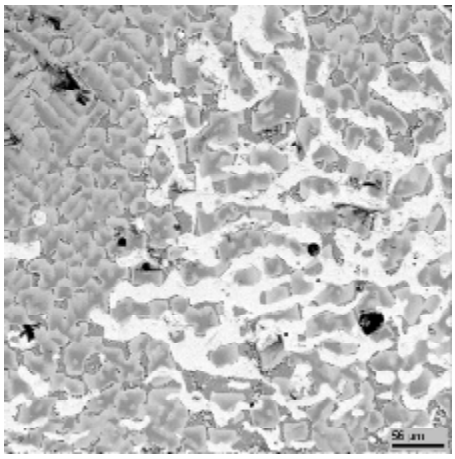

2-1

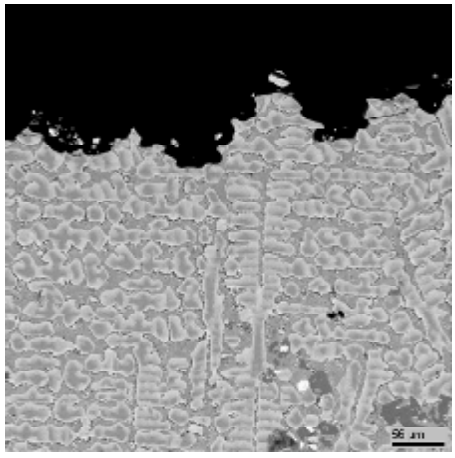

2-2

Fig. 2.5.34 – Micrographs of Region 2

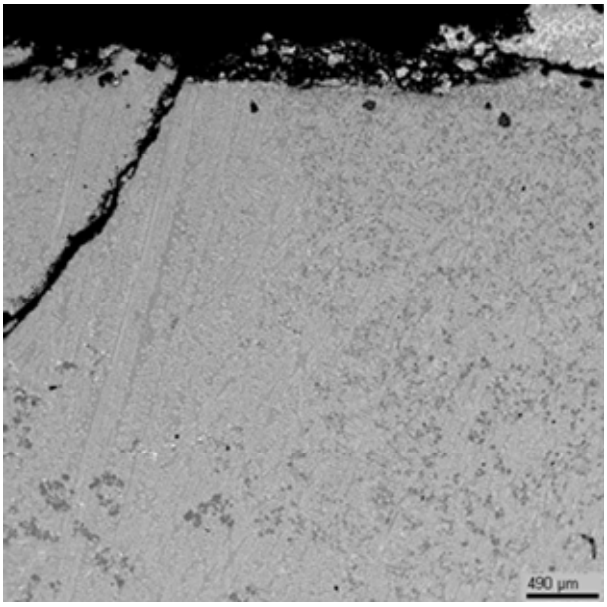

3

Fig. 2.5.35 – Micrograph of Region 3

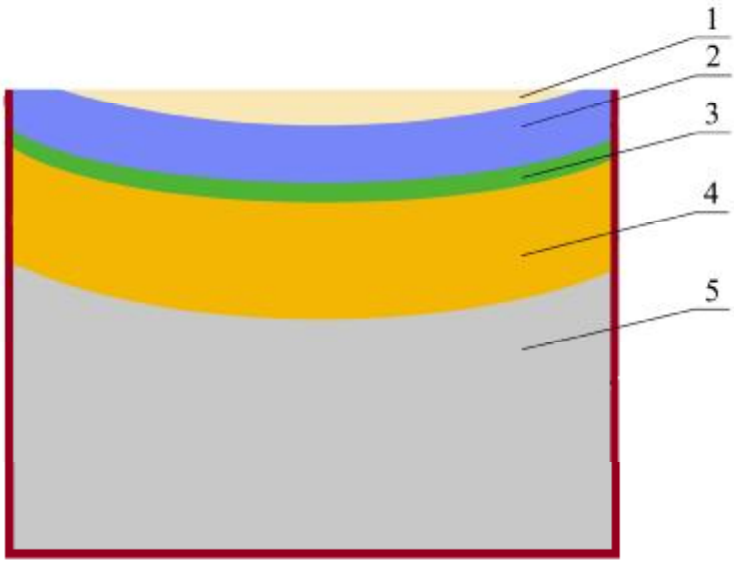

1 – shrinkage cavity; 2 – interaction zone upper layer;
3 – interaction zone intermediate layer; 4 – interaction zone lower layer;
5 – steel specimen

Fig. 2.5.36 – Diagram of layers position

2.6. Differential Thermal Analysis

The Differential Thermal Analysis (DTA) of samples taken from the upper and lower areas of the interaction zone (layers 2, 4 Fig. 2.5.36) of MC9 was made by the SETSYS Evolution-2400 analyzer [1]. The instrument allows investigation of thermal behaviour of substances within a wide temperature range from 196 up to 2400 °C. The instrumental error of temperature determination is ±5 °C.

The temperature of steel specimen - corium interaction initiation (solidus temperature, T_{sol}) was determined by the start of the endothermic effect at the sample heating and by the start of the exothermic effect at the sample cooling. The difference in T_{sol} values may be explained by a possible subcooling of the melt below T_{sol} during its crystallization, whereas there has not been detected any substantial superheating of a solid body above the solidus point. Therefore, the value registered at heating the sample is regarded as a more credible.

Tab.2.6.1 and Figs. 2.6.1, 2.6.2 offer SEM/EDX data on compositions and microstructures of the samples taken from layers 2 and 3 of the interaction zone.

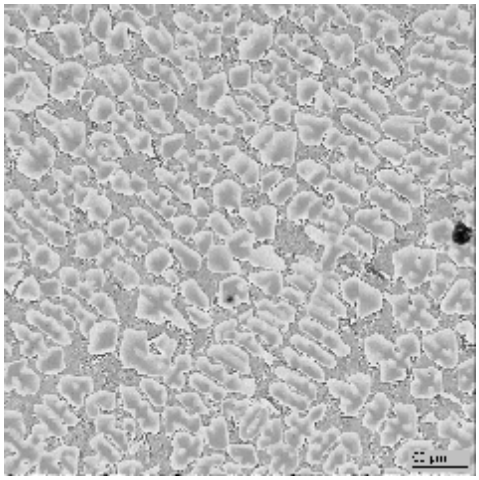

SQ1

Fig. 2.6.1 – Microstructure of layer 2 of the interaction zone

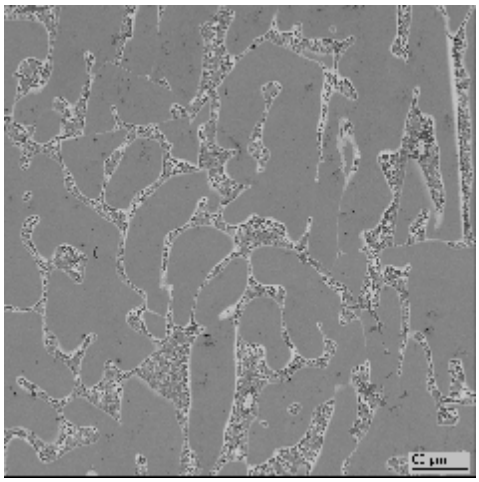

SQ2

Fig. 2.6.2 – Microstructure of layer 4 of the interaction zone

Table 2.6.1 – SEM/EDX data on the eutectic composition of samples taken from layers 2 and 4 of the interaction zone

No.		U	Zr	Fe	Cr	Ni	Mn	~O
SQ1	mass %	40.39	6.40	50.37	1.43	0.95		0.45
SQ2	mass %	26.87	13.36	55.27	0.97	1.19	-	2.34

Figs. 2.6.3 and 2.6.4 show DTA curves for a sample from layer 2 of the interaction zone.

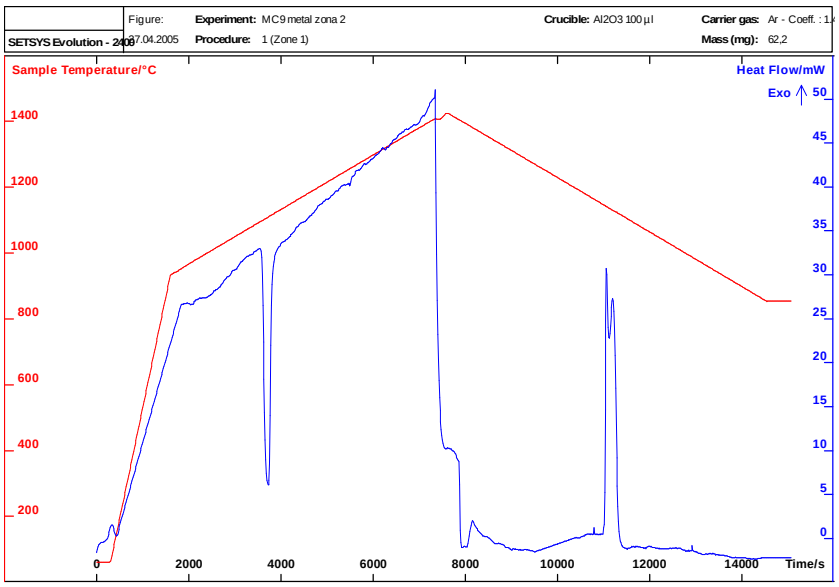

Analysis conditions:
Sample mass-62.2 mg;
Carrier gas - argon;
Carrier gas flow rate – 4 ml/min;
Heating rate – 5 °C/min;
Thermocouple type - B (PtRh 6%/30%);
Crucible material – Al_2O_3

Fig. 2.6.3. DTA curve, heating stage, sample from layer 2 of the interaction zone

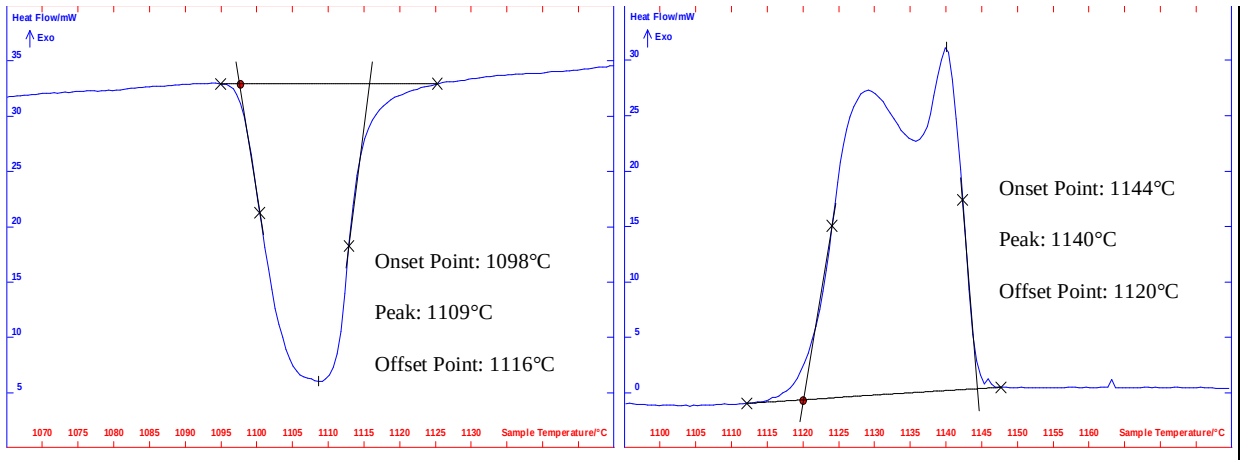

Fig. 2.6.4. Enlarged fragments of Fig. 2.6.3 , sample heating and cooling

Fig. 2.6.4 (heating) shows the 1088 – 1124°C temperature range to feature a clearly expressed endothermic peak. To determine the temperature corresponding to the peak onset, a baseline "linear from first to last point" was chosen and then the lines tangent to the peak slopes were

drawn. The point of tangent line crossing with the baseline yielded the temperature of 1098 °C corresponding to T_{sol}.
Figs. 2.6.5 and 2.6.6 show DTA curves for a sample from layer 4 of the interaction zone.

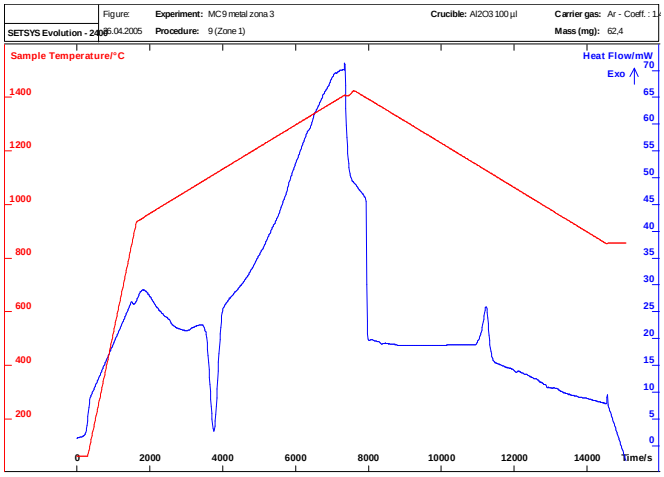

Analysis conditions:
Sample mass-62.4 mg;
Carrier gas- argon;
Carrier gas flow rate - 4 ml/min;
Heating rate-5 °C/min;
Thermocouple type - B (PtRh 6%/30%);
Crucible material –Al_2O_3

Fig. 2.6.5 – DTA curve, heating stage, sample from layer 4 of the interaction zone

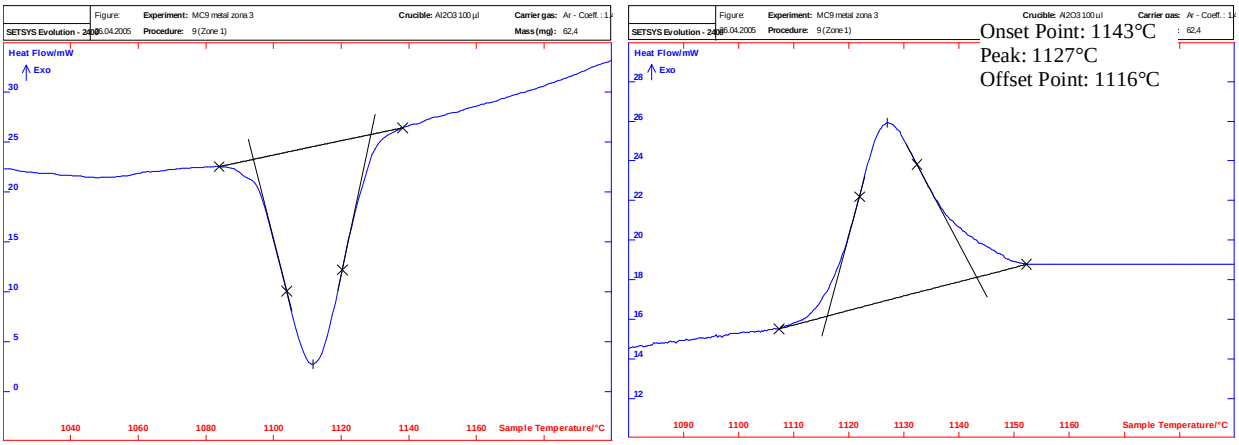

Fig. 2.6.6 – Enlarged fragments of Fig. 2.6.5, sample heating and cooling

According to the DTA data, T_{sol} values for both layers of the interaction zone are practically the same.

2.7. Composition of the oxidic ingot and interaction zone

Fig. 2.7 summarizes the results of the posttest XRF, SEM/EDX and chemical analyses. Notable is the satisfactory agreement of results obtained by all three methods for the ingot oxidic part. In the interaction zone, the XRF and SEM/EDX data agree satisfactorily for Fe and Cr. For U, agreement exists only between the XRF results for the templates upper surfaces. The Zr concentration data differ greatly. When discussing the collection of results for MC9, the SEM/EDX data were taken as the reference ones.

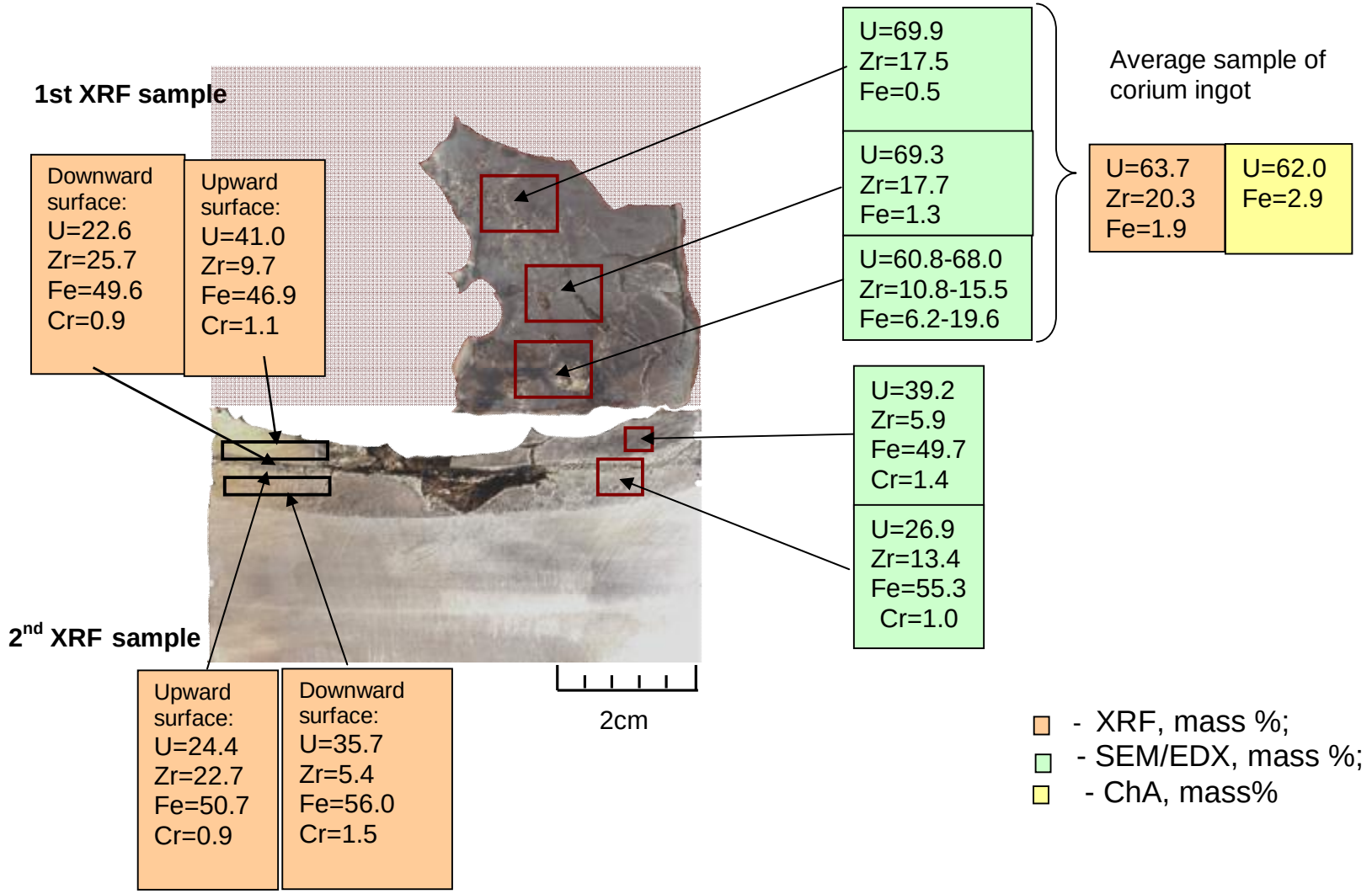

Fig. 2.7 – Results of posttest analyses obtained by different methods

3. Discussion of results

When discussing the results of MC9 concerning kinetics and depth of ablation of vessel steel at its interaction with a metal-oxide melt, it is reasonable to compare them with the results from MC6…MC8. At the same time, it is necessary to take into account the peculiarities of MC9, connected with intensive evaporation of steel components from the melt, and determine the reasons of some effects that were specific to this test. Finally, it is necessary to evaluate the obtained results for their relevance to the problem of in-vessel melt retention.

3.1. Molten pool structure

At the initial stage of MC9 stainless steel was introduced into molten suboxidized corium, and as a result of components repartitioning, a heavier metallic melt formed in the pool bottom part with a lighter oxidic melt above it. According to MASCA results, the characteristic time required for components repartitioning does not exceed 30 min. However, the molten pool structure undergoes changes during the test period – firstly, due to the processes of mass transfer between the molten pool and steel specimen, secondly due to steel components evaporation, and thirdly due to the ongoing mass transfer between the metallic and oxidic melts conditioned by the two previous processes. According to posttest, the molten pool was almost completely oxidic after the test (at its final stage). Let us assess duration of existence of the melt metallic part and use for this purpose the experimental data on the specimen ablation kinetics, on the release of aerosols, as well as experimental results from MASCA Project on components partitioning between the metallic and oxidic parts of the melt.

Fig. 3.1.1 offers the data on the release of steel components taking into account the losses in transport lines (see Section 2.2). The released amount totalled ~ 284.8 g at an almost constant evaporation rate. Section 2.2.6 contains also data on the composition of the interaction zone determined by posttest analyses. The mass of steel transferred from the interaction zone to corium was determined to equal almost 138 g. Taking into account the introduced (participating in the interaction) stainless steel (~ 192 g), the total mass of steel components which have got into the oxidic melt throughout the test equals ~ 330 g. This value is close to that of the total mass of the evaporated steel (mass of aerosols) plus the small amount of Fe (~ 35 g) discovered in the oxidic ingot. Thus, due to evaporation, the metallic part of the melt has exhausted by the time of test completion, or a little bit earlier, taking into account the mass balance error. That is, it may be expected that practically all the test through the specimen surface has been interacting with the metallic part of the melt, but this would be true only if the metallic part of the melt was in the pool bottom part permanently.

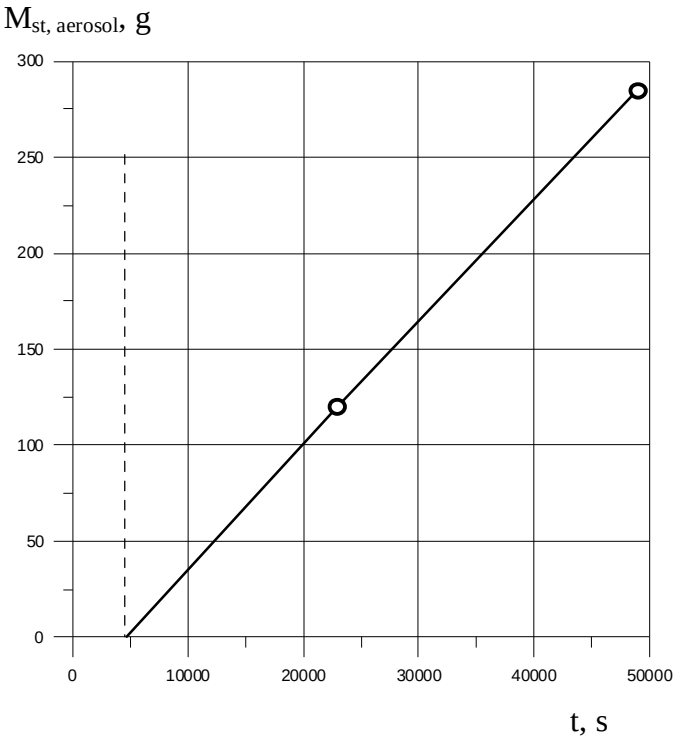

- - - - - – introduction of steel; ○ – measurements

Fig. 3.1.1 – Evaporation of steel during the test

To check how the mentioned condition is observed, let us consider kinetics of the mass transfer processes in the system “oxidic part of the melt – metallic part of the melt – steel specimen”. When doing so, let us conventionally break it into two systems: 1) oxidic and metallic parts of the melt; 2) metallic part of the melt – steel specimen. The interaction between the oxidic and metallic parts of the melt (initially – molten suboxidized oxides and steel) is governed by the regularities establised in the course of MASCA investigations. Fig. 3.1.2 offers generalized experimental data from MASCA [13] on the composition of the metallic part of the melt balanced with the oxidic part, depending on the relative mass of steel involved in the interaction, for U/Zr=1.2 and C-32, that is for the conditions of MC9. The initial relative mass of steel involved in the interaction: $\overline{m}_{st.} = M_{st.} / \left(M_{met.} + M_{ox.} \right) \approx 0{,}1 \left(10\% \right)$. In accordance with Fig. 3.1.2, the initial concentrations of U and Zr in the metallic part of the melt are 43 and 17 mass %, respectively.

Hypotheses and assumptions accepted for the follow-up calculations:

- The interaction zone composition is constant in time and coincides with the average composition determined by the posttest analyses: U – 33.3; Zr – 8.3; Fe – 53 mass %; the said composition is maintained by the corresponding diffusion of U and Zr from the metallic melt into the specimen and the counterdiffusion of Fe;
- The mass of steel involved in the interaction is a subject to changes, depending on its entry into the melt from the interaction zone as the specimen ablation progresses (see Section 2.4) and evaporation (according to Fig 3.1.1);
- Composition of the metallic part of the melt is determined from Fig. 3.1.2 according to the current value of the relative mass of molten steel participating in the interaction, neglecting the time required for attaining equilibrium state;

– The interaction zone is liquid; density of material in the interaction zone is determined additively on the basis of its composition; density of liquid is ~15% less than that of the solid ingot (determined from the volume of the shrinkage cavity).

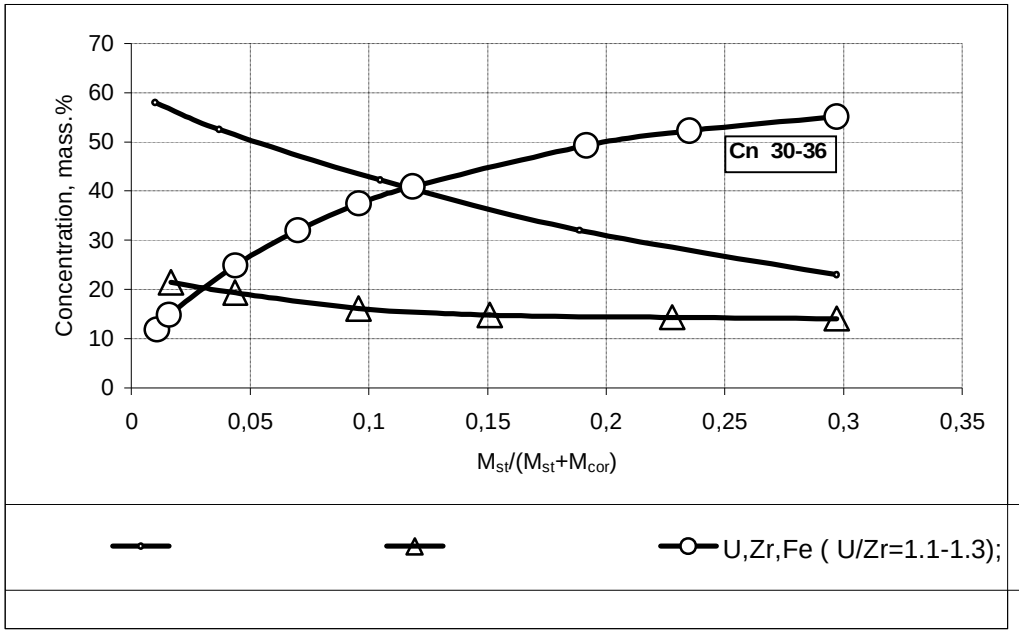

Fig. 3.1.2 – Distribution of components in the metallic part of the melt (according to MASCA results)

Figs. 3.1.3, 3.1.4 offer the results of calculations. It may be seen that during the test the mass of the metallic part of the melt is steadily decreasing down to a value close to zero, and the relative mass of molten steel involved in the interaction is decreasing correspondingly from 10% to practically zero. It follows from MASCA experimental results, in this range metallic melt has a highr density than the oxidic melt, i.e., indeed, the specimen was interacting with the metallic part of the melt within MC9. The concentrations of U and Zr in the metallic part of the melt (Fig. 3.1.4) all the test through exceed the concentrations of U and Zr in the interaction zone, it proving legitimacy of an assumption concerning permanent transfer of U and Zr from molten metal into the specimen (interaction zone).

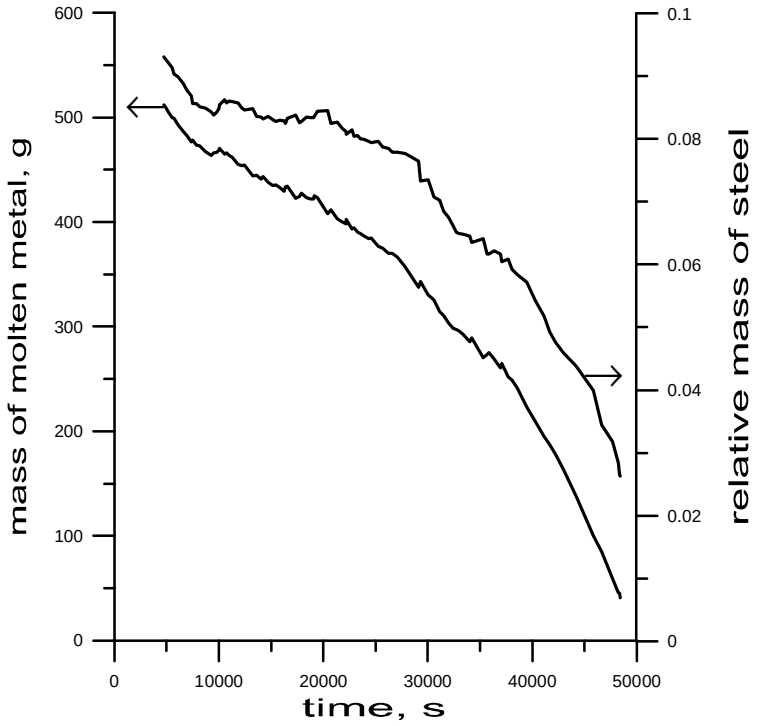

Fig. 3.1.3 – Mass of molten metal and relative mass of steel

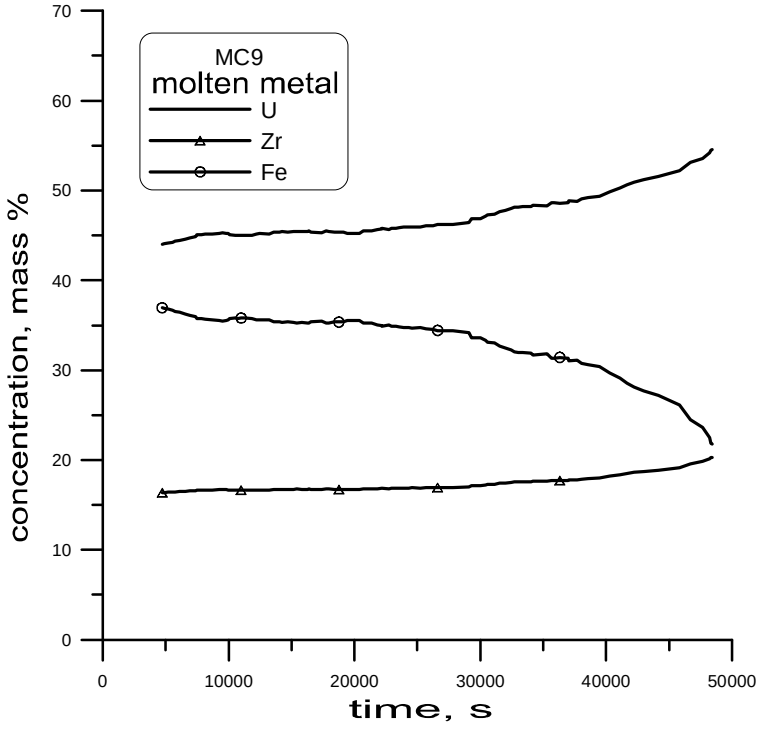

Fig. 3.1.4 – Metallic melt composition

3.2. Maximum depth of ablation

Calculations of the specimen temperature condition have found final position of the interaction front (boundary between the interaction zone and specimen) in MC9 to correspond to the

1060÷1100°C range. A comparison of this value with those obtained in MC6…MC8 [1] shows them to differ significantly (compare with the maximum value of 1200°C in MC8). Let us make an attempt to establish a correlation between this boundary temperature (T_{bndry}) and the interaction zone composition.

Tab. 3.2 contains the boundary temperatures and compositions of the interaction zone (for MC9, compositions of the lower and upper parts of the interaction zone, and the average are given). The table also contains the initial molten corium oxidation degrees (C_n) and maximum temperatures on the specimen top surface at the initial stage of interaction. Fig. 3.2.1 shows the influence of the mass concentration of Fe in the interaction zone (C_{Fe}) on the magnitude of T_{bndry}. Note, that the accepted concentration of Fe for MC9 is the one in the interaction zone lower part which had contacted with the specimen via the skull.

Table 3.2 –Interaction zone compositions and boundary temperatures

	Test No.					
	MC6	MC7	MC8	MC9		
				upper part	lower part	average
C_U, mass %	25.6	44	22	39.5	27	33,3
C_{Zr}, mass %	5.4	2.2	6.1	5.5	11	8,3
C_{Fe}, mass %	64.4	50	68.2	50	56	53
T_{bndry}, °C	1120-1200	1030-1100	1200	1060-1100		
C_n	C-32	C-32	C-70	C-32		
T_{surf}^{max} ,°C	1360	1150	1420	1440		

The numbers in Fig. 3.2.1 (and in Figs. 3.2.2, 3.2.3) denote MC tests. T_{bndry} obviously grows as C_{Fe} increases. From the model of eutectic interaction between suboxidized molten oxides and a steel specimen it follows that dissolution of steel stops when the interaction front reaches in the specimen an isothermal surface that has T_{sol} of the interaction zone composition. It may be assumed, therefore, that T_{sol} is increasing along with the growing C_{Fe}. A reason behind this increase may be the increased concentration of oxygen within the studied range of governing parameters variation. However, this supposition is contradicted by the DTA results for the material from the interaction zone, according to which T_{sol} is approximately similar in all tests and is close to 1090 °C (Fig. 3.2.1).

A possible explanation of the noticed contradiction is that during crystallization of the interaction zone the oxygen contained in it partially releases, i.e., either transits into molten corium, or forms gas pores (together with the shrinkage cavity). Obviously, T_{sol} goes down with the decreasing oxygen concentration. That is why the values obtained by DTA are underrated, the lowest possible ones, and closeness of T_{sol} values determined by DTA for different compositions of the interaction zone (for different tests) reflects only properties of the crystallized material and not always reflects properties of the material from the interaction zone in the course of a test.

A correlation between the interaction zone compositions and the governing parameters in tests of the MC series can be established proceeding from the below-given considerations. First of all, notable is that the mechanism of suboxidized molten oxides/cooled steel specimen interaction (the essence of which is in U, Zr, Fe and O repartitioning) is similar to the mechanism of suboxidized molten oxides/molten steel interaction which had been studied within the frame of the OECD MASCA Program [13], but not identical to that mechanism due to peculiarities of MC tests, that is, steel solidity, temperature gradient, and a crust of suboxidized corium on the surface of interaction. It may be expected that despite these differences, qualitative regularities of the process would not differ from those revealed by MASCA tests: at an equal ratio between the

mass of steel involved in the interaction and the total mass of oxides and steel, the greater is the oxygen potential of oxides, (i.e., the higher is the degree of Zr oxidation [C_n] in molten oxides),

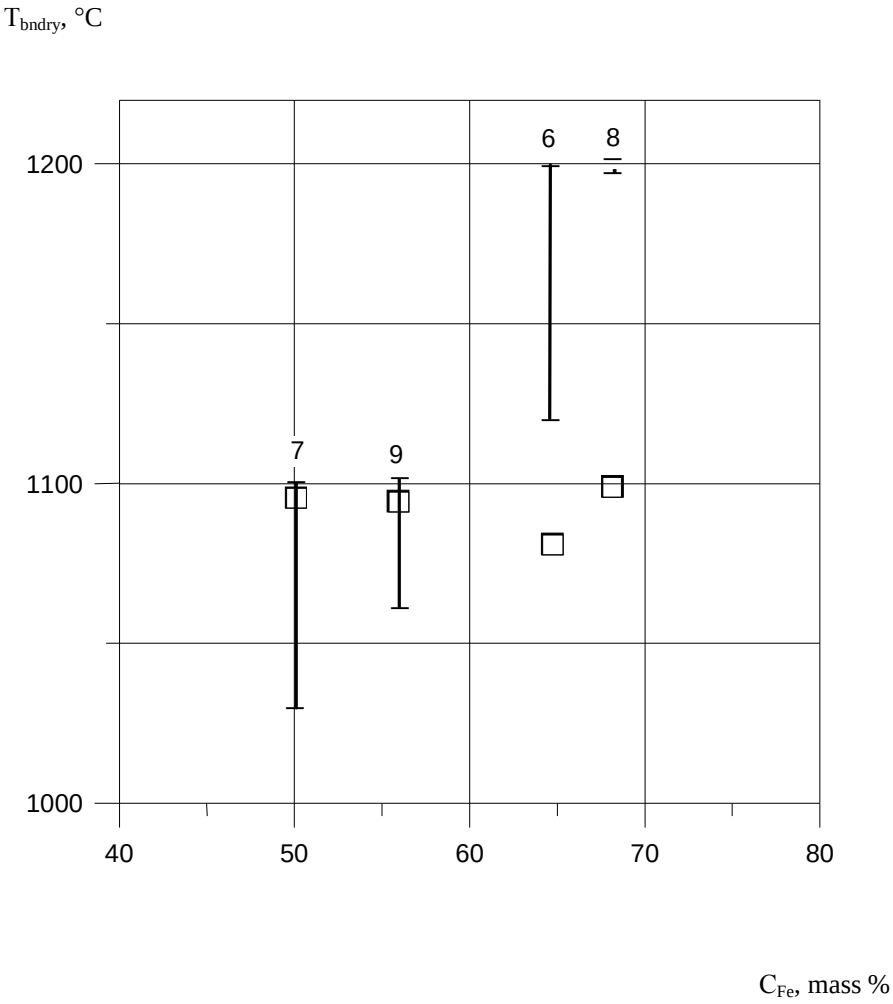

6÷9 – numbers of MC tests
I – test; B– DTA

Fig. 3.2.1 – Temperature at the interaction zone/specimen boundary as a function of concentration of Fe in the interaction zone

the higher is the concentration of Fe in the metallic part of the melt (in the interaction zone), while at the uniform oxygen potential of molten oxides, the larger is the mentioned relative mass of steel, the likewise higher is the concentration of Fe in the interaction zone (see Fig. 3.1.2).

A comparison of the results of MC6 and MC8 (the tests with similar relative masses of steel, 3.4 and 2.9 %, respectively) shows (Fig. 3.2.2) the concentration of Fe in the interaction zone of MC8 to be higher and correlate with a higher C_n value in this test (MC6 – C-30, MC8 – C-70). If we compare concentrations of Fe in MC6 and MC7 which had the same oxygen potential of the melt (~ C-30), it may be seen (Fig. 3.2.3) that when the relative mass of steel increases from ~0.4 % in MC7 up to 3.4 % in MC6, the concentration of Fe in the interaction zone grows from 50 up to 64.4 %, respectively. A similar analogy with the MASCA results exists for the regularities in concentration of U: depending on the said governing parameters, the concentration of U decreases (see Tab. 3.2). The concentration of Zr, however, behaves oppositely. While in

MASCA tests it changes (qualitatively) like the concentration of U, i.e., decreases, in MC6…MC8 it, on the contrary, grows (see Tab. 3.2).

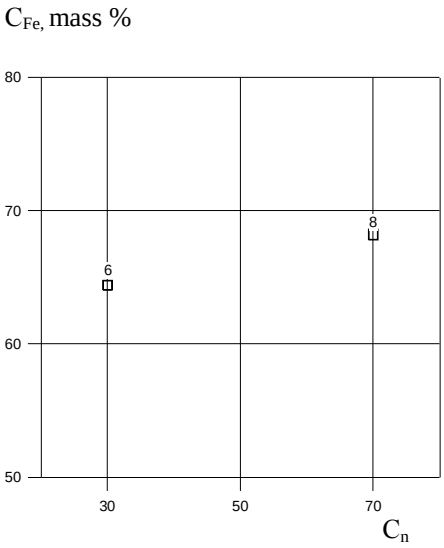

Fig. 3.2.2 – Concentration of Fe in the interaction zone as a function of the melt oxygen potential

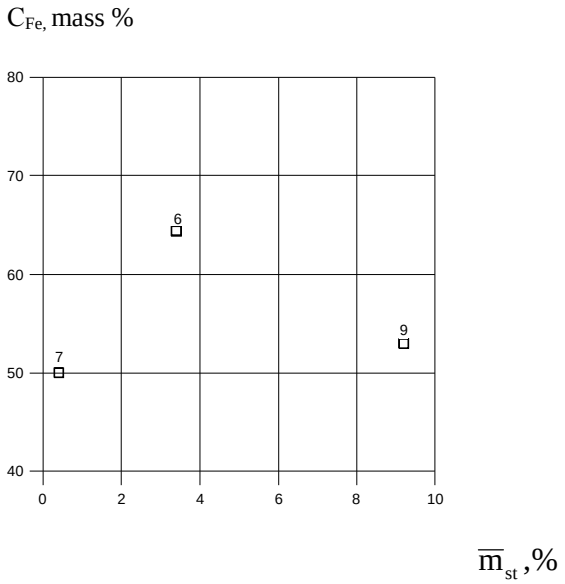

Fig. 3.2.3 – Concentration of Fe in the interaction zone as a function of the mass fraction of steel involved in the interaction with the melt

Along with the data from MC6 and MC7, Fig. 3.2.3 contains data on Fe concentration in the interaction zone of MC9 (in which oxygen potential of molten corium was the same, i.e., ~ C-30). Obviously, a decrease of concentration of Fe occurred in contrast to the expected growth against the increasing mass fraction of steel. To explain this result, peculiarities of MC9 should be analyzed.

The situation after the introduction of steel into molten oxides in the beginning of the test is in no way different from that in MASCA tests: the metallic melt that forms in the pool bottom part has a composition that under the same governing parameters of the test (U/Zr ratio, oxygen potential of molten oxides, relative mass of steel, molten oxides temperature) coincides with the composition determined in MASCA tests. Then, according to the MC9 conditions, the initial composition of the metallic part of the melt is as follows: U – 43; Zr – 17; Fe – 37 mass %. This composition changes in time under the influence of such factors, as mass exchange with the steel specimen, steel components evaporation, and components repartitioning between the said part and molten oxides (the latter process is the “quickest”). As the result of evaporation, the metallic part of the melt decreases in due course to the point of complete disappearance. However, in accordance with the regularities revealed in MASCA tests, the decreasing metallic part of the melt becomes increasingly enriched in U and Zr, and depleted of Fe, accordingly (see Fig. 3.1.4). A tendency to the components’ concentrations levelling in the metallic part of the melt and in the specimen’s interaction zone (in contacts with the former via the skull) explains a higher concentration of U and Zr and, correspondingly, a lower concentration of Fe in the interaction zone in MC9 in comparison with the values that could be expected if the procedures of MC9 and of MC6…MC8 were the same (i.e., if steel were not introduced into molten oxides in MC9). In such a case concentration of Fe in the interaction zone would have been closer to 70 % and the boundary temperature – to ~ 1200°C. A complete levelling of compositions of the metallic part

of the melt and of the interaction zone does not occur, presumably due to the regularities of chemical balance establishment in a system under thermogradient conditions.

Imagine a test similar to MC9, but featuring a surface crust that prevents Fe evaporation. If the mass of stainless steel introduced into the melt in this test is increased (though, below the amount at which molten metal forms a surface layer), then the increase in U and Zr concentrations in molten metal will inevitably cause their concentrations in the interaction zone to decrease and that of Fe increase, accordingly. It means that in such a case T_{bndry} will be higher than ~ 1090 °C in MC9. The same would happen due to the same reasons in a test similar to MC9, if the degree of molten corium oxidation (oxygen potential of molten corium) is increased. Concentrations of U and Zr in the metallic part of the melt will decrease if the mass of introduced steel is reduced, but the same effect was achieved in MC9 through the long-term evaporation of Fe. Therefore, it may be considered that concentrations of U and Zr in the interaction zone in MC9 are the maximum possible, while that of Fe is the minimum possible (at least, at $C_n \geq 30$) during the interaction of vessel steel with the metallic part of molten pool. Hence, the value of T_{bndry} from MC9 is the lowest possible for the described conditions. Though the calculated T_{bndry} falls within the 1060-1100 °C, its value cannot be lower than T_{sol} determined by DTA, therefore the minimum value of T_{bndry} should be accepted as equal to 1090°C.

3.3. Ablation kinetics

Fig. 3.3 shows histories of the ablation depth measured in the specimen central part in MC6…MC9. The major difference of MC9 from all other MC tests with suboxidized molten corium is in the absence of the incubation period which is the time required for the liquid phase to form on the specimen surface due to U and Zr diffusion from the oxidic crust surface into the steel specimen. Lack of this period in MC9 is an evidence of the liquid phase existence on the specimen surface from the very beginning of its interaction with molten metal. It means, that the molten metal that shifts to the pool bottom immediately starts impregnating the oxidic crust. The ultrasonic measurements show that during the period from steel introduction into molten oxides till the inversion (~ 5000 sec), the interaction of molten oxides with the specimen via the initial skull have not lead to the liquid phase formation. As is shown in Fig. 3.3, in MC6 and 7 featuring the same melt composition (~ C-30) the liquid phase had formed only by ~ 16000 sec.

In MC8 ablation of the specimen started after a much smaller lag than in MC6 and 7, approximately after 8000 sec. The difference in the incubation period duration may be due to the different content of Zr in molten corium (different oxidation degree). SEM/EDX has shown α-Zr to concentrate along the skull/specimen boundary and serve as an additional diffusion barrier for the transportation of U. It may be supposed that in MC8 (C-70 corium) the concentration of α- Zr is lower than in MC6 and 7 (~C-30 corium), and this conditions a shorter incubation period in MC8.

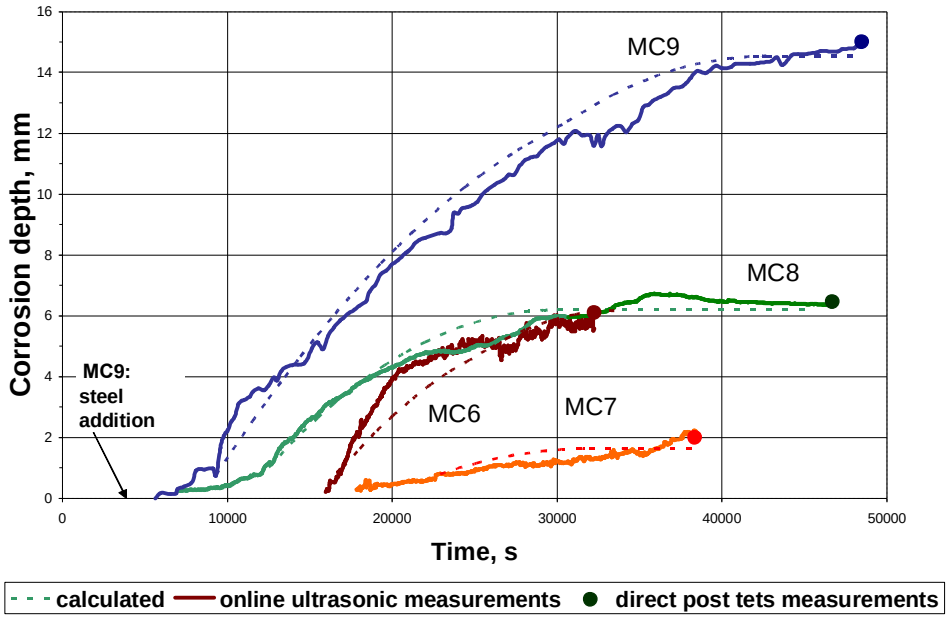

Fig. 3.3 – Vessel steel specimens ablation kinetics

The initial period of ablation (slow ablation period), which is most clearly observed in MC8, is associated with the time required for the forming liquid phase to "impregnate" the skull. Then, thanks to a reduced diffusion resistance, the mass transfer between molten oxides and the liquid phase on the specimen surface accelerates sharply and intensifies the dissolution of steel.

In terms of quality, the main period of ablation (fast ablation period) in MC 9 does not differ from such periods in MC6 and 8, and is characterized by 1) a decreasing rate of ablation with the lapse of time due to the temperature lowering at the interaction front as it progresses inside the specimen, and 2) ablation stoppage when a temperature equal to T_{sol} of the material of the interaction zone is attained. However, ablation rates in the performed tests have significant quantitative differences.

The most considerable difference in rates is observed at the initial stages of the fast ablation period when rates are maximal (at maximum temperatures at the interaction front, i.e., in subsurface layers of the specimen). Apparently, the lowest value of ablation rate in MC7 is determined by the minimal temperature of the specimen surface (~ 1150°C), it being much lower than in other tests.

Based on general considerations, it may be believed that at equal temperatures of the specimen surface the rate of ablation would be the higher, the larger is the share of liquid phase in the interaction zone in proximity to the ablation surface. If we assume that during the fast ablation period the establishment of chemical equilibrium in an oxide-metallic system by means of components repartitioning through the skull happens much faster than the dissolution of steel, the share of the said liquid phase may be judged from the difference between the specimen surface temperature and T_{sol} of the interaction zone composition in the U-Zr-Fe(Cr,Ni…)-O system.

Thus, it may be supposed that throughout the fast ablation period its rate is the higher, the larger is the difference between the current temperature at the ablation front and the value of T_{bndry} determined by composition of the interaction zone.

Using the calculated values of temperature distribution in specimens and experimental data on the ablation depth history in all the performed tests, an approximated empirical correlation for the vessel steel ablation rate during the fast ablation period has been deduced:

$$\frac{dh}{dt} = 0.46 \cdot 10^{-4} \sqrt{T_{int} - T_{bndry}}\ , \text{ mm/s.}$$

The calculated and experimental data are compared in Fig.3.3. In accordance with Fig. 3.2.1, the following T_{bndry} values have been accepted: MC7 and MC9 – 1090°C; MC6 – 1180°C; MC8 – 1200°C. Notable is the satisfactory agreement between the calculated and experimental data.

Let us comment another result of the tests which, strictly speaking, refers to the maximum depth of ablation, but is most vividly illustrated by Fig.3.3. The question is about the big difference in depth in MC6 and MC9. The reason of such a big (over two times) difference is not only in different T_{bndry} values, small differences in surface temperatures and input heat flux densities, but also in the differences in heat drainage down the specimen lateral surface to the cold crucible. The latter is conditioned by differences in thermal conductivity of the lateral insulation which depends on the degree of ZrO_2 granules and powder compactness (packing) and changes unpredictably from test to test. Apparently, the said thermal conductivity in MC9 happened to be minimal and, in particular, determined the maximum distance from the specimen surface to the ~ 1090°C isotherm.

3.4. Specimen temperature condition

In contrast to MC6…MC8, the analysis of the specimen temperature condition in MC9 has revealed some peculiarities of both temperature measurements and numerical modeling conditions.

First of all, it should be noted that two thermocouples – TC01 and TC03 – went faulty, and readings of a peripheral surface thermocouple TC8 almost all test through were ~ 70°C lower than those of TC10, a peripheral surface thermocouple located 4 mm from the top, and therefore regarded as unvalid. Naturally, the said three thermocouples were omitted from the analysis and their readings are missing in Fig. 1.2.2 (Section 1).

Among the remaining thermocouples, attention is attracted to the “strange” readings of TC02, TC04 and TC09 (see Fig. 1.2.2): starting from ~ 30000 sec, the readings are reducing steadily against the almost stable temperature recorded by the nearby thermocouples (along the radius and concerning the distance from the specimen upper top). A possible reason of this decrease is discussed below. The only thing that can be mentioned now is the correlation between the azimuthal position of the mentioned thermocouples (located in the “narrow” azimuthal region, see Tab. 1.1) and shape of the shrinkage cavity: hot junctions are located right in the places where the shrinkage cavity – pretty asymmetrical – is deeper (see Fig. 3.4.1). Due to the described reason, the enumerated thermocouples were omitted from the numerical modeling of the specimen temperature condition at the final stage of the test.

It was noted in Section 2.3 that the numerical modeling of the specimen temperature condition at the final stage of the test has found the best agreement between the calculated and measured temperatures when radially uniform heat supply to the specimen (to the interaction zone upper boundary) was specified, while according to calculations of molten oxides’ thermal hydrodynamics the mentioned heat supply appeared to be significantly nonuniform, with its maximum in the central part of the specimen top. The attempts to change the result by varying thermal conductivity of the interaction zone material yielded no positive effect, as it required an assumption that this material is anisotrophic, i.e. that its radial thermal conductivity is considerably higher than the axial, but there would be no reasonable explanation for that.

A possible reason of the noted discrepancy in the distribution of the heat flux to the specimen may be as follows: it may be supposed that the specimen steel surface layer undergoes

decarbonization as a result of the prolonged exposure at a high temperature, and the carbon becomes partially oxidized by oxygen contained in the interaction zone. The then generating gaseous phase may accumulate under the skull and form a cavity or a small layer located mostly in the central surface part of the interaction zone. In such a case, a significant thermal resistance would arise in the central part of the heat supply zone; it cannot be modeled in the calculations of the specimen temperature condition, but its resulting effect may be equal to the evenning of the radial distribution of the input heat flux. If accumulation of the gaseous phase occurs above that part of the zone where the shrinkage cavity would form later, it may explain the above-mentioned “strange” readings of the thermocouples TC02, TC04 and TC09: the local heat supply would decrease with the growing thickness of the gaseous layer and would lead to the local progressive temperature drop (in the azimuthal region where the said thermocuples are located). Then the time around 30000 sec from the beginning of the test may be regarded as the instant when formation of the gaseous layer started.

Another peculiarity of the specimen temperature condition requiring a discussion is its change during the long-term, almost steady-state regime in MC9. A comparison of readings of TC05, TC06 (10 mm radius, 6 and 8 mm from the upper top, respectively) and of TC10 (29 mm radius, 4 mm from the upper top) at the steady-state regime initial and final stages shows that readings of the centrally located thermocouples gained 50 °C, on the average, while those of the peripheral one lost 40 °C. To explain this effect, the calculations described in Section 2.3 were supplemented by electromagnetic and thermal-hydrodynamic calculations for a molten pool under conditions of the steady-state regime initial stage, i.e., for the initial structure of the metal-oxidic pool. In comparison with calculations for a single-phase melt, the calculation procedure was modified as follows: for describing the melt motion in MC9, a model has been apllied that describes a 2-D non-stationary axis-symmetrical motion of a two-phase non-isothermal viscous liquid in the field of gravity and electromagnetic forces with a dispersed volume source of heat. Unlike in [12], the equations of thermal hydrodynamics were solved together with the electromagnetic field equations.

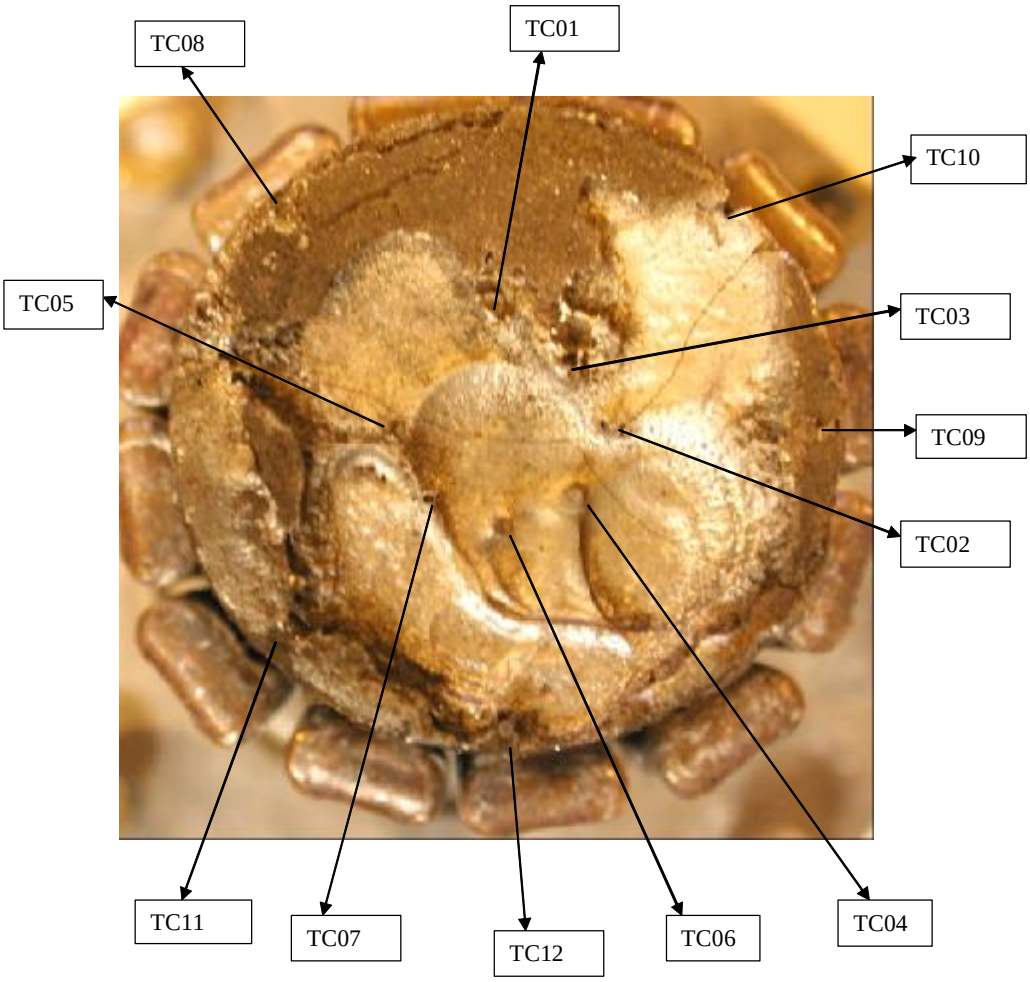

Fig. 3.4.1 – Specimen surface after interaction, top view

Lorentz force ($\bar{f}$) and volume source of heat (W) were calculated from the relations

$$\bar{f} = \bar{J} \times \bar{B} = y\left(\bar{E} + \bar{V} \times \bar{B}\right) \times \bar{B}, \quad (1)$$

$$W = \bar{J} \cdot \bar{E}, \quad (2)$$

where $\bar{J}$ – flow density vector;

$\bar{E}$ – electric field intensity vector;

$\bar{B}$ – magnetic flux density vector;

$\bar{V}$ – velocity vector;

σ – specific conductance.

Electric ($\bar{E}$) and magnetic ($\bar{B}$) field intensities are connected with the vector potential $\left(\bar{A}\right)$ by equations

$$\bar{E} = -\frac{1}{c}\frac{\partial \bar{A}}{\partial t} - \text{grad}\varphi, \quad (3)$$

$$\bar{H} = \text{rot}\bar{A}. \quad (4)$$

c - is the velocity of light.

In the case of a sine field, the vector potential amplitude equation is written as

$$\frac{1}{\mu}\left(\frac{\partial^2 \dot{A}}{\partial r^2}+\frac{1}{r}\frac{\partial^2 \dot{A}}{\partial r}+\frac{\partial^2 \dot{A}}{\partial z^2}-\frac{\dot{A}}{r^2}\right)=i\gamma\omega\dot{A}, \qquad (5)$$

and electric field intensity and the volume source of heat may be calculated using the formulas

$$W=\frac{1}{2}\gamma\omega^2\left|\dot{A}\right|^2, \qquad (6)$$

$$\dot{E}=i\omega\dot{A}, \qquad (7)$$

where $\dot{A}$ is the vector potential amplitude;

μ is the magnetic permeability;

ω is the circular frequency;

i - imaginary unit.

The presence of the second liquid (metal, in our case) in the calculation cell is characterized by its volume fraction F. The condition F = 1 is met when the calculation cell is completely filled with metal, and F = 0 in the absence of metal in the calculation cell; partial filling corresponds to $0 < F < 1$.

The transport equation for F is written as

$$\frac{\partial F}{\partial t}+\mathrm{div}\left(\overline{V}F\right)=0. \qquad (8)$$

Here, the velocity vector $\overline{V}$ is determined through solving the obtained system of equations, in which thermalphysic and electrical specific parameters are determined by the relation

$$\varphi=\varphi_1 F+\varphi_2\left(1-F\right), \qquad (9)$$

where φ is the effective specific parameter, and

φ_1, φ_2 are specific parameters of the 1st and 2nd liquids.

Intensive parameters are determined by the relation

$$\psi=\frac{\omega_1 c_1 F+\omega_2 c_2\left(1-F\right)}{c_1+c_2}, \qquad (10)$$

where ψ is the effective intensive parameter,

ψ_1, ψ_2 are intensive parameters of the 1st and 2nd liquids, and

ρ_1, ρ_2 are densities of the 1st and 2nd liquids.

Surface tension was taken into account when determining the oxide/metal interface (see [14] for details of the algorithm). Like in [12], discrete analogs of differential equations of the model have been constructed by the method of final volumes [15].

Structure of a metal-oxidic pool is shown in Fig. 3.4.2. Figs. 3.4.3 – 3.4.5 show distribution of temperature, of heat generation, as well as the distribution along the specimen surface radius of the heat flux from the melt to the specimen (the absolute values of heat flux are overestimated due to overestimation of the total power extracted into the melt). It is obvious, that in contrast to

the analogous distribution at the final stage of the test, at the initial stage the maximum input heat is shifted to the specimen top surface peripheral part. This transformation in the heat flux distribution explains the recorded temperature history.

In accordance with the obtained data on the input heat distribution, the specimen temperature condition has been calculated (see Figs. 3.4.6, 3.4.7). Fig. 3.4.6 shows satisfactory agreement between the calculated and measured temperatures (at the initial stage of the test the thermocouples TC02, TC04 and TC09 functioned “normally” and their readings were used in these calculations). The maximum temperature at the axis of the specimen top surface amounted to 1440°C, it being noticeably lower than the analogous temperature value obtained through calculations performed for the steady-state regime final stage (see Fig. 2.3.4, Section 2.3).

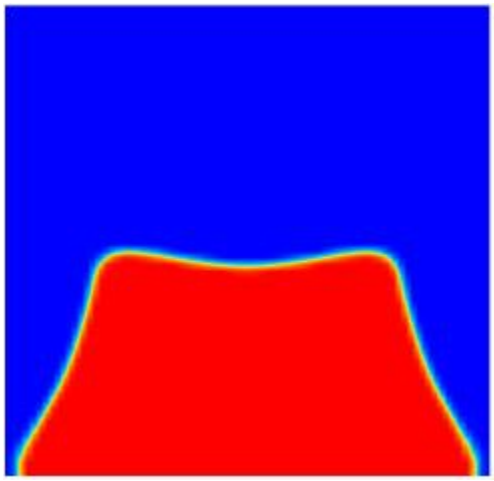

Fig. 3.4.2 – Oxide/metal phases (dark/light)

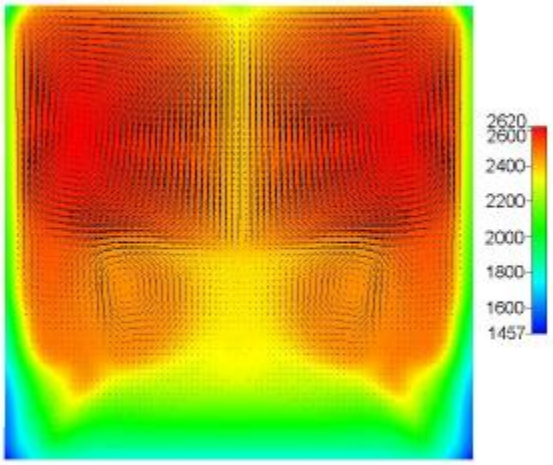

Fig. 3.4.3 – Temperature distribution (°C)

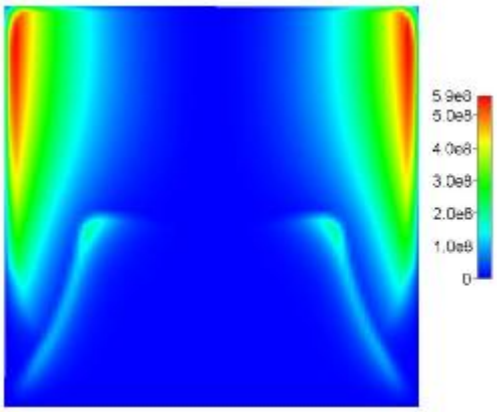

Fig. 3.4.4 – Distribution of heat generation (W/m^3)

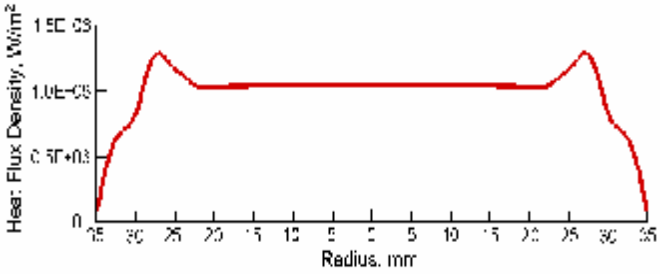

Fig. 3.4.5 – Heat flux distribution

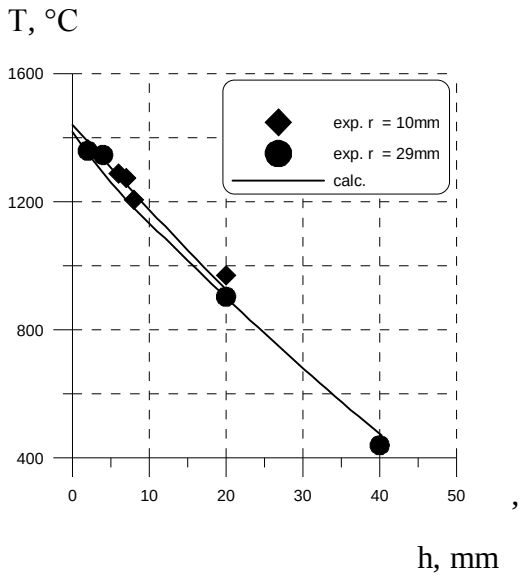

Fig. 3.4.6 – Temperature distribution along the specimen height

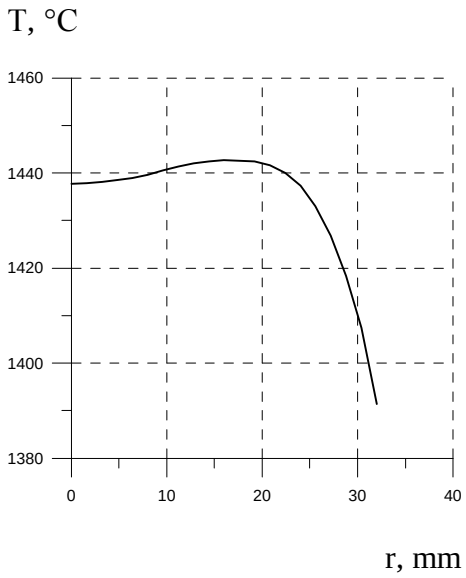

Fig. 3.4.7 – Temperature distribution along the specimen top radius

3.5. Main results of the test

Let's consider relevance of the results of MC9 for the in-vessel melt retention. Like in MC6…MC8, the maximum depth of ablation corresponds to the position in the steel specimen body of an isothermal surface with a T_{bndry} close to T_{sol} of the U-Zr-Fe(Cr,Ni…)-O system, which is determined by the interaction zone composition, which, in its turn, depends on corium characteristics and the initial temperature condition of the specimen. Like in MC7, under the conditions of MC9 the value of T_{bndry} is regarded as the minimum possible one (~ 1090 °C). Kinetics of steel ablation in MC9 differs from that in MC6…MC8 by the absence of the incubation period, i.e., the time required for reaching the maximum depth of ablation at the interaction between vessel steel and metallic part of the suboxidized molten corium is smaller than during the interaction with the oxidic part, all other factors being equal. In principle, evaporation of steel components during MC9 could influence the conditions of melt/specimen interaction. However, in the absence of evaporation (in presence of an oxidic crust at the molten pool surface) just a slight increase of T_{bndry} is possible. That is, in terms of the maximum depth of ablation, the conditions of MC9 were the most conservative. The absence of steel components evaporation could influence ablation kinetics indirectly via the changing T_{bndry}. It was discussed in Section 3.3 that the increase of T_{bndry} will lead to the slowing ablation. Therefore, from the point of view of kinetics the conditions of MC9 were also conservative. Consequently, there is no reason in any other additional tests modeling the conditions that exclude evaporation of vessel steel components.

A more general conclusion can be made that additional investigations of the vessel steel ablation depth and kinetics envisaging modification of the metal-oxidic melt characteristics would be irrational, at least with the horizontally positioned interaction surface and $C_n \geq 30$, as any combinations of experimental conditions would be unable to reduce the obtained minimum value of T_{bndry} (≈ 1090 °C) and increase the ablation rate. The latter may happen only if the specimen surface temperature increases within the range between the experimentally obtained ~ 1400°C and the temperature of steel melting of ~ 1500°C.

From the point of view of the in-vessel melt retention, the processes studied in MC6…MC9 may influence mechanical behaviour of the vessel, which depends on thickness of its intact part. According to the results of investigations, the wall thickness limit (from the inside) may be regarded as justified for a surface with a temperature equal to 1090 °C, if the molten corium is suboxidized ($C_n \geq 30$). It does not matter then, which part of the melt – oxidic or metallic – the vessel steel is interacting with.

Computation of the reactor vessel ablation is reduced to the preliminary calculation of its temperature condition (vessel thickness temperature distribution) and subsequent integration in accordance with the ablation rate dependence $W \equiv \frac{dh}{dt}$, given in Section 3.3.

$$h = \int_0^t W(T_{int})\,dt = 0{,}46 \cdot 10^{-4} \int_0^t \sqrt{T_{int}(h) - 1090}\,dt,$$

where T_{int} is the temperature at the interaction front, °C,

h is the ablation depth, mm, and

t is time, sec.

The deduced dependence is empirical and is inapplicable to vessel steel and corium compositions differing from the studied ones.

An incubation period is absent for the metallic part of the melt; it may be disregarded for the oxidic part in the most conservative formulation, and a more precise evaluation may be based on the data obtained for molten C-30 and C-70 applying linear interpolation to duration of this period in the investigated range. In all cases, the depth of ablation during the incubation period and the intermediate period of ablation may be neglected. Duration of ablation requires the transformation of temperature condition of the reactor vessel against the decreasing residual heat to be taken into account in accident calculations.

Conclusions

1 The MC9 test devoted to studies of the interaction between the metallic part of suboxidized molten prototypic corium and the water-cooled steel specimen has shown that:

- The mechanism of vessel steel ablation is that of eutectic melting (dissolution). The maximum depth of ablation is close to the distance from the specimen surface to the isothermal surface with ~ 1090°C, and does not exceed this distance. From this point of view, the interaction between vessel steel and metallic part of suboxidized molten corium does not differ from the interaction with the oxidic part of the melt.
- Due to the lack of the incubation period, vessel steel ablation at the interaction with the metallic part of the melt is anyway shorter than that at the interaction with the oxidic part. For both metallic and oxidic melts, ablation kinetics (during the fast ablation period) is characterized by a decreasing rate of ablation against the decreasing temperature of the vessel steel at the interaction front.

2 When substantiating the concept of suboxidized molten corium in-vessel retention, thickness of the wall in calculations of the vessel mechanical behaviour should be limited by a value determined by position of the 1090°C isotherm.

3 An empirical correlation is proposed for calculating ablation kinetics of the reactor vessel steel at its interaction with suboxidized molten corium.

References

1. Khabensky V.B. et al. Investigation of corium melt interaction with NPP reactor vessel steel // Annual Report (METCOR, Phase 2, 2nd year). ISTC Project No. 833.2-2003.
2. Losev N.F. Quantitative X-ray fluorescence analysis. Moscow, Nauka Publishers, 1969.
3. Riabchikov D.I., Seniavin M.M. Analytical chemistry of uranium. Moscow, Publishing House of the USSR Academy of Sciences. 1962.
4. Lukianov V.F., Savvin S.B., Nikolskaya I.V. Photometric detection of uranium microquantities using reagent arsenazo III. JACh., v. XV, issue 3. 1960.
5. Markov V. K. et al. Uranium. Methods of its determination. Moscow, Atomizdat Publishers, 1964.
6. GOST 4011-72. Drinking water. Methods for determination of total iron.
7. Sendel E. Methods of metal traces determination by colorimetry. Moscow, Mir Publishers, 1964.
8. Yeremina B.G. Gas analysis. Moscow, Mir Publishers. 1955.
9. Baksanova L.E., Budnikov V.I., Valtsifer V.A. Gas volumetric method of active aluminium determination in polymeric materials. Factory laboratory. No.7, v. 66. 2000.
10. Butirin G.M. High-porosity carbon materials. Moscow, Khimiya Publishers, 1976.
11. Bekkert M, Klemm H. Reference book on metallographical etching. (Russ. transl.), 2nd edition, revised and updated. Moscow, Metallurgiya Publishers, 1988, 400 p., illustr.
12. Khabensky V.B., Bechta S.V., Smirnov S.A. Molten corium hydrodynamics and heat transfer during IMCC. R&D Report, ISTC Project 833.2-2003, 2004.
13. Asmolov V.G., Bechta S.V., Khabensky V.B. et al. Partitioning of U, Zr and FP between Molten Oxidic and Metallic Corium. Proceedings of MASCA Seminar 2004. Aix-en-Provence, France, June 10-11 2004.
14. C.W. Hirt and B.D. Nichols. Volume of Fluid (VOF) Method for the Dynamics of Free Boundaries. J. Comp. Phys., 39, 201, 1982.
15. Patankar S. Numerical Heat Transfer and Fluid Flow. Moscow. Energoatomizdat. 1984. 152 p.